INVESTIGATION OF THE

PROCESSING-STRUCTURE-PROPERTY RELATIONSHIP

IN Ta-Si-N NANOCOMPOSITE COATINGS

by

ANNA ZAMAN

DISSERTATION

Presented to the Faculty of the Graduate School of
The University of Texas at Arlington in Partial Fulfillment
of the Requirements
for the Degree of

DOCTOR OF PHILOSOPHY

Arlington, Texas
May 2018

Acknowledgements

I would like to take this opportunity to express my gratitude for all the invaluable help, input and support I received during my graduate study to make this research possible.

First and foremost, I would like to thank Dr. Efstathios I. Meletis for being my research advisor. This research has been guided by his enriched knowledge and expertise in the subject. His encouragement and instructions provided me the right amount of structure with some level of independence to design my thesis forward.

I would like to thank our collaborators in Spain for their help in the characterization of the Ta-Si-N films. I would like to thank my committee members Dr. Yaowu Hao, Dr. Kyungsuk Yum, Dr. Harry F. Tibbals, Dr. Deajong Kim. I sincerely thank Dr. Jiechao Jiang for his help with various characterization equipment at UTA.

Each and every one of my lab mates receives thanks for their advice, assistance and training during my time as a graduate student. I would specially like to thank Yi Chen for his immense help with the nanoindentation, Dr. Jessica Mooney for training me on the magnetron sputtering system and Dr. Mingui Zhang for her help with the TEM. I'd like to acknowledge the UTA labs SaNEL and CCMB, because of which the research was possible.

Finally, I would like to thank my family for their constant support throughout the course of my graduate studies.

May 2018

Abstract

INVESTIGATION OF THE

PROCESSING-STRUCTURE-PROPERTY RELATIONSHIP

IN Ta-Si-N NANOCOMPOSITE COATINGS

Anna Zaman, PhD

The University of Texas at Arlington, 2018

Supervising Professor: Efstathios I. Meletis

The present-day industry demands development of coatings for harsh environmental applications which can resist impact and oxidation at high temperatures. It is vitally important to develop new hard (>30 GPa) protective coatings which will be thermally stable at temperatures, T > 800 °C and simultaneously will ensure a good protection of the substrate against oxidation from an external atmosphere. The limitations of conventional coatings due to inferior hardness or poor oxidation stability can be overcome by nanocomposite coatings as they exhibit enhanced and completely new properties. To address this requirement of new enhanced protective systems, there is a need to get a better understanding about the effects of the elemental composition, phase composition and microstructure on the mechanical and thermal properties of the coatings.

In this body of work, two transition metal nitride (TmN) systems, (Ta-N and Ta-Si-N) were explored in detail to develop an overall understanding of the relationship between the processing conditions, the microstructure, and the mechanical properties of the as-deposited thin film nanocomposite coatings. Reactive magnetron sputtering was used to deposit tantalum nitride (Ta-N) thin films on Si substrate. The effect of varying the N_2 percentage in the N_2/Ar gas mixture, varying substrate bias and varying temperature on the Ta-N film characteristics was investigated.

The highest hardness of ~ 33 GPa was shown by the Ta-N films containing the hexagonal Ta_2N phase (films deposited with 5% and 3% N_2 in the gas mixture). Decreasing the N_2 content in gas mixture below 7% was found to result in microstructural refinement with grain size ~5-15 nm. The film deposited with 3% N_2 in the gas mixture exhibited nano-needle like morphology and besides displaying highest hardness, it exhibited a high hardness/modulus ratio (1.33), elastic recovery (68%) and very low wear rate (3.1×10^{-6} mm^3/Nm). This film (deposited with 3% N_2 content in the gas mixture) remained thermally stable upto 780 ^oC.

The knowledge gained from the study of the Ta-N system was used as a base to explore ternary Ta-Si-N coating. Relationships between the crystal structure, microstructure and mechanical properties of this coating system were discovered and explored in detail. The film crystal structure displayed the same transition as that observed in the Ta-N system, changing from face centered cubic (fcc) TaN (at 20% N_2 in the gas mixture) to a mixture of fcc $TaN_{1.13}$ and hexagonal Ta_2N (at 15% N_2) to non-textured hexagonal Ta_2N (at 13% and 10% N_2) and finally to textured hexagonal Ta_2N (at 7% N_2). XPS revealed Ta-N and Si_3N_4 binding states in the films. The microstructure changed from a columnar morphology (20 - 30 nm wide columns) with visible amorphous boundaries (5-10 nm thick) at 13% N_2 content in the gas mixture, to columnar without presence of any amorphous boundaries (at 15% N_2). The films deposited with 13% - 15% N_2 content in the gas mixture, displayed high hardness of ~40±2 GPa and remained thermally stable upto 800 ^oC. Besides high hardness, the 13% N_2 film had high H/E* ratio of 0.11, elastic recovery of ~60 % and relatively low friction coefficient of 0.6 and low wear rate ($7.09x10^{-6}$ mm^3/Nm). The high hardness of the films was attributed to the dense nanocolumnar structure, with nanocrystals of ~5-10 nm in size with different crystallographic orientations within these columns.

Table of Contents

List of Figures

List of Tables

Chapter 1 Introduction

One of the central challenges in modern engineering science is to protect a material at its surface from chemical reactions and mechanical degradation. Applying a hard coating, which bonds strongly to the surface of the material, prevents excessive abrasion and provides the needed shield towards mechanical impact. Coatings nowadays are used in a tremendous number of items. Many tools (e.g. drilling bits), medical devices (e.g. hip joints), consumer products (e.g. solar cells), all kind of glasses (e.g. windows and spectacles) and displays (smartphones and tablets) are covered with a protective, functional and/or decorative coating to enhance their efficiency, life time and appearance [1- 3]. A global market study estimates, that just the nano-coatings market in the year 2011 was US$ 1.5 billion. Optimistic estimations for nanoscale and thin film market were up to US $13 billion until the year 2016 [4,5]

1.1 Research Motivation

The development of hard/superhard coatings is driven both by the scientific curiosity of researchers to explore possibilities of synthesizing a material whose hardness could approach or exceed that of diamond ($H \geq 70$-100 GPa) and the technical importance of these coatings. At high temperatures in an oxidative environment many hard coatings quickly deteriorate due to thermal instability and chemical degradation. The thermal stability of majority of hard coatings produced so far is relatively low, up to the temperature $T \leq 1000$ °C only. Temperatures $T \leq 900$-1000 °C are insufficient for the utilization of such coatings in many applications [6,7]. Typical examples of these applications are the coatings for cutting tools for high-speed cutting, turbine blades for ground electric power stations, engines of aircrafts and special parts of super high-speed aircrafts, rockets and reusable launch vehicles (space-shuttles, pilot free space transporting vehicles, etc.) exposed to extreme temperatures (up to about 2000 °C). On the other hand, coatings which are

stable at high temperatures (> 1000 ^{o}C) are mostly amorphous and lack the much-needed high hardness (> 30 GPa). Therefore, it is vitally important to develop new hard (≥30 GPa) protective coatings which will be thermally stable at temperatures, T ≥ 900 °C and simultaneously will ensure a good protection of the substrate against oxidation from an external atmosphere.

The limitations of conventional coatings due to inferior hardness or poor oxidation stability can be overcome by nanocomposite coatings. Nanocomposite coatings represent a new generation of materials and are composed of nanocrystalline (nc-) grains, fibers or crystallites with less than 10 nm diameter surrounded by an amorphous (a-) matrix [8-21]. The nanocomposite materials, due to their multiphase nature and very small grain size (≤ 10 nm) can exhibit enhanced or completely new properties, e.g., increased mechanical strength, high resistance to oxidation at temperatures above 1000 °C, low friction and low wear, enhanced toughness and enhanced resistance to cracking, compared to the conventional coatings [23]. These facts are a main driving force stimulating the development of nanocomposite materials to address the need of hard and oxidation resistant coatings.

It was found that there are at least four types of nanostructures as shown in Figure 1-1, that result in the enhanced hardness of nanocomposite coatings: (1) bilayers with nano size period λ, (2) the columnar nanostructure, (3) nanograins surrounded by very thin (~1 to 2 ML) tissue phase and (4) the mixture of nanograins with different crystallographic orientations and/or different phases, here λ= h1+h2, h1 and h2 are the thickness of first and second layer of the bilayer, respectively, and ML denotes the monolayer [23]. Individual nanostructures are formed under different conditions using either a sequential deposition of individual layers in the nanosize bilayers or in transition regions where the coating structure changes from crystalline through nanocrystalline to amorphous.

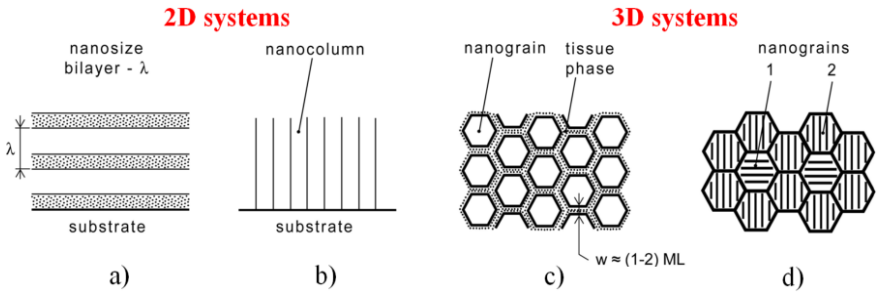

Figure 1-1 Schematic illustration of four nanostructures of the nanocomposite coating with enhanced hardness [23].

Amongst these proposed nanostructures, the structure where the nanograins are dispersed in an amorphous matrix are referred to as DNG/AM coatings, (Figure 1-1: c). The most remarkable feature of the DNG/AM nanocomposite coatings is the fact that a very low (≤ 10 at. %) amount of the element added in the amorphous material results in enhanced property of the base material. The prototype for this nanostructure was theoretically modelled and experimentally verified by Veprek and was based on isolated nanocrystals of TiN surrounded by a monolayer of a-Si_3N_4 as shown in Figure 1-2. This type of a nanocomposite (nc-TiN/a- Si_3N_4) has been shown to increase the hardness of single phase TiN from 23 GPa to about 70 GPa [18, 25]. Another similar form of nanostructure which results in enhanced hardness is shown in Figure 1-1 (e) where the nanograins grow in columnar morphology in addition to being dispersed in thin amorphous matrix. Properties of these nanocomposites are determined not only by the size of nanograins and the separation distance between them but also by (i) the structure, phase and elemental composition of nanograins and (ii) the mutual interaction between the nanograins [24] and these structures can be extended to other transition metals like Hf, Ta, Cr, Zr, etc with the possibility that it might result in a structure with increased hardness (> 30 GPa).

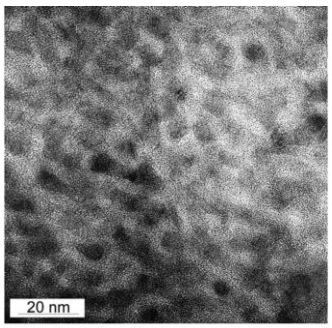

Figure 1-2 TEM showing the proposed structure of nc-TiN/a-Si_3N_4 with an amorphous monolayer between nanoscale TiN grain [18].

However, the thermal stability of hard coatings produced so far is relatively low upto temperature ≤ 1000°C. The present state-of-the art in the field of the oxidation resistance of hard protective non-oxide coatings based on nitrides is summarized in Figure1-3 which clearly shows that the crystalline coatings exhibit a lower oxidation resistance (not exceeding ~ 1000 °C) [24].

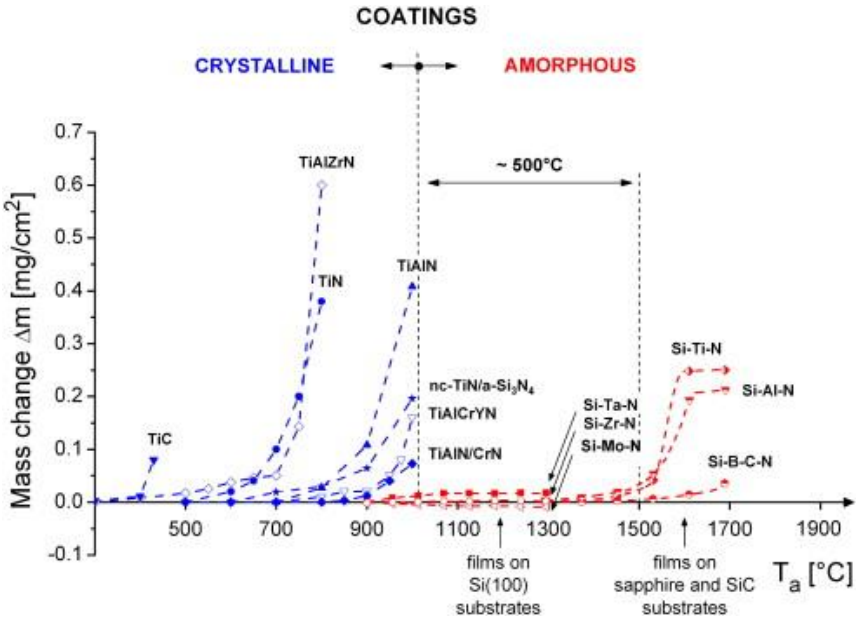

Figure 1-3 Oxidation resistance of selected hard crystalline and amorphous coatings [24].

On the contrary, the oxidation resistance of amorphous coatings is much higher and easily exceeds 1000 ^{o}C. As the amorphous content of coatings increases, there is a decline in their hardness for e.g. to achieve superhardness in case of nc-TiN/a-Si_3N_4 nanocomposite coating, the

fraction of the a-Si_3N_4 phase should be typically close to only about 17-23 mol. %. Limiting amorphous content to about 20% does improve oxidation resistance of TiSiN (oxidizes at 600 ^oC) as compared to single phase TiN (oxidizes at 400 ^oC) but is still less than satisfactory. Thus, to increase both hardness and oxidation resistance of a nanocomposite coating, the efficient way is the control of the amount of crystalline and amorphous phases in addition to careful selection of elements.

1.2 Proposed Research and Objectives

The impressive number of outstanding physical, chemical and mechanical properties of transition metal nitrides (Me-N) makes them very attractive materials for wide variety of industrial applications. Various Me-N and Me-Si-N systems have been explored to some detail by researchers, such as TiN, TiSiN, ZrN, CrN, TaN etc [26, 27]. TiN is the most explored hard coating; however, it exhibits inferior oxidation resistance at temperatures above 500 ^oC. CrN coatings have excellent wear quality and oxidation resistance above 600 ^oC; however, they exhibit highly rough surfaces because of the formation of a crystalline Cr_2O_3 surface oxide layer after annealing. To further expand the applications of Me-N systems (applications requiring temperatures above 900 ^oC), quasi-amorphous Me-Si-N systems have been considered. Amongst the group of nc-MeN/a- Si_3N_4 coatings, here Me = Ta, Zr, Ti, Al, Mo, W, etc. Ti-Si-N has been the most frequently studied. TiSiN coatings show great promise as a high hardness coating but again their performance in terms of high temperature oxidation resistance is still less than satisfactory (oxidizes at 600 ^oC).

Another potential candidate among the transition Me-N's is Ta-N which is chemically inert, corrosion resistant and has the ability to resist oxidation up to 800 ^oC. The theoretical hardness of Ta-N exceeds that of TiN. Investigations carried on Ta-N clearly indicate their

potential as a high hardness coating [28-31]. Recent evidence shows that when sufficient amount of Si is incorporated in Ta-N, the Ta-Si-N coatings display excellent oxidation resistance. Ta-Si-N nanocomposite coating with high amorphous content has been tested at higher temperatures displaying resistance to oxidation upto 1350 ^{o}C. However, these coatings lack the enhanced hardness present in Ta-N and TiSiN coatings [32-35]. As mentioned above, nanocomposite coatings based on Veprek's structure (specifically nc-TiN/a-Si_3N_4), displayed enhanced hardness and improvement in resistance to oxidation compared to single phase TiN. Strengthening caused by decrease in grain size finally reaches a saturation due to absence of dislocations in ultra-small nano-crystals. The strength and hardness of such a material may further be enhanced when another strengthening mechanism becomes dominant. This mechanism of strengthening is due to hindering of grain boundary sliding when there is about one monolayer of Si_3N_4 acting as a glue tissue between the TiN nanocrystals. Application of proposed DNG/AM nanostructure model of hardness enhancement to the Ta-Si-N system, while controlling the amount of crystalline (nc-TaN) and amorphous phases (a-Si_3N_4), has the potential and possibility to create revolutionary coatings with both high hardness (>30 GPa) and excellent high temperature properties (> 900 ^{o}C). In addition to TaN and Si_3N_4, SiO_2 and Ta_2O_5 will be formed during deposition due to the presence of residual oxygen. Oxidation resistance of this nanocomposite model can be further increased by reducing the anion vacancies in SiO_2. Silicon dioxide being a more stable oxide (ΔG_f° = -856.3 kJ/mol) as compared to Tantalum pentaoxide (Ta_2O_5; ΔG_f° = -780.3 kJ/mol) will be formed first during the process. Diffusion of Ta in Silicon Dioxide (surrounding the TaN grains) will reduce the oxygen anion vacancies and thus, it is expected to reduce oxygen diffusion and hence increase oxidation resistance. Previous reports regarding TaN/TaSiN coatings were focused on the

fabrication methods and properties, however, very limited detailed microstructural analysis relevant to the coatings has been reported.

As is well known that a material's physical properties are determined by the microstructure, therefore, getting a clear understanding of the microstructure evolution and how the microstructure affects coatings properties is imperative. With a good understanding of the effects of the fabrication parameters on coatings microstructure and the microstructure effects on the coatings properties, coatings with tailored properties can be designed by controlling the preferred nanometer scale components.

The overall objective of the present research is to fulfill the needs of coatings for harsh environment applications which can resist impact and oxidation at high temperatures.

The specific objectives of this research are:

1. To develop an understanding of the relationship between the processing parameters (like N_2/Ar ratio, substrate bias, deposition temperature), the microstructure and the mechanical properties of the Ta-N system, design a high hardness Ta-N coating.

2. Use the Ta-N as a model system and add Si with the expectation to produce a nanocomposite microstructure of Ta-N grains surrounded by a Si-N tissue phase with the overall goal of synthesizing and understanding the microstructure-property relationship in this ternary system. While controlling the Si and overall amorphous content within the Ta-Si-N film, it is possible that the DNG/AM proposed nanostructure for hardness enhancement may be extended to the Ta-Si-N system, and at the same time achieve thermal stability and oxidation resistance at high temperatures of existing systems such as TiSiN.

Based on the above knowledge, develop an overall understanding of mechanical response and oxidation resistance in these coatings, which will help design new protective and advanced

coating systems. The coatings will be fabricated by magnetron sputtering which can produce coatings with high levels of purity and refined microstructure [36].

1.3 Structure of the thesis

This dissertation consists of six chapters. The following is an outline and brief summary of each chapter included in this document.

Chapter 1, Introduction: This chapter introduces the main motivations, including both commercial and scientific motivation, and objectives behind the work. It also provides a brief introduction to the current knowledge in the state of MeN/MeSiN coatings.

Chapter 2, Literature Review: This chapter gives detailed background information on the state of the art of hard coatings and the mechanism of hardness in conventional and nanocomposite coatings.

This chapter introduces the concept for the design of nanocomposite coatings and why Ta-Si-N is a potential candidate for high hardness/high oxidation resistant coating in the field of Transition Metal Silicon Nitride (MeSiN) coatings.

Chapter 3, Thin Film Fabrication and Characterization: This chapter describes the deposition system set up and deposition parameters for TaN and TaSiN thin films. In addition, details are provided regarding the characterization methods and processes used including X-Ray diffraction (XRD), nano-indentation, high resolution transmission electron microscopy (HRTEM), X-Ray photoelectron spectroscopy (XPS), Auger electron spectroscopy (AES), tribometry, and surface optical profilometry.

Chapter 4, Microstructure and Property Investigation of Tantalum Nitride Coatings: A detailed study of the properties and microstructure of Ta-N films with varying deposition conditions were explored using HRTEM, nano-indentation, and XRD.

Chapter 5, Microstructure and Property Investigation of Tantalum Silicon Nitride Coatings: A detailed study of the properties and microstructure of Ta-Si-N films with varying deposition conditions were explored.

Chapter 7, Conclusions: The major results and conclusions of this investigation.

Chapter 2 Literature Review

In modern materials science, nano-scale materials are experiencing rapid development due to their existing and/or potential applications in a wide variety of technological areas such as electronics, catalysis, ceramics, magnetic data storage, structural components, etc. The search for coating materials having excellent mechanical properties (e.g., high hardness > 30 GPa) for use at high temperatures (> 900°C) has made use of technology in both composite and nanoscale materials science and remains a fascinating area for future study and advancement of the knowledge of high hardness coatings.

2.1 Hardness: Mechanism

Hardness is an important mechanical property of materials. It is defined as the resistance of solid matter to plastic deformation. Hardness is high when:

(i) the average bond strength is high

(ii) the number of bonds per unit volume is high

(iii) the average number of valence electrons per atom is high

(iv) bonds are strongly directional (i.e., have a large covalent component) ionicity and metallicity decrease hardness [37].

Diamond, with strong and fully covalent bonds, satisfies all of the (i)-(iv). Cubic BN, with partially ionic bonds, has a somewhat lower hardness. Graphite, though containing stronger bonds than diamond, has a much lower number of atoms and bonds per unit volume, and must therefore be softer. To relate the atomic structure to hardness, both the strength of the chemical bonds and the rigidity of the bonding network must be considered because it is possible to have flexible crystals with very strong bonds [38]. In crystalline materials, any plastic deformation caused by a force requires dislocation movement. Dislocations are crystallographic defects or irregularities

within a perfect crystal structure [39]. A dislocation propagates until a barrier or the solid surface is reached. Their movement is impeded by different kinds of stress fields and by other dislocations, inducing a pile-up of dislocations in front of barriers [40-42].

Although leading experts in the field believe that diamond will remain the most intrinsically hard material, much effort has been devoted to the processing and understanding of new, high-hardness materials, especially for use as tribological coatings. Much of the recent research in the field of high hardness coatings focuses on the development of thin film materials which can maintain their mechanical properties at high temperatures.

2.2 State of the Art

Hardness can be measured in a variety of ways, defining three types of hardness: scratch hardness, indentation hardness and rebound hardness. In this thesis, hardness is referred to as indentation hardness. The deposited films are thin (~700 nm), and hence it is important that the films and not the substrates hardness is measured. In general, a nanoindenter is used and certain measurement rules have to be considered to obtain the indentation hardness H: $H = P_{max}/A$

where P_{max} is the maximum load and A is the contact area [43].

Processes that result in hardening are grouped in bulk hardening and in thin film hardening. The bulk hardening effects are often used in the metal working industry and imply solid solution strengthening, precipitation hardening, work hardening, martensitic transformation, Hall-Petch strengthening, inverse Hall-Petch softening, and bombardment hardening. The thin film hardening effects are generated by sputter techniques and encompass hardening effects caused by coherency strains, misfit dislocations, thermal stress, orientation, Koehler stresses, interlayer stabilization, supermodulus effect and polarization strengthening [21, 44- 45].

Coatings can be classified according to a) their hardness: H > 20 GPa are called hard, H ≥ 40 GPa are considered superhard and coatings with H ≥ 80 GPa are ultrahard or b) can be divided in single and multiphase coatings. Holleck classified hard coatings according to their bond nature: metallic (transition metal-nitrides, -carbides and -borides), covalent (nitrides, carbides and borides of Al, Si and B, including diamond) and ionic (e.g., oxides of Al, Be, Ti and Zr [41, 46-47]. As mentioned, an important criterion for the choice of hard materials is their high intrinsic hardness. From this point of view, boron and silicon nitrides (c-BN and g-Si_3N_4) having short covalent bonds and high binding energies are regarded as the most promising candidates [48-49]. The nitrides of several early transition metals, namely of groups 4 to 6 of the periodic table, e.g., TiN, ZrN, VN, TaN and CrN, show similar properties with respect to hardness, high-temperature stability and chemical inertness. Titanium Carbide coatings became the earliest tribological coatings to gain widespread industrial use. Later, Titanium Nitride (TiN) coatings were developed via methods such as PVD and were quickly developed to become commercially available. While both TiC and TiN coatings remain relevant today as tribological coatings, significant efforts have been made to adjust the chemical composition, processing methods, and overall performance properties of these materials in order to fit a wide variety of materials application needs. Titanium Carbon Nitride (TiCN) coatings were developed to combine the good thermal and hardness properties of TiN coatings with the superior adhesion properties of TiC coatings. Typically, TiCN coatings display about 80% higher hardness as compared to TiN, as well as a reduced coefficient of friction [2, 50-51]. Other advancements to the field of hard coatings for use in extreme environments have included but are not limited to TiBCN, SiBCN, TiAlN/CrN [52-55]. A list of currently known hard materials is given in Table 2-1.

Table 2-1 Vickers Hardness values, Bulk Moduli and Shear Moduli for some common hard materials [38].

Material	**Vickers Hardness (GPa)**	**Bulk Moduli (GPa)**	**Shear Moduli (GPa)**
Diamond C	96±5	443	535
BC_2N	—	408	445
Cubic BN	63±5	400±3	409±6
Defect zincblende C_3N_4	—	448	390
Cubic C_3N_4	—	496	332
B_6O	35±5	228	204
TiB_2	33±2	244	263
SiO_2 (stishovite)	33±2	305±11	220
B_4C	30±2	247	171±11
TiC	29±3	241±1	188±6
SiC	28±3	226±9	196±13
ZrC	27±2	223	166±2
$AI2O_3$	22±2	246±11	162±2
Si_3N_4	21±3	249±3	123±2
$MgSiO_3$ (perovskite)	18+2	256±7	177
TiC	18±2	217	118
HfN	17±2	422	141
VN	15±1	268	159
NbN	14±1	315±28	156
AIN	12±1	203±5	128+2
GaN	12±2	210	120
TiN	24	-	-

Alternative approaches to the search for the hardest phase and/or for the novel superhard chemical compounds are based on modification of the materials microstructure in order to increase additionally the hardness of the materials over their intrinsic hardness (based on bond strength) in the single crystalline state. Two of them are nanostructuring, i.e., reducing the crystallite sizes to the nanometer range, and the design and formation of nanocomposites, i.e., material combinations

with pronounced interface phenomena. These approaches have been applied successfully for nitride nanocomposites [23].

2.3 Concept for the Design for Hardness Enhancement in MeSiN Nanocomposite Coatings

The main feature of nanocomposites is enhanced hardness. Mechanisms which are responsible for the hardness enhancement are: i) the dislocation induced plastic deformation, ii) the nanostructure of materials, and iii) Cohesive forces between atoms. The dislocation-induced plastic deformation dominates in the materials composed of large grains with size d >10 nm. On the contrary, the nanostructure is dominant in materials composed of small grains with size d≤10 nm. It means that the hardness enhancement of coating strongly depends on the grain size d, Figure 2-1. From this figure, it is seen that there is a critical value of the grain size $d_c \approx 10$ nm at which a maximum value of hardness of the coating is achieved. The regions around maximum hardness, correspond to a continuous transition from the activity of the intragranular processes at $d > d_c$, dominated by the dislocations and described by the Hall–Petch law to the activity of the intergranular processes at $d < d_c$ dominated by the interactions between atoms of neighboring grains and/or by the small scale sliding in grain boundaries. In materials with the grain size $d \leq d_c$ (1) dislocations are not generated (grain size d is smaller than the length of dislocation) and (2) processes in grain boundary regions play a dominant role over those inside grains [20]. Therefore, besides chemical and electronic bonding between atoms, the nano-structure of material plays a dominant role when $d \leq d_c$. It is suggested that grain boundary sliding is the reason for softening in this crystallite range. Therefore, a further increase of the strength and hardness with decreasing crystallite size can be achieved only if grain boundary sliding can be blocked by appropriate design of the material. This is the concept of design for superhard nanocomposites.

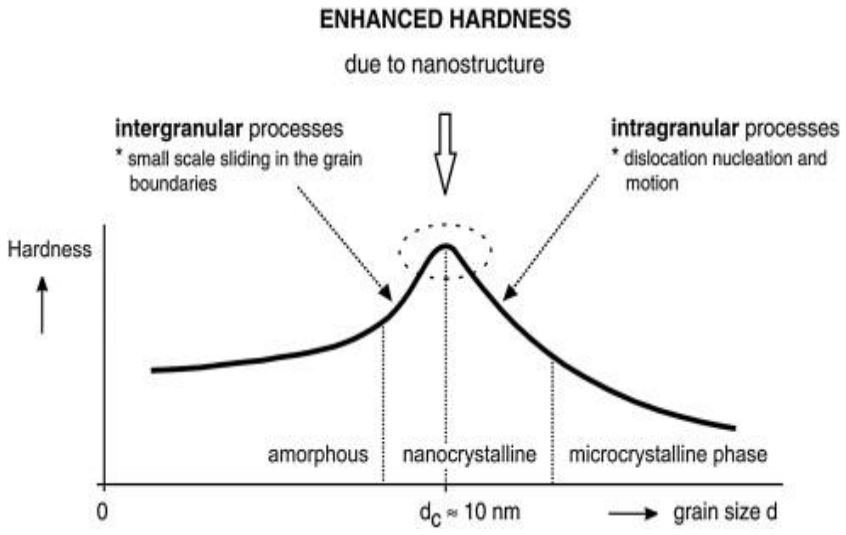

Figure 2-1 Schematic illustration of hardness as a function of the size *d* of grains [24].

As mentioned in Chapter 1, there are at least four types of nanostructures which result in enhanced hardness of nanocomposite coatings [23]. Individual nanostructures are formed under different conditions using either a sequential deposition of individual layers in the nanosize bilayers or in transition regions where the coating structure changes from crystalline through nanocrystalline to amorphous. There are three transition regions: (1) the transition from the crystalline to the X-ray amorphous material, (2) the transition between two crystalline phases of different materials and (3) the transition between two crystallographic orientations of grains of the same material. These regions are schematically displayed in Figure 2-2. From this figure is seen that to every transition region corresponds an optimal elemental composition at which nc-/a- or nc-/nc- nanocomposite coatings can be formed. The addition of one or more selected elements into a base material, e.g., the addition of Silicone Si in the nitride transition metal (TM), is very effective way to produce hard nanocomposite coatings with enhanced hardness, here TM = Ti, Zr, Hf, V, Nb, Ta, etc. [56]. The evolution of the film nanostructure in the transition from the crystalline to amorphous material is schematically displayed in Figure 2-3 [57].

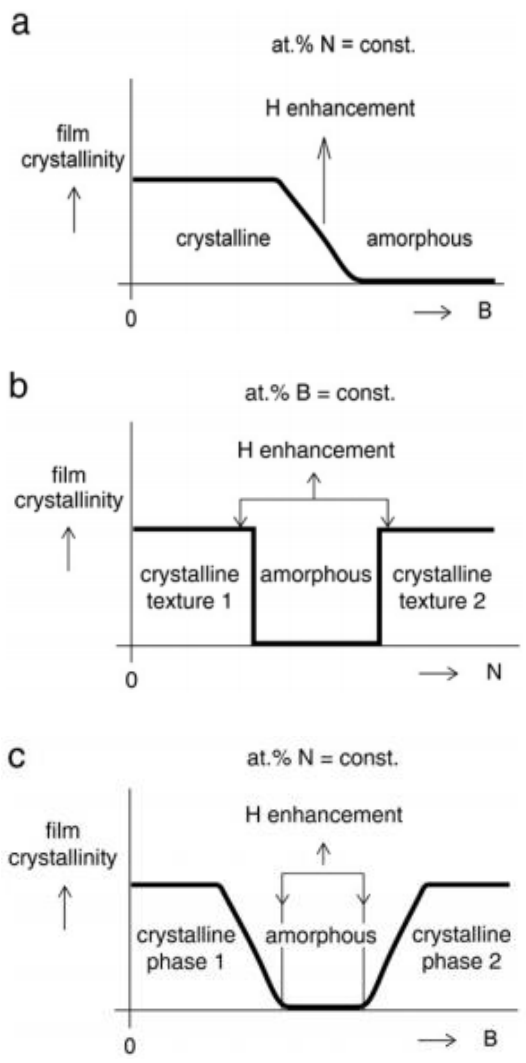

Figure 2-2 Schematic illustration of three transition regions of $A_{1-x}B_xN$ compounds: (a) Transition from crystalline to amorphous phase; (b) transition between two different preferred crystallographic orientations of the grains of the same material; (c) transition between crystalline phases of two different materials [23].

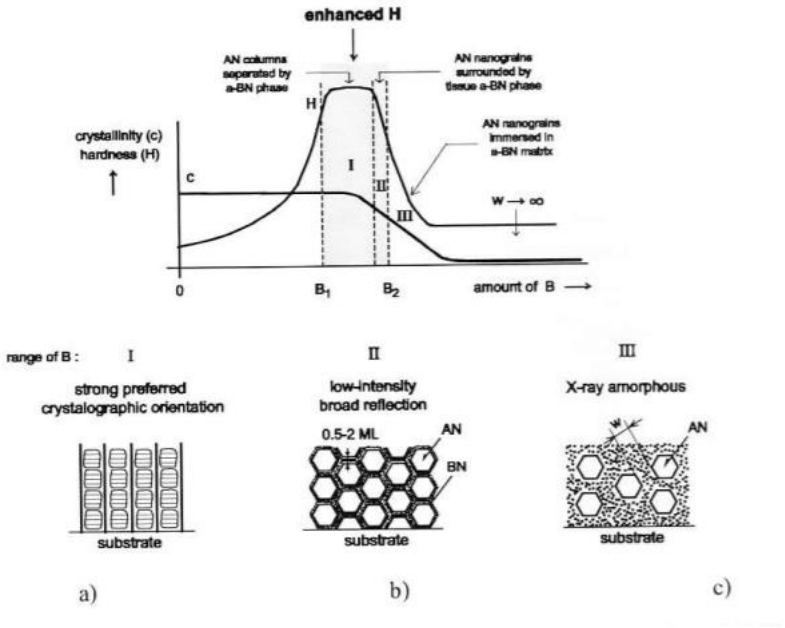

Figure 2-3 Schematic illustration of the evolution of nanostructure in two-phase A-B-N nanocomposite film with increasing amount of element B [57].

The nanocomposite protective coatings are nowadays deposited mainly as suggested by Veprek and Reiprich, [18, 58] and contain transition metal nitrides as the main component. The most popular TmN used for machining applications is TiN; the most popular supplementary elements are silicon and aluminum. For the first time, the addition of aluminum and/or silicon to TiN in sputtered thin films was reported 40 years ago [59]. Later on, it was shown by the groups of Knotek [60] and Munz [61] that the addition of aluminum to TiN improves both oxidation resistance and hardness of Ti–Al–N coatings as compared to the TiN coatings. However, segregation of Al and Ti within the (Ti, Al) N, which leads to the decomposition of fcc-(Ti,Al,)N into TiN and AlN , was classifies as a negative process. Ti–Si–N coatings with enhanced hardness and oxidation resistance were further developed by Li Shizhi et al. [58] and Veprek et al. [18]. In these coatings, Veprek and Reiprich observed formation of amorphous Si_3N_4, and made it responsible for the improvement of the oxidation resistance [62, 63]. However, TiSiN system

shows extraordinary ability as a high hardness coating, the thermal stability and oxidation resistance of this material are not sufficient for high temperature applications.

2.4 Oxidation Resistance

The oxidation resistance is one of the most attractive properties of hard nanocomposite coatings. A considerable effort has been made on the development of hard nanocomposite coatings with high oxidation resistance. As was seen in Fig 1-3, the oxidation resistance of hard coatings strongly depends on their structure, and the crystalline coatings exhibit a lower oxidation resistance compared to the amorphous coatings. The thermal stability of most of the crystalline coatings produced so far is not high enough which is below 1000 ℃ [64]. This is mainly because the oxidation resistance enhancement of the coating is based on the suppression of coating crystallization. The oxidation resistance of amorphous coatings as compared to crystalline coatings is very high at temperatures exceeding 1000 ℃ because of the lack of grains. There is no direct contact of the external atmosphere with the substrate through boundaries and reactions between the external atmosphere and the substrate are eliminated as summarized in Figure 2-5.

The present state-of-the art in the field of the oxidation resistance (OR) of hard protective non-oxide coatings based on nitrides is summarized in Figure 1-3. The OR of the coating is characterized by the increase of the coating mass Δm after its annealing to a given temperature T_a. The value of T_a corresponding to the beginning of a sharp increase of Δm from $\Delta m \approx 0$ is the maximum temperature T_{max} which determines the OR of the coating.

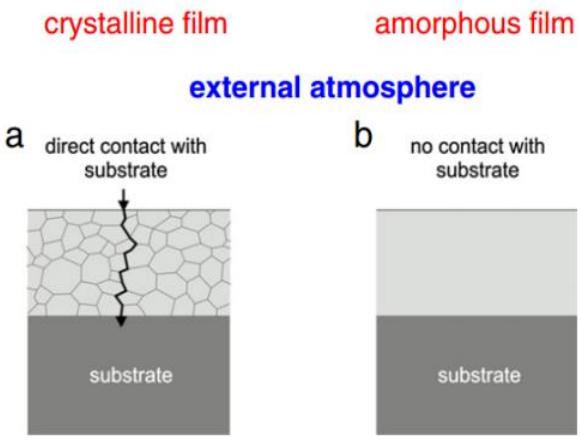

Figure 2-4 Principle of the oxidation resistance enhancement of hard nanocomposite coatings [23].

A good separation of the nanograins from each other is necessary but not a sufficient condition to protect the substrate against oxidation. It requires to select correctly the material of the substrate for different operation temperatures or to separate the substrate from the coating by a barrier interlayer. The nanocomposite coatings where the MeN_x nanograins are dispersed in the a-Si_3N_4 phase prevent direct connection between the external atmosphere and the substrate. Thereby, they should ensure a good protection of the substrate against oxidation even at temperatures when the amorphous phase start to nanocrystallize. Every change of the structure of coating and every interaction between the coating and substrate elements must be, however, avoided.

While the TiSiN system shows extraordinary ability as a high hardness coating, the thermal stability and oxidation resistance of this material are not sufficient for high temperature applications. On the other hand, TaSiN coatings with high Si content are of particular interest due to their ability to resist oxidation at elevated temperatures, up to at least 1350 ^{o}C. While a small increase in mass is noted at 1100˚C, the TaSiN coating does not undergo the rapid increase in mass

associated with oxidation as the other films do. Instead, after a small initial increase in mass, the film remains stable up to the maximum temperature tested, 1350 ºC [64].

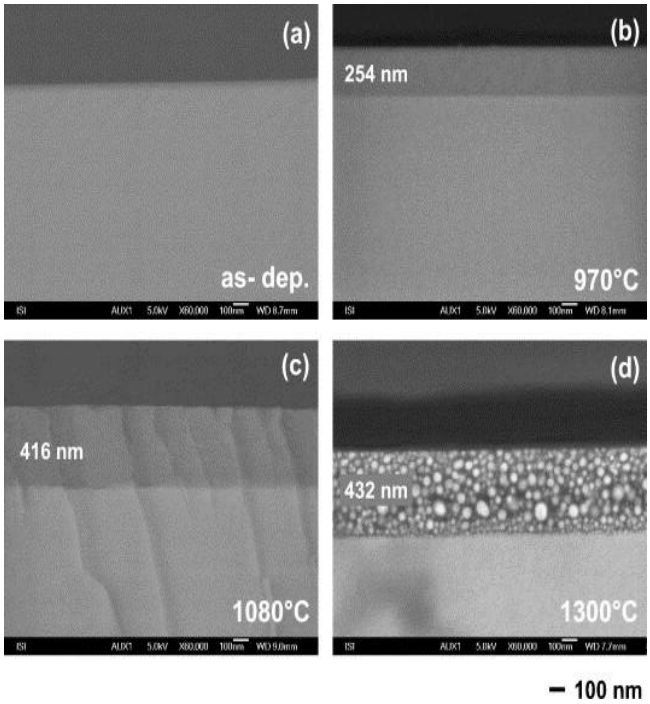

Figure 2-5 Formation of an oxide layer on high Si content TaSiN film surface at various annealing temperatures (a) as deposited, (b) 970˚C, (c) 1080˚C, (d) 1300˚C, all annealed in air [64].

The proposed mechanism suggests that at 1100˚C, Oxygen diffuses and reacts with Ta, forming a stable, passive tantalum oxide layer of a few hundred nanometers in thickness at the film surface (Figure 2-6). This oxide layer acts as a barrier to subsequent oxidation. Most publications report the TaSiN system as either completely amorphous or as a mixed system composed of Ta-Si, Ta-N, and Si-N compounds. Some compounds tend to crystallize such as TaN_x and $TaSi_x$, and others such as Si_3N_4 and SiN_x are amorphous. Reported TaSiN systems displaying high temperature oxidation stability have a much higher amorphous content than the TiSiN system, and films with Si content greater than 40 at. % exhibit the highest resistance to oxidation, but these high amorphous content films have hardness values less than 30 GPa [65-67].

2.5 Ta-Si-N: Potential candidate for High Hardness/High Oxidation Resistant Coating

Investigations carried out on Tantalum Nitride thin films, clearly indicate their potential of being used as very hard coatings. One of the papers reports theoretical hardness of 61 GPa for one of the phases of Ta-N. Some phases present in TaN at high N_2 flow and higher substrate temperature, such as orthorhombic Ta_4N and fcc TaN have theoretical hardness of 61 and 50 GPa, respectively, although other researchers have reported the fcc phase to have hardness around 20 GPa [68-69]. However, there is no consensus in the literature about the relationship between microstructure and mechanical properties of the TaN system. Also, there is a lack of detailed TEM analysis in the literature which is imperative to gain a clear understanding of the relationship between hardness and detailed microstructural characteristics. The thermal stability and oxidation resistance of TaN (800 ^{o}C) are significantly better than TiN (400 ^{o}C) and TiSiN (600 ^{o}C). Ta-Si-N nanocomposite coating with high amorphous content has been tested at higher temperatures displaying resistance to oxidation upto 1350 ˚C but these coatings lack the enhanced hardness present in TaN and TiSiN coatings [64]. As mentioned above, nanocomposite coatings based on Veprek's structure (specifically nc-TiN/a-Si_3N_4), displayed enhanced hardness and improvement in resistance to oxidation compared to single phase TiN. Application of DNG/AM nanocomposite model of hardness enhancement to the Ta-Si-N system, while controlling the amount of crystalline and amorphous phases can lead to the development of new Ta-Si-N materials with both high hardness (>30 GPa) and excellent high temperature properties (>900 ^{o}C) not currently reported in the literature. With decreased Si content and lower overall amorphous content within the film, it is possible that this system might mimick DNG/AM proposed nanostructure for hardness enhancement and achieve thermal stability and oxidation resistance at high temperatures.

2.6 Preparation of the Nanocomposite

A common characteristic of the ternary and quaternary nitride nanocomposite coatings is that they are produced via simultaneous deposition of elements with limited mutual miscibility, which partly or completely segregate (i.e., they must display thermodynamically driven segregation) during the deposition process or during the operation of the coatings (particularly at elevated temperatures) by forming nanostructured microstructures. To achieve superhardness for nanocomposites suggested by Veprek, ($TiN–Si_3N_4$), a certain ratio of the fractions (typically close to 80:20 mol %) of the two phases (nanocrystalline: amorphous) is necessary in order to provide the driving force for the segregation and resultant formation of the nanostructure. In addition, the amorphous phase must possess high structural flexibility in order to accommodate the coherency strain. Both materials should be refractory so that the operational temperature of the tools will be smaller than half of the melting or decomposition temperature. In this case the nanostructure would be stable and grain boundary sliding can be avoided [18, 25].

In order to assure that thermodynamically driven segregation and formation of the nanostructure occur during deposition the activity of nitrogen must be sufficiently high and the substrate temperature high enough to allow diffusion during film growth. For stable transition metal nitrides such as TiN and others this applies for nitrogen pressures above about 1 mbar and temperatures about 600–700 °C [25]. It is believed that with sufficiently high deposition temperature of 500-550 ^{o}C, this nanoscale morphology is achieved by way of spinodal decomposition. Spinodal decomposition refers to the situation in which the second derivative of pressure with respect to volume is negative. This results in a system which is inherently unstable, and, the result is the rapid un-mixing of a solution consisting of two mixed phases with zero activation energy. This “uphill” diffusion will continue to take place, decreasing the total free

energy of the system, until the equilibrium conditions (TiN and Si_3N_4 in this case) are reached. This is much different than typical methods of nucleation of crystalline phases, which require overcoming a substantial initial free energy barrier in order for nucleation or initial grain growth to occur. In addition, nucleation may happen only a very few times, or possibly even only once, since the nucleation of additional grains may rapidly occur in the areas immediately surrounding the initial grain. Conversely, spinodal decomposition may occur continuously and simultaneously in different physical locations throughout the coating deposition process. This type of mechanism is known for producing materials typically consisting of very fine grains, which have been shown to enhance the mechanical properties of the material. Activated chemical or physical vapor deposition techniques such as plasma CVD and PVD or reactive sputtering are most suitable for such processes.

In methods such as CVD or PVD Magnetron sputtering, where the flux of the Ti, Si, and N atoms to the substrate surface is random, a solid solution is believed to form in the initial stages. If the deposition temperature is sufficiently high as to allow the spinodal decomposition proposed in the literature, then the formation of a strong nanocomposite structure will occur during the coating deposition process. It has been shown that this decomposition is kinetically controlled by bulk diffusion, since the decomposition of the mixed phases is faster than Si diffusion. From the published data it appears that higher substrate temperature and bias in plasma PVD promote phase segregation which results in higher hardness [18]. To summarize, the formation of a nanocomposite requires high plasma density and temperature as was demonstrated for various systems.

2.6.1 Sputter Deposition

PVD methods are commonly used in the manufacture of thin films and coatings. PVD methods include evaporation, sputter deposition, cathodic arc deposition and pulsed laser deposition. In all methods of PVD, the constituent species, atoms or molecules are produced by either evaporation of a solid source or by using energetic gaseous ions in plasma to knock off or sputter the atoms from a source target. These atoms travel through a vacuum of very low-pressure gas phase, impinge on the substrate and finally condense on the surface to form the film.

In a sputter system, an inert gas such as Argon is fed into the chamber at low pressure. A voltage is applied across the two electrodes and plasma is created. The plasma contains neutral Ar atoms, Ar ions and free electrons and is a conducting medium. Free electrons present in the chamber are accelerated away from the negatively charged cathode (target). Some of these electrons collide with the sputtering gas like Ar, resulting in a Ar+ ion and a electron. The positive ions are then accelerated to the negatively biased target and dislodge or sputter the target atoms. These atoms are then free to travel through the plasma as a vapor and strike the surface of the wafers and form the deposited film. If the target is conductive, we use DC mode of sputter deposition and to deposit nonconductors like lightly doped silicon, we use RF method. During this process, number of free electrons will collide with Ar+ ions to form neutral Ar atoms. When the energized electron returns to the ground state, a photon is released in the reaction, resulting in the plasma glow.

In sputter deposition, the target or source sputtering rate is important. Sputtering occurs when the incoming ion transfers enough energy to the target surface to break bonds holding the target atom in place. This depends on the energy and mass of the ions and the target material. The yield, which is the number of atoms from the target per incident ion depends on energy of ion,

voltage across the sheath and the direction of incidence of the ions. Multiple targets may also be used in these systems for co-sputtering.

2.6.1.1 Reactive Sputter Deposition

In this method, a reactive gas is introduced in the chamber along with the sputtering gas. In case of TaN, the plasma can furnish energy to the N_2 to allow it to dissociate into atomic nitrogen, which can then easily react with the Ta. The reaction usually occurs either on the wafer surface or near the target itself and not in the plasma. Controlling the stoichiometry of reactively sputtered films is sometimes difficult.

2.6.1.2 Magnetron Sputter Deposition

In both conventional DC and RF sputtering, the efficiency of ionization from energetic collisions between electrons and atoms is rather low. Most electrons lose their energy in non-ionizing collisions and as a result, only a small percentage of them take part in the ionization process with Ar atoms. In RF plasmas electrons gain energy directly from oscillating RF fields, increasing the ionization efficiency to some level. However, the overall deposition rate is still low. In this technique, magnets are used to increase the percentage of electrons that take part in ionization. A magnetic field is applied which traps the electrons near the target surface and causes them to move in a spiral motion until they collide with an Ar atom. The advantages of this technique are several like unintentional wafer heating is reduced, since dense plasma is confined near the target. In addition, lower Ar pressure can be utilized as ionization efficiency is high and film quality would be better, due to less Ar incorporated in them.

2.6.1.3 Bias Sputtering

Sputtering of the wafer is usually desirable. One application would be for pre-cleaning the wafer before actual deposition. Another application is bias sputter deposition, where deposition

and sputtering of the wafer are done simultaneously. A negative bias relative to the plasma is applied to the substrate, which is electrically isolated from the chamber walls. Positive Ar atoms from the plasma will now be accelerated to the wafers to the substrate and sputter off atoms. The energy of the ions can be controlled by controlling the substrate bias. In sputter cleaning, no deposition is allowed to occur on the wafer surface by usually using a shutter to block sputtered material from the target. A controlled thickness of the material is sputtered off the wafer, removing any contaminants and oxides. In bias sputtering, conditions are chosen so that more deposition occurs than sputtering. A more planarized film is obtained because of bias sputtering. Also, properties of the film being deposited can be changed by changing the substrate bias. These properties include residual stress, density, resistivity and mechanical properties. The drawback of this method is that the net deposition rate is slow.

Chapter 3 Thin Film Synthesis and Characterization

Formation of a nanocomposite requires high plasma density and temperature. Activated chemical or physical vapor deposition techniques such as plasma CVD and PVD or reactive sputtering are most suitable for such processes.

The first part of the research was deposition, analysis and design of TaN coatings. These coatings were fabricated using a home-built hybrid Plasma Enhanced Physical Vapor Deposition (magnetron sputtering) system, followed by detailed characterization. Diffractive methods including XRD and HRTEM were used to gain a detailed understanding of the crystal structure and nanocrystalline morphology of the coatings in relation to their properties. AES and XPS was used to obtain the composition and chemical states of the coatings. Nanoindentation, tribological wear testing, and optical profilometry aided in the understanding of the mechanical properties including the hardness, wear resistance, and coefficient of friction of the deposited coatings. The goal was to gain fundamental knowledge of the effects of the deposition parameters on the microstructure and mechanical properties of TaN films and hence design a high hardness oxidation resistant coating. Knowledge gained during the processing and characterization of TaN films served as a model system to study and design another high potential coating, TaSiN.

3.1 Synthesis of TaN/TaSiN Films

Reactive PVD Magnetron Sputtering was used to deposit TaN/TaSiN films. The sputtering system in the Surface and Nano Engineering Laboratory (SaNEL) is a very versatile system and many experimental parameters including pressure, gas mixture, targets, power to the magnetrons (DC and RF), substrate bias, substrate temperature, distance between the target and substrate, and substrate rotation can easily be varied. Figure 3-1 shows the home-made hybrid plasma assisted magnetron sputtering system in SaNEL. The stainless-steel chamber has a cylindrical shape with

47 cm diameter wide and 50 cm height. The system has three 2-inch diameter magnetron guns mounted at the bottom of the chamber (Fig 3-2). Each magnetron gun can be easily connected to DC or RF plasma power capabilities. The position of the magnetron gun is designed to have 30 degree inclination to the substrate holder center with a target-substrate distance about 6 - 10 cm. The sputtering target holder and substrate holder in the chamber have a face to face arrangement serving as electrodes. The magnetron guns can support targets with thickness of 0.125", 0.185" or 0.250". The targets can be shielded using a pneumatic shutter above the magnetron gun. The substrate can be rotated and heated up to 900°C (setting temperature). The substrate holder is a 10-cm diameter plate (Fig 3-3) where the samples can be mounted and has rotation capability. The substrate can be either RF or DC biased up to 50 W and 1000 V, respectively.

Figure 3-1 PVD reactive magnetron sputtering system in Surface and Nano Engineering Laboratory.

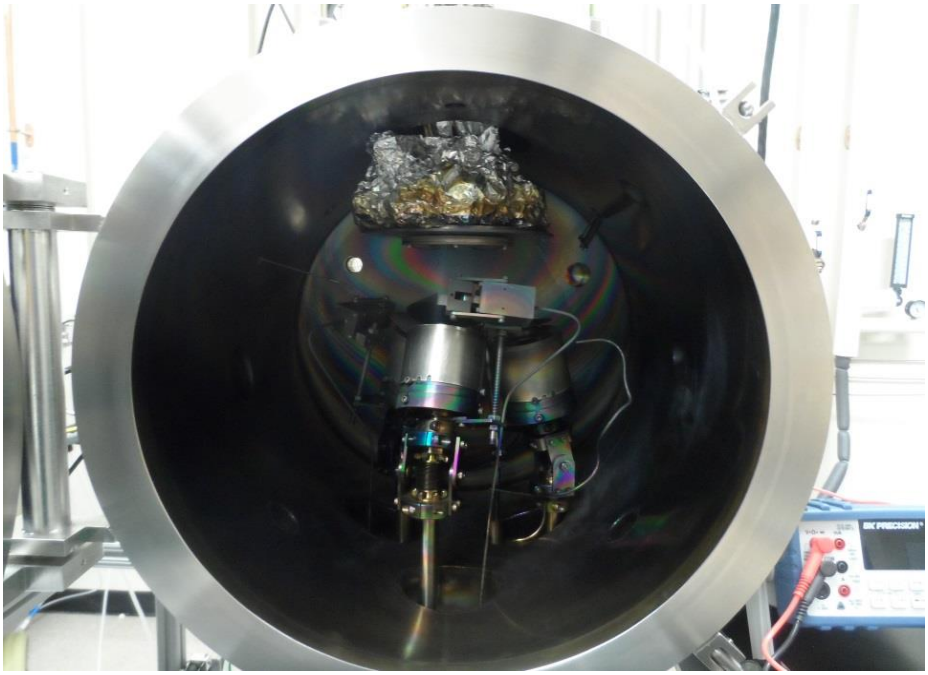

Figure 3-2 Magnetron guns inside the Sputtering Chamber.

Figure 3-3 Silicon wafer loaded on the substrate holder.

Argon gas with a purity of 99.99% was introduced into the system chamber as a medium to start and maintain a glowing plasma. The gas flow was controlled using a Unit Instruments mass

flow controller to meet the pressure requirement during the deposition. The deposition chamber is pumped down using a mechanical pump and a cryopump is used to get pressure range of ~ 10^{-7} Torr. During the deposition, very precise pressure control is maintained using an automatic gate valve in conjunction with an MKS 146C PID controller. A thermocouple gauge measures the roughing line pressure and an ion gage located at the backside of the sputtering chamber measures the chamber pressure when the valve gate is open and the cryopump accesses the chamber to achieve higher vacuum. All the magnetron guns and substrate holder were cooled circularly using a Thermo Scientific NESLAB RTE 740 water chiller to avoid heating damage to all the guns.

3.2 Reactive Magnetron Sputtering Experimental Conditions

Experimental sputtering conditions were specifically selected based on a thorough review of the literature and several preliminary experiments carried on TiSiN thin films (which was an ongoing project) in the SaNEL lab designed to gain an understanding of sputtering rate vs. pressure and/or power to the magnetron guns. Because MeSiN composite thin films properties degrade significantly with the presence of only trace amounts of oxygen impurities, achieving a low base pressure is of high importance. The base pressure should be in the range of 10^{-7} Torr. TaN and TaSiN coatings are typically prepared with Nitrogen as the reactive gas and Ta and Si target, respectively. In the case of MeN/MeSiN coatings, the pressure of the N_2 reactant gas must be high enough within the chamber to obtain the proper stoichiometry required within the film, but not so high as to poison the targets used in the deposition. The target to substrate distance is typically between 6-10 cm, and a negative bias is typically applied at the substrate in order to limit the incorporation of oxygen atoms within the coatings [72]. Also, substrate bias has been shown to refine the film microstructure due to re-sputtering. In addition, it has been shown that the substrate temperature during deposition is very important to obtain the previously discussed nanocrystalline

structure. Some nc-TiN/a-Si_3N_4 coatings have been created by PVD using deposition temperatures of 200°C and 150 mm between the target and the substrate [73]. Other sources claim that the minimum temperature required for deposition of composites using PVD which have full segregation between their TiN and Si_3N_4 phases, stoichiometric formation of TiN, and hardness enhancement is 500-700°C, and that distance less than 10 cm, between the substrate and the target is required to have sufficient plasma density at the substrate [74].

As mentioned experimental sputtering conditions were specifically selected based on literature review and the initial experiments carried on TiSiN thin films in the SaNEL lab. The TaN films were deposited on Si (100) p-type wafers. The wafers were cleaned with acetone prior to loading in the chamber. The chamber was roughed down to 20 mTorr using mechanical pump and then exposed to the cryo pump by opening the gate valve. A low base pressure in the range of 10^{-7} Torr was achieved before film deposition, and a low working pressure of 5 mTorr was used, to limit the degradation of the films with presence of any trace amounts of oxygen impurities. Each of the targets, as well as the substrate was cleaned for 1 minute with Argon plasma before beginning the film deposition. Sputter cleaning allows good adhesion of the deposited film by eliminating any surface contamination. Rotation was applied to ensure uniform deposition from the magnetron gun involved in the depositions. A series of TaN thin films were deposited with varying N_2 content, varying bias and varying temperature. The substrate heater was carefully calibrated and most of the experiments were carried out at 550 ^oC. Some TaN films were also deposited at 350 ^oC, to determine the effect of temperature on the mechanical properties of the films. Bias ranging from -50 V to -300 V was applied at the substrate to determine the effect of bias voltage on crystal structure and film hardness. The Ta target was loaded into the front magnetron, and 50 W DC power was applied. For TaSiN, the Si target was loaded in the left

magnetron and 13 W pulse dc power was applied. The N_2/Ar ratio was adjusted by controlling their flow rates. The N_2 percentage was varied from 2.5 % to 25 % in case of TaN and 7% to 20% in case of TaSiN. Deposition time was 1 hour for all films.

3.3 Characterization of TaN/TaSiN Thin Films

Characterization techniques such as XRD, HRTEM, AES, XPS, SEM were used to study the crystal structure, detailed microstructure, composition and surface morphology of the films respectively. Nanoindentation and tribological wear testing were used to study mechanical properties including hardness, modulus and frictional wear.

3.3.1 XRD

X-Ray Diffraction was used to determine what crystalline phases are present in the films deposited at varying conditions. It was carried out on a Bruker D-8 Advance X-Ray Diffractometer with a Cu Kα radiation source and a wavelength of 1.54 Å. All scans were low angle detector scans. The acceleration voltage and filament current were set at 40 kV and 40 mA, respectively. A small step size of 0.03° and a dwell time of 2 seconds was used to obtain high resolution scans.

3.3.2 AES and XPS

The elemental composition and chemical states were investigated using AES and XPS conducted in a Perkin–Elmer Phi 560 ESCA/SAM system using a non–monochromated Al Kα excitation source. The films were sputter cleaned in an Ar environment for 4 min prior to measurement. Survey scans were conducted in the 0 – 1200 eV range with 0.1 s dwell time. The Casa XPS software was used for XPS and AES spectra analysis. The spectra of the films were calibrated using the C 1s peak at 284.5 eV.

3.3.3 HRTEM

The microstructure of the films was studied by HRTEM. Cross section specimens were prepared by the procedure of mechanical grinding, polishing, dimpling and Ar ion milling. Selected–area electron diffraction (SAED) patterns and HRTEM images were recorded in a Hitachi H–9500 electron microscope (300 keV).

3.3.4 Nanoindentation

Hardness tests were carried out on a Hysitron Ubi 1 Nanoindenter with a cube corner tip. The hardness and elastic modulus were recorded for 9 indentations (3x3 matrix). The average of the values was calculated. Depth controlled indentations were performed at less than 10% of the coating thickness, so that the hardness effect of the underlying substrate is avoided. The films were mounted onto magnetic disks using crystal bond.

3.3.5 Optical Profilometry

The thickness and surface roughness of the film were measured by a Veeco NT-9100 Optical Surface Profilometer. The thickness was measured by calculating the step height between the film and the non-deposited substrate using a 5X objective. Surface roughness, R_a uses the arithmetic average of the absolute values of the height of the sample to estimate the roughness of a surface. Due to presence of residual stresses TaN films have some curvature. The radius of curvature is measured by the profilometer. This value is then plugged in the Stoney's equation, to calculate the residual stress present in the films.

The equation below is the Stoney's Equation

$$\sigma_f = \frac{E_s d_s^2}{6(1-\nu_s)} * \frac{1}{d_f} * \frac{1}{R}$$

where E_s, d_s, and ν_s are the Young's Modulus, thickness, and Poisson's Ratio of the Si (100) substrate, respectively, d_f is the thickness of the film, and R is the delta radius of curvature between the Si wafer before and after film deposition.

3.3.6 Tribological Testing

Pin on disc experiments were performed on TaN films to determine their tribological. A 6 mm alumina ball was used and a force of 1N was applied. The test run was 100 m. Coefficient of friction and overall wear rate were determined. Wear rates of the films were determined by taking a number of 2-D profiles of the wear track using the optical profilometer. The area under each of the profiles was calculated, and the average value of 3 profiles was taken. The calculated area was multiplied by the circumference of the wear track to find the wear volume. The wear rate is further obtained by dividing the wear volume with the load applied and the sliding distance (mm^3/Nm).

3.3.7 SEM

A Hitachi S-3000N Variable pressure SEM was used to obtain further supplementary data for MeSiN films. A high vacuum setting, a working distance of 15 mm, and an electron voltage of 10-15 keV were used to obtain images of the surface morphology of the films.

Chapter 4 Microstructure and Property Investigation of Tantalum Nitride Films

4.1 Background

Materials based on the nitrides of transition metals have attracted considerable interest because of their high hardness, high temperature oxidation resistance and stability, and high wear resistance which give rise to various application. Among the different transition metal nitrides (TiN, CrN, HfN, ZrN, etc.) TaN is gaining increasing interest due to its excellent chemical and physical properties. It is chemically inert, corrosion resistant and has ability to resist oxidation up to 800 ^{o}C.

Ta-N is a widely used material for producing hard coatings, wear resistant layers, thin film resistors, diffusion barriers in integrated circuits, and mask layers for X-ray lithography [30, 71, 75]. The Ta–N system shows a variety of compound solutions such as body centered cubic (bcc) TaN, hexagonal (hex) TaN, hex Ta_2N, face centered cubic (fcc) TaN, hex Ta_5N_6, tetragonal Ta_4N_5 and orthorhombic $Ta_6N_{2.5}$, Ta_4N, Ta_3N_5 with differing physical, chemical and mechanical properties [70-87]. The reported values of hardness for hex Ta_2N, fcc TaN, orthorhombic $Ta_6N_{2.5}$ and orthorhombic Ta_4N are 31 GPa, 20 GPa, 30.8 GPa and 61.8 GPa respectively [68, 69, 81, 88-90].

Tantalum nitride (TaN) was studied as a model system to develop and investigate another high potential transition metal silicon nitride, Ta-Si-N system, with the overall goal of synthesizing advanced hard ($\geq$ 30 GPa), high oxidation resistant (above 1000^{o}C) coatings. Production of Ta-N by reactive sputter deposition is a well–established technique. Most of previous studies have reported on the hardness of various Ta-N phases but their microstructure in relation to mechanical properties is scarcely examined. Getting a clear understanding of the effect of deposition

parameters on the microstructure and how the microstructure affects coatings properties is imperative to design advance coating systems.

In this work, a home-made plasma assisted RF magnetron sputtering system has been used for depositing TaN films on Si (001) substrates. TaN films with different crystal structures and microstructures were obtained at different deposition conditions. The effect of varying deposition conditions on the crystal structure, microstructure and hence mechanical properties have been discussed in detail.

4.2 Experimental Details

An extensive literature review was performed to select initial conditions for deposition using home-built hybrid Plasma Enhanced Chemical Vapor Deposition system in SaNEL. From these preliminary conditions, parameters were selected and adjusted as needed based on experimental results in order to further increase the hardness of the coatings.

The total gas flow (Ar + N_2) was kept constant at 25 sccm. The substrate temperature was held at a temperature of 550 ^oC for most experiments. Based on an extensive literature review, it was clear that oxygen impurities have detrimental effects of the mechanical properties of transition metal nitride systems. Therefore, a negative bias was always applied at the substrate to repeal O^{2-} ions, and the working pressure was kept very low at 5 mTorr to discourage the presence of impurities within the sputtering chamber. Although several target to substrate distances were explored for other ongoing experiments at SaNEL, coatings in this case were deposited at ~10 cm distance, since this intermediate distance allowed for both sufficiently high deposition rate and acceptable coating uniformity.

Three sets of experiments (1. Effect of varying N_2/Ar gas ratio, 2. Effect of varying substrate bias, 3. Effect of varying deposition temperature) were designed to investigate the effects

of varying deposition parameters on the crystal structure, chemical states, microstructure and hence mechanical properties of Ta-N films.

1. To determine the effect of varying N_2/Ar gas ratio in the films, experiments were carried out at –100 V substrate bias (E_B) with a total gas (N_2+Ar) flow rate of 25 sccm. The N_2 content was varied in the gas mixture from 25% to 3%. A select set of experiments was also carried out at –200 V E_B while varying the content of N_2 from 7% to 2.5%. Once the effect of varying N_2 content on mechanical properties of the coatings was established, the coatings were fine-tuned by adjusting additional deposition parameters such as substrate bias and temperature to obtain high hardness Ta-N films.
2. To determine the effect of varying E_B, experiments were carried out with 5% N_2 content with a total gas (N_2+Ar) flow rate of 25 sccm. The E_B was varied from -50 V to -200 V. The bias at the substrate was varied in order to determine the effect of increased energy presence at the substrate during film deposition, since it has been previously shown that substrate bias can have the effect of fine nanostructure refinement through the continued re-sputtering of the coating surface.
3. To determine the effect of varying temperature, experiments were carried out with 5% N_2 content with a total gas (N_2+Ar) flow rate of 25 sccm and -100 V E_B. The substrate temperature was varied from 550 ^oC to 350 ^oC. A select set of experiments was also carried out at –200 V E_B.

Rotation was set at 15 rpm for all films to ensure uniform deposition. Deposition conditions for TaN are given in Table 4-1.

Table 4-1 Deposition conditions for TaN films.									
Film	**Substrate**		**Ta Target**			**Volumetric Flow Ratio (sccm)**		**N_2 %**	**Temp. ^oC**
	Bias (V)	Current (mA)	Power (W)	Volt. (V)	Current (mA)	Ar	N_2		
S100N25	100	13	50	320	183	18.75	6.25	25%	550
S100N15	100	13	50	294	200	21.2	3.75	15%	550
S100N10	100	13	50	289	206	22.5	2.5	10%	550
S100N7	100	14	50	290	200	23.25	1.75	7%	550
S100N5	100	14	50	286	205	23.75	1.25	5%	550
S100N3	100	17	50	266	50	43.5	1.3	3%	550
S50N5	50	13	50	284	209	23.75	1.25	5%	550
S200N2.5	200	19	50	259	230	48.7	1.3	2.5%	550
S200N7	200	15	50	281	212	23.25	1.75	7%	550
S100N5 TEMP 350	100	14	50	274	214	23.75	1.25	5%	350
S200N5 TEMP 350	200	16	50	268	211	23.75	1.25	5%	350

4.3 Effect of Varying N_2/ (N_2 + Ar) Gas Ratio on Film Properties

The aim of this study was to investigate the effects of varying N_2 percentage in the gas mixture on the crystal structure, elemental composition, chemical states, microstructure evolution and eventually mechanical properties of the films.

4.3.1 XRD Analysis

Figure 4-1 shows the low–angle XRD of the Ta–N films deposited at E_B = -100 V with the N_2 content varying in the gas mixture from 25% to 3%. The XRD spectra of the films with 25% – 10% N_2 show diffraction peaks at 2θ angles of 35.5°, 41.3° and 60.1° corresponding to lattice spacing of 2.5 Å, 2.16 Å and 1.53 Å, respectively. These can be identified as the (111), (200), (220) peaks of fcc δ–TaN (PDF#49-1283). The 25% N_2 film seems to be textured along (111) plane and as the N_2 content is decreased from 25% to 10%, the (200) peak becomes equally strong as the (111) peak. Decreasing N_2 content to 7% results in one major peak at 2θ angle of 35.3° with lattice spacing of 2.5 Å, and other small peaks at 2θ angles of 41.07° and 59.79°, with lattice spacing of 2.18 Å and 1.54 Å, respectively. These can be also identified as the (111), (200) and (220) diffraction peak of the fcc TaN. The 7% N_2 film seems to have a noticeable (111) texture. All the peaks exhibit a shift to lower angles compared to (111), (200), (220) diffraction of the fcc TaN crystal structure reported in the powder diffraction file (PDF#49-1283). This is most likely caused by the compressive residual stress in the films. Further decrease in N_2 to 3% results in diffraction peaks at 2θ angles of 33.8°, 38.4°, and 60.4° with lattice spacing 2.63 Å, 2.32 Å and 1.53 Å, respectively. These can be identified as the (100), (101), (110) planes of hex Ta_2N (PDF#26-0985). It should be noted that the (002) reflection of the hex–Ta_2N is expected to be present in the shoulder around 2θ angle of 36.5°.

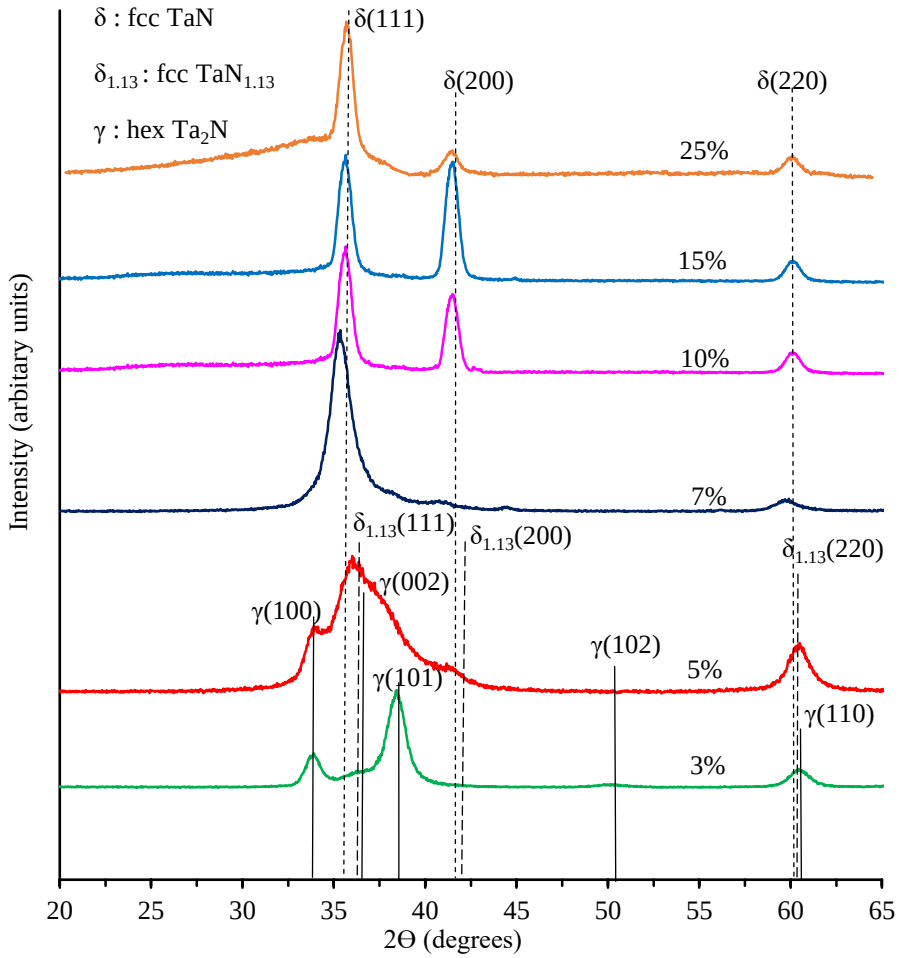

Figure 4-1 Low Angle XRD scan of TaN films deposited at a substrate bias of -100V and N_2 varying from 25% to 3%.

The XRD of the film deposited with 5% N_2 shows at least two peaks at 2θ angle of 33.9° and 60.40°, and a broad peak around 36.02° which in turn is comprised of many peaks. The XRD patterns of the films with 3% and 5% N_2 are shown separately in Figure 4-2. The peaks at 33.9°, 36.02°, 60.40° with lattice spacing 2.63 Å, 2.49 Å and 1.53 Å, respectively can be identified as the (100) plane of the hex Ta_2N, and (111) and (220) plane of fcc $TaN_{1.13}$, respectively. Thus, the XRD spectrum for the film with 5% N_2 shows a mixture of phases and is a transition from a single phase fcc TaN (from 25% – 7% N_2) to mainly hex Ta_2N (3% N_2). We should note that since the film with 5% N_2 had a mixture of phases, the other expected planes such as (002), (101) of the hex

Ta_2N and (200) of the fcc $TaN_{1.13}$ phase are present in the broad shoulder extending from a 2θ angle of 35.83° to about 42° as shown in Figure 4-2. The hex Ta_2N phase which dominates in the 3% N_2 film was still emerging in the 5% film. The hex Ta_2N phase is well reported in the literature [91]. It has been reported that TaN has a defective structure and deviations from stoichiometry are frequent [92]. The theoretical analysis suggests that in the Ta–N system, Ta_2N and TaN phases are the stable and metastable structures, respectively; however, the energy difference for these two tantalum nitrides is very close allowing them to coexist [93].

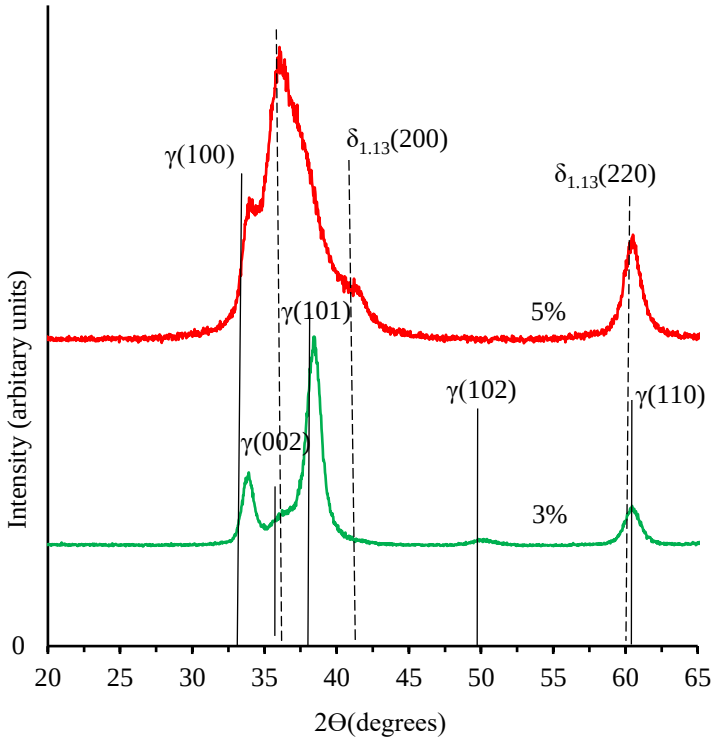

Figure 4-2 Low Angle XRD scan of TaN films deposited at a substrate bias of -100V and N_2 varying from 5% to 3%.

Figure 4-3 shows the low–angle XRD of films deposited at E_B = –200 V and varying the N_2 content from 7% to 2.5%. The trend observed for this set of experiments was similar to that shown by the films deposited at similar conditions but at E_B = –100 V. For the film with 7% N_2, the peaks at 2θ angle of 35.15°, 40.14° and 59.5° with lattice spacing 2.53 Å, 2.23 Å and 1.55 Å,

respectively can be identified as the (111), (200) and (220) plane of fcc TaN. The peaks in this case are broad and at slightly lower diffraction angles (due to residual stresses) than the film deposited at E_B = –100 V with the same gas ratio.

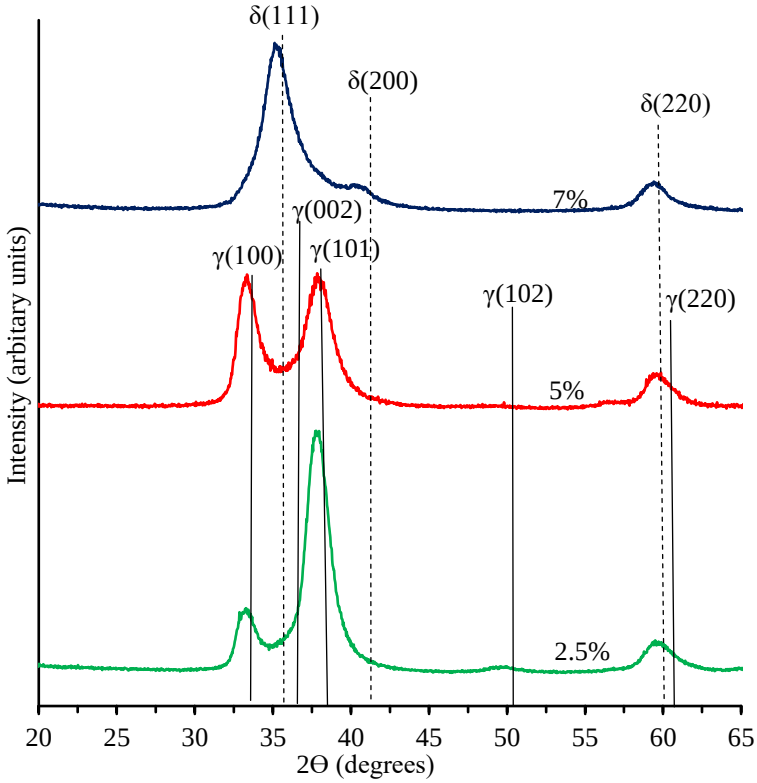

Figure 4-3 Low Angle XRD scan of TaN films deposited at a substrate bias of -200V and N_2 varying from 7% to 2.5%.

The broader peaks indicate refinement in the film microstructure (resulting in decreased grain size) caused by the consistent energetic bombardment at higher bias. As the N_2 content is decreased to 5%, diffraction peaks at 2θ angle of 33.34°, 37.91° and 59.6° with lattice spacing 2.6 Å, 2.37 Å and 1.54 Å, respectively are observed. These can be identified as the (100), (101) and (220) plane of hex Ta_2N. In the case of E_B = –200 V, a transition from fcc TaN to hex Ta_2N was facilitated without the broad peak (comprising a mixture of phases) observed at E_B = –100 V for the same N_2 percentage. This indicates a faster transition promoted by the higher energy

of the system at a higher E_B. As the N_2 content is further decreased to 2.5%, hex Ta_2N is still the dominant phase textured along the (101) orientation. The (101) texture is more pronounced compared to the film deposited with almost same content of N_2 (3%) but at E_B = –100 V.

Figure 4-4 shows the variation in the deposition rate (nm/h) of the films deposited at E_B of –100 V and – 200 V. The thickness of the films deposited at E_B = –100 V was around 500 ± 30 nm except the one deposited with 7% and 5% N_2. The 7% N_2 film was textured along the fcc (111) plane and this preferred orientation can be the reason for its high deposition rate. The 5% N_2 film comprises mainly of fcc $TaN_{1.13}$ but it also contains other phases, resulting in a slight decrease in deposition rate compared to the 7% N_2 film. However, the trend from 7% to 25% N_2 and 5% to 3% N_2 was a decrease in deposition rate and this could be due to more uniform, non-textured microstructure.

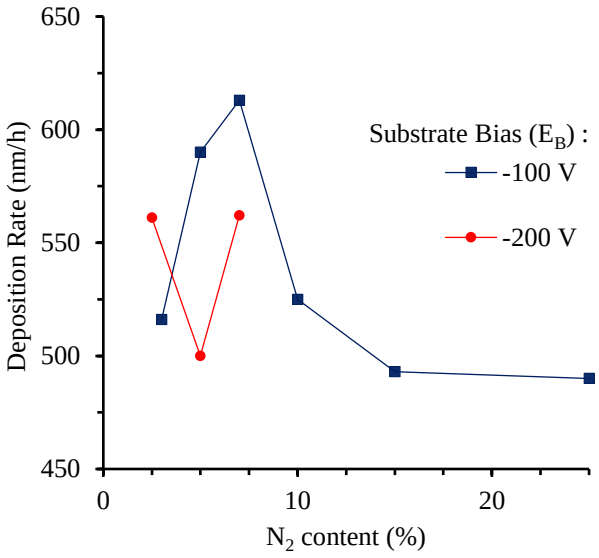

Figure 4-4 Variation in the deposition rate (nm/h) of the films deposited at E_B of –100 V and – 200 V.

The deposition rate of the films deposited at higher bias (in this case -200 V) is typically lower due to resputtering. The films deposited with 7% and 2.5% N_2 have higher deposition rate

compared to the 5% film. The higher deposition rate for these films is due to their texture, the 5% film being nontextured hex Ta_2N. However, the film deposited with 2.5% N_2 at E_B = -200 V has higher deposition rate than the film deposited with almost same N_2 content (3%) but at E_B = -100 V. Both films have preferred orientation along the (101) plane but analysis of their respective (101) peak heights shows a significant higher texture for the film deposited at E_B = -200 V resulting in higher deposition rate.

4.3.2 XPS Studies

The composition and chemical state of Ta–N films were examined by AES and XPS respectively. All binding energy values have been corrected for the charging effect with reference to the adventitious carbon 1s peak at 284.6 eV. Figure 4-5 shows the evolution of the elemental composition of the reactively sputtered Ta–N films deposited at E_B = –100 V with N_2 content varying from 25% to 3%.

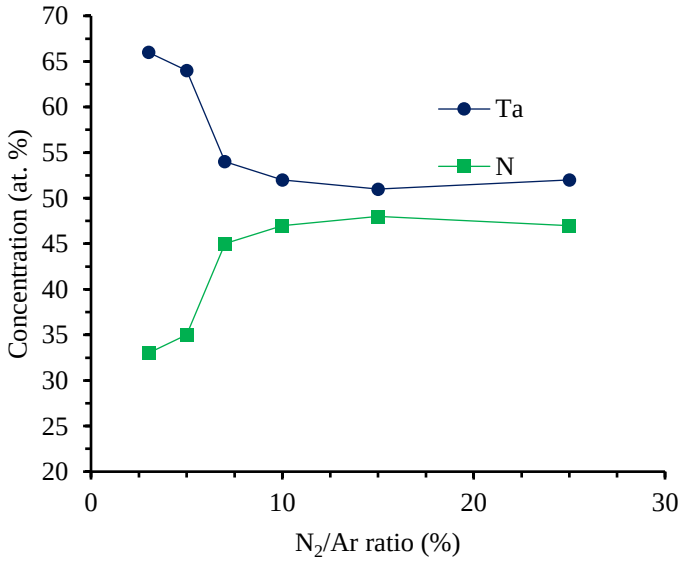

Figure 4-5 Evolution of the elemental composition of the reactively sputtered Ta–N films deposited at E_B = –100 V with N_2 content varying from 25% to 3%.

The elemental percentage composition was determined from peak to peak intensity from the differentiated spectrum. A decrease in N concentration and increase in Ta concentration can be observed as the N_2 content in the gas mixture is decreased from 25% to 3%. The Ta:N ratio is approximately 1:1, 1:1.8, 2:1 for 25% - 7%, 5% and 3% flow ratios respectively. This agrees well with the phases identified by XRD.

The high-resolution Ta 4f and N 1s spectra for films with N_2 content varying from 25% - 3% are shown in Figures 4-6(a) and (b), respectively. As shown in Figure 4-6(a) the Ta 4f peaks are at higher binding energies compared to that of metallic Tantalum (Ta $4f_{7/2}$ ~ 21.7 eV). This peak shift indicates the transition from a metallic (Ta $4f_{7/2}$ ~ 21.7 eV) to a nitride (Ta $4f_{7/2}$ ~ 24.7 eV) chemical state. We can also observe that as the N_2 content is increased from 3% to 15%, the binding energy of Ta $4f_{7/2}$ peak is shifted to slightly higher values (23.1 eV at 3%, 23.5 eV at 5%, 23.7 eV at 7%, 23.8 eV at 10%, 23.8 eV at 15%) indicating a change in chemical state. At 25% N_2, the intensity of the Ta 4f peak decreases and binding energy of Ta $4f_{7/2}$ shifts to 23.2 eV. This indicates presence of some other chemical states or defects at the surface which resulted in the low binding energy of Ta 4f peak. Decrease in the intensity of the Ta 4f peak at higher N_2 was also reported by Arshi *et al.* [94]. As shown in Figure 4-6(b), the N 1s peak is around 397 eV and this corresponds to metal nitride state, although the Ta $4p_{3/2}$ peak at 403.5 eV is almost constant. It can also be seen that there is a decrease in the intensity of the N 1s peak with decreasing N_2 content, which is consistent with the compositional analysis (Figure 4-5). For the 25% film, the N 1s peak showed a slight shift to a lower binding energy, similar to the shift in Ta4f peak, possibly due to excess N in the film. In the case of 3% and 5% N_2, the N 1s peak shows some broadness as compared to the sharp peak for the 25% N_2. This broad peak corresponds to two binding energies, 398.1 eV and 397.2 eV and can be attributed to presence of two phases in the film.

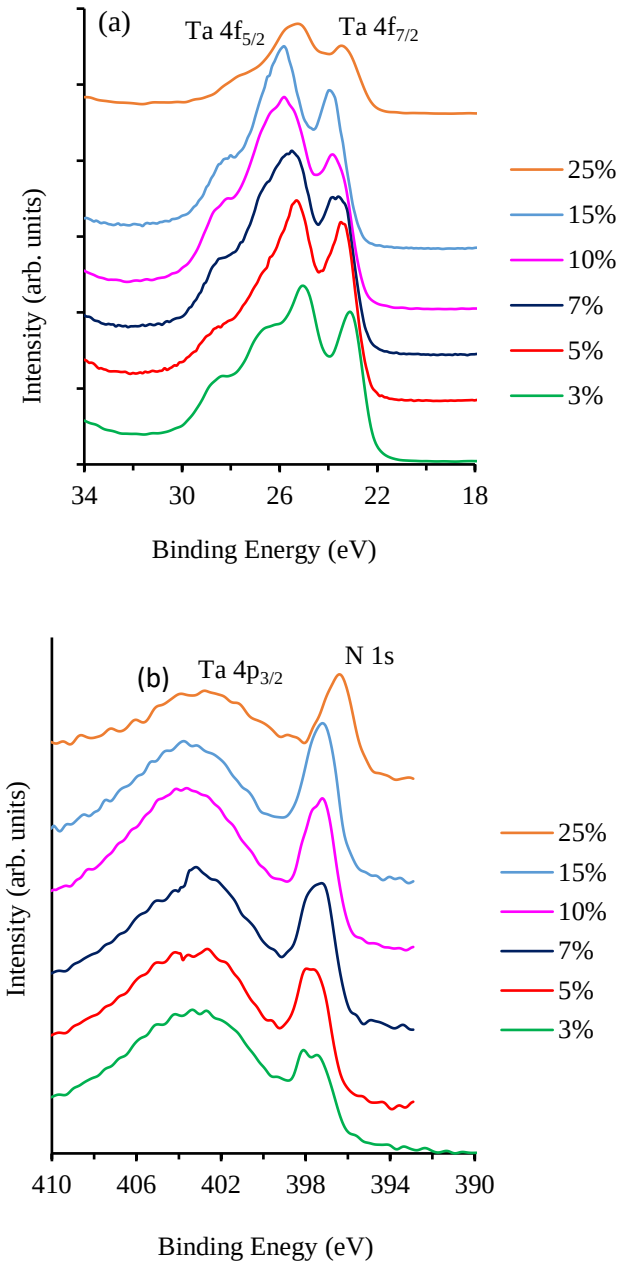

Figure 4-6 High resolution (a) Ta 4f (b) N 1s spectra for films with N_2 content varying from 25% - 3%.

Figures 4-7(a), (b) show the deconvoluted peaks for films deposited with 3% and 25% N_2, respectively, where the solid black line represents experimental values and dashed lines represent the deconvolution. After deconvolution, the spectra for these films are composed of two sets of Ta 4f doublets. Considering, the split energy by spin orbit coupling of $4f_{7/2}$ and $4f_{5/2}$ in Ta 4f as 1.9

eV, the high energy side doublet for all films shows the binding energy of Ta $4f_{7/2}$ to be 26.2 eV and of Ta $4f_{5/2}$ close to 28.2 eV, close to the chemical state of Ta in Ta_2O_5 (Ta $4f_{7/2}$ = 26.2 eV) (34, 36). Regarding the low energy side doublet, the binding energy of Ta $4f_{7/2}$ is around 23.5 eV and of Ta $4f_{5/2}$ close to 25.5 eV, which correspond to binding states of Ta in Ta–N system ($4f_{7/2}$ = 23 eV and $4f_{5/2}$ = 25 eV [95]. The fraction of Ta_2O_5 binding state is higher for the 3% N_2 as compared to 25% N_2 film, which is evident from the intensity of the high–energy side shoulder in the Ta 4f spectra which increases with decreasing N_2 content. It looks like the incorporation of residual oxygen in crystalline Ta–N is reduced as the N_2 content increases. A similar effect has been reported by Chang *et al.* [96].

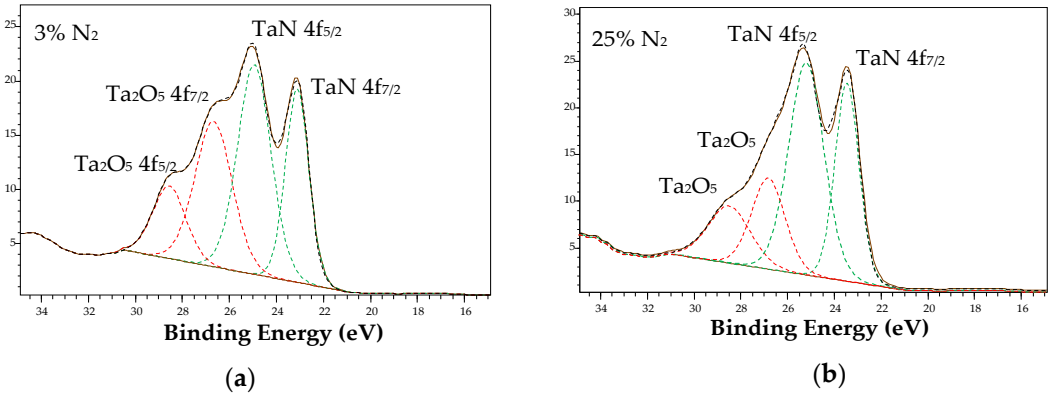

Figure 4-7 Deconvoluted Ta 4f peaks for films deposited with (a) 3% (b) 25% N_2

Figures 4-8(a) and (b) show the deconvolution of the N 1s peak including the Ta $4p_{3/2}$ for the 5% and 25% N_2 film, respectively. As seen in the 25% N_2 film, the N 1s peak is around 397 eV whereas the 5% N_2 peak can be deconvoluted into two peaks with binding energies, 397.2 eV and 398.1 eV. The presence of these two peaks in the low N_2 content films is consistent with the TaN and Ta_2N phases detected by XRD. Thus, the XPS findings are in agreement with XRD data adding additional insight to the gradual nucleation and growth of the Ta_2N phase as the N_2 content decreases.

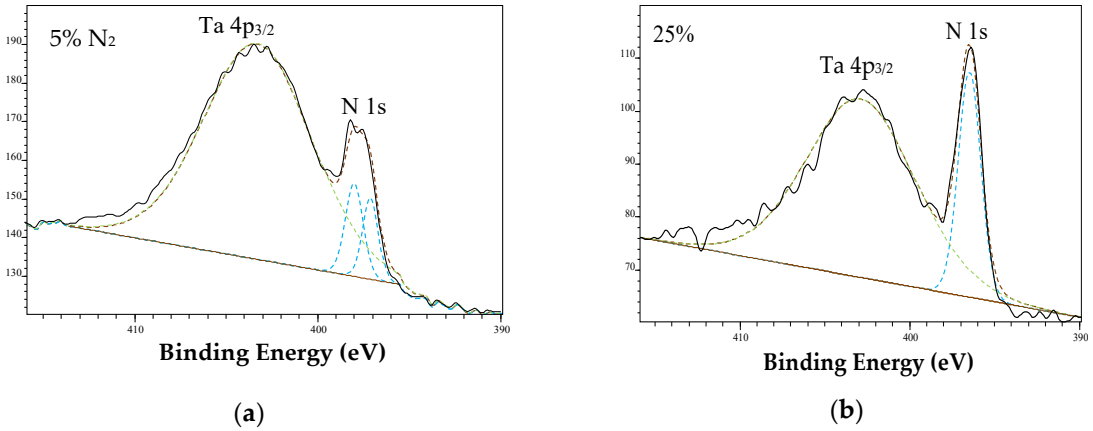

Figure 4-8 Deconvoluted N 1s peak for film deposited with (a) 5% N_2 (b)25% N_2.

4.3.3 Microstructural Investigation

In order to understand the effect of varying N_2 content in the gas mixture on the microstructure of the Ta–N films, three films were selected to be analyzed using TEM. These were the films deposited at E_B = –100 V with 7%, 5% and 3% N_2.

4.3.3.1 Ta–N film Deposited with 7% N_2

Figure 4-9(a) is a bright field TEM image of the bulk structure of the film deposited with 7% N2, showing signs of columnar morphology along the growth direction. Figure 4-9(b) is a cross section bright field TEM image showing the interface between the Si substrate and the Ta–N film. The film shows a sharp interface with the substrate via a Ta adhesion layer, which is ~60 nm thick with a seamless transition to the TaN film. A similar smooth transition was observed for the films with 5% and 3% N_2. The SAED pattern shown as an inset in Figure 9(b) was taken from an area in the film (away from the film/Si interface) and shows a single diffraction ring with lattice spacing 2.5 Å. This can be identified as the (111) plane of fcc TaN. The SAED pattern agrees well with the XRD pattern for this film where a single peak was observed corresponding to fcc TaN as shown in Figure 1. Figure 4-9(c) is a HRTEM image from a cross section of this film which depicts

the presence of 5–15 nm size grains (shown by circles) separated by amorphous boundaries (shown by dotted lines).

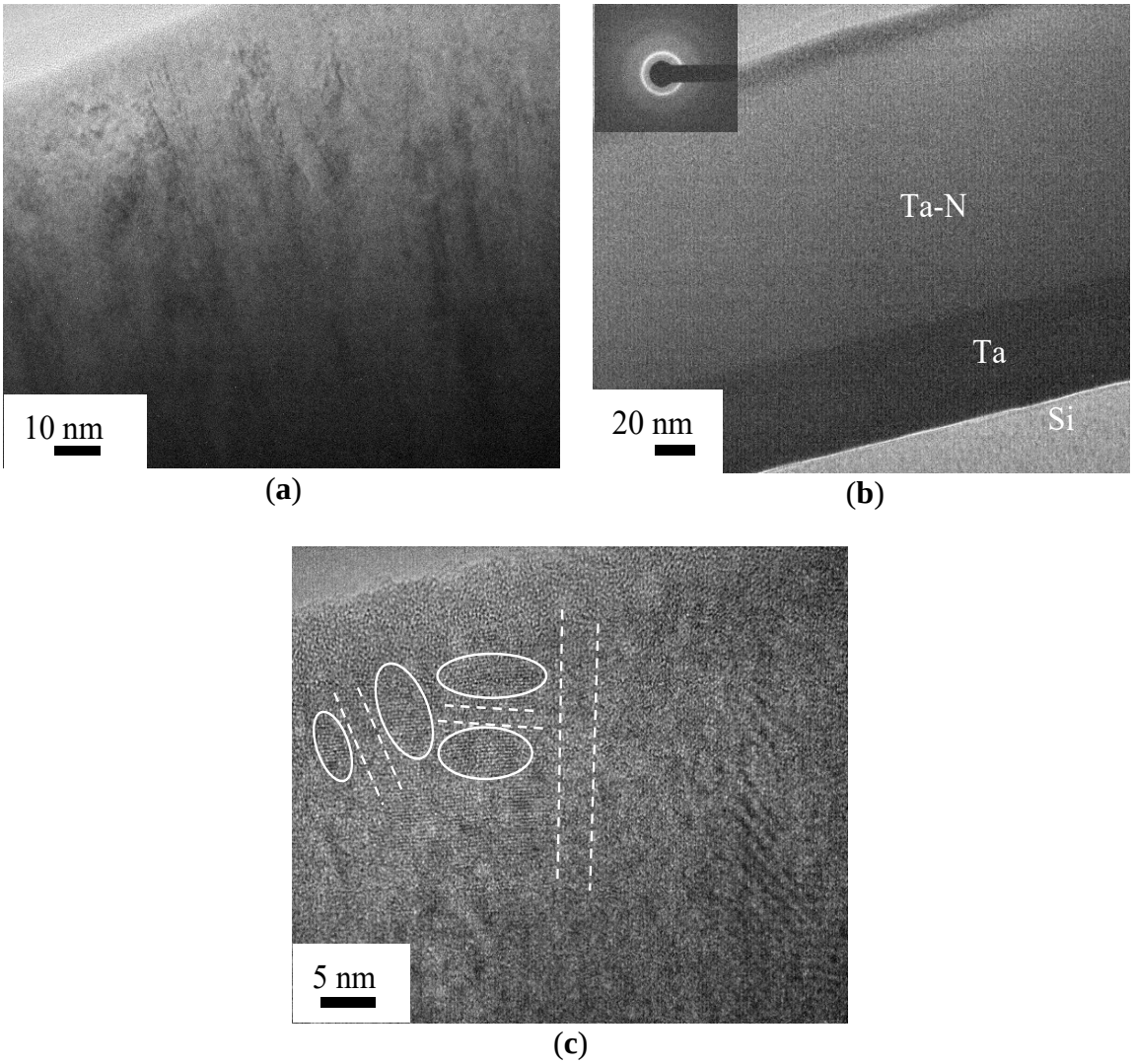

Figure 4-9(a) TEM image, (b) TEM image of film/Si interface (inset is the SAED pattern) and (c) HRTEM image from a cross section of the film sputtered with 7% N_2.

4.3.3.2 Ta–N film Deposited with 5% N_2

Figure 4-10(a) is a bright field TEM image of the film deposited with 5% N_2 showing very fine needle like structures and some rounded structures indicating presence of more than one phase. This agrees well with the XRD pattern (Figure 4-2) which clearly showed a mixture of phases for

this film. Figure 4-10(b) is a typical SAED pattern taken from an area away from the film/Si interface showing several diffractions. The first diffraction ring (1) has a lattice spacing of 2.63 Å and can be identified as the (100) plane of hex Ta_2N. The diffraction spots (2) at the outer diameter of the first ring (1), have a lattice spacing of 2.14 Å and can be identified as the (200) plane of fcc $TaN_{1.13}$.

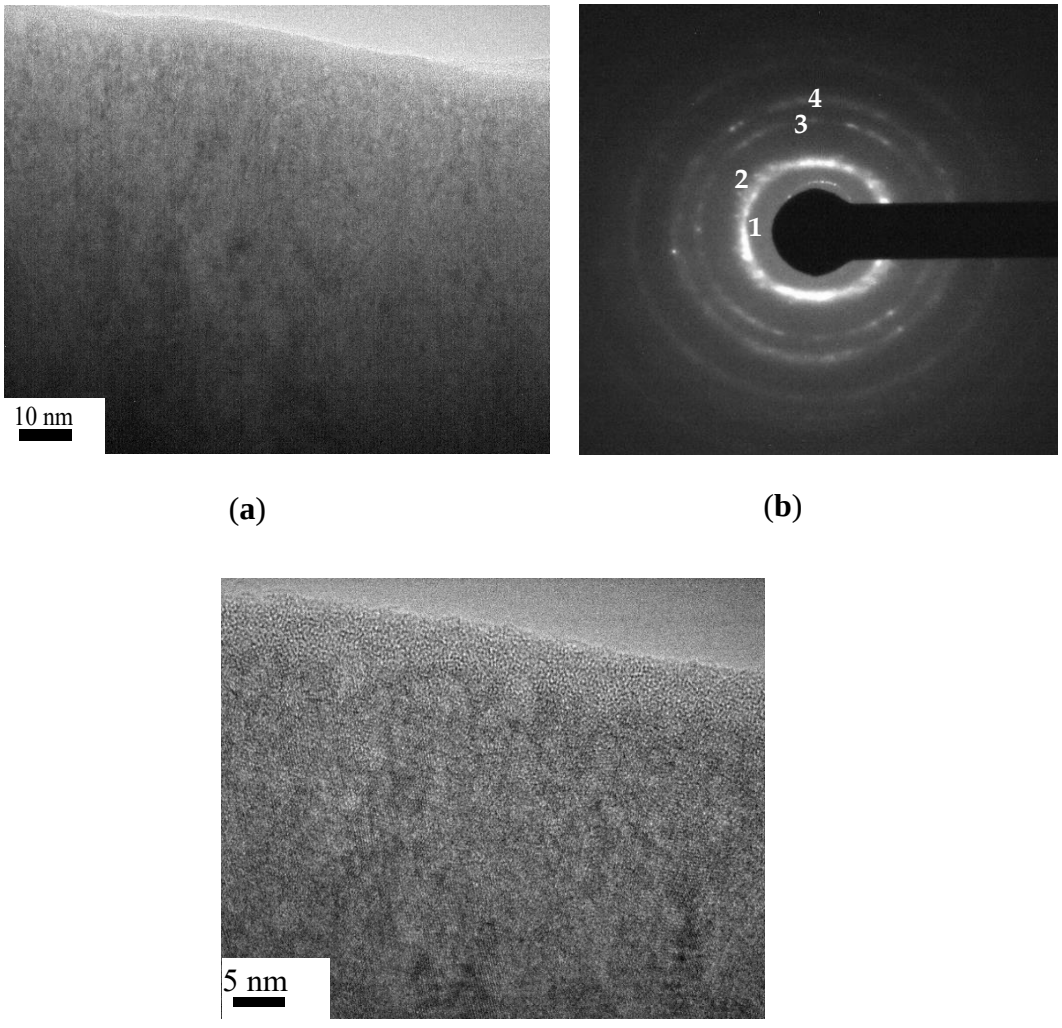

(**a**) (**b**)

(**c**)

Figure 4-10(a) TEM image, (b) SAED pattern and (c) HRTEM image from a cross section TEM foil of a Ta-N film deposited with 5% N_2.

The expected (111) diffraction of fcc $TaN_{1.13}$ and (002), (101) of hex Ta_2N with lattice spacing 2.49 Å, 2.45 Å and 2.32 Å, respectively are present in this diffused diffraction arc but cannot be differentiated. This agrees with the broad transition peak observed in the XRD pattern for this film (Figure 2). The diffraction ring (3) with lattice spacing 1.52 Å can be assigned mainly to the (220) plane of fcc $TaN_{1.13}$ (and also to (110) of hex Ta_2N). The diffraction ring (4) with lattice spacing 1.29 Å can be assigned to the (220) plane of hex TaN. It should be noted that the (220) peak for hex TaN was not visible in the XRD as it shows diffraction at 2θ angle of 72.9° which is beyond 65° of the diffraction pattern. Figure 4-10(c) is a cross section HRTEM image of the film clearly showing randomly oriented elongated and rounded grains depicting more than one morphology. Nanograins with a typical size of 2–5 nm with no visible amorphous boundaries between grains can be observed.

4.3.3.3 Ta–N film Deposited with 3% N_2

Figure 4-11(a) is a cross section bright field TEM image of the film deposited with 3% N_2 showing presence of nano–needle like structures. The nano–needles have a lateral size of ~5–10 nm and a length of ~20–30 nm. Figure 4-11(b) is a typical SAED pattern taken from an area in the film (away from the film/Si interface) showing several diffractions. The four diffraction rings (1), (3), (4), and (5) with lattice spacing 2.63 Å, 2.30 Å, 1.78 Å and 1.5 Å, respectively can be identified as the (100), (101), (102), (110) plane of hex Ta_2N. The diffraction ring (2) with lattice spacing 2.49 Å corresponds to the (111) plane of fcc $TaN_{1.13}$ phase. The presence of this phase could also be seen in the shoulder around 2θ angle of 36° in the XRD pattern for this film (Figure 2). Also, as is evident from the SAED pattern, the diffraction arcs are discontinuous indicating ordering of the columnar grains (in this case nano-needles) in the in-plane direction. This is in addition to the texture in the films developed along the growth direction as detected by XRD, which showed the

(101) plane of the hex Ta_2N, d–spacing 2.30 Å as the high intensity peak. The (002) and (102) diffractions of hex Ta_2N were absent in the XRD pattern for this sample. These observations show that both random and textured regions exist in the film. Figure 4-11(c) is a HRTEM image taken from an area away from the film/substrate interface. The grain size varies from 5–10 nm. Most grains are interconnected with their adjacent grains directly without the presence of amorphous boundaries. Very few amorphous boundaries were formed between the grains.

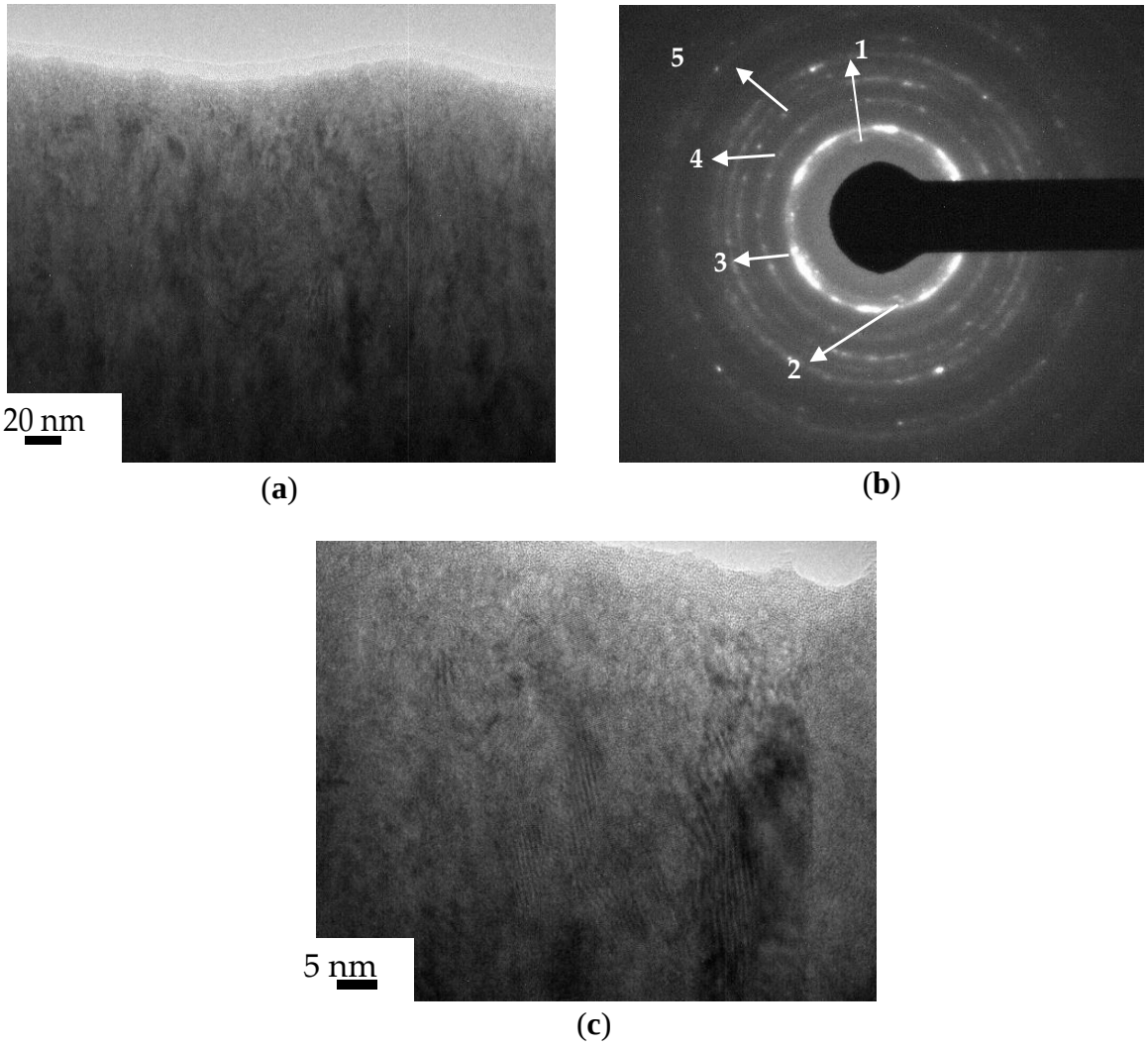

Figure 4-11(a) Bright field TEM image, (b) SAED pattern and (c) HRTEM image from a cross section of a Ta-N film deposited with 3% N_2.

4.3.4 Surface Morphology, Mechanical and Tribological Properties

Figure 4-12 shows the cross-section morphology of the Ta–N film deposited with 3% N_2. The cross section shows a dense film with a sharp interface between the Ta adhesion layer (~40 nm) and the substrate as well as a smooth transition from the adhesion layer to the TaN film. It is also evident that initially a smooth, featureless Ta-N film grows (~180 nm) from the Ta interlayer and subsequently, the film develops a nanocolumnar structure. The surface roughness was measured by optical profilometry and was around 10 nm for all films.

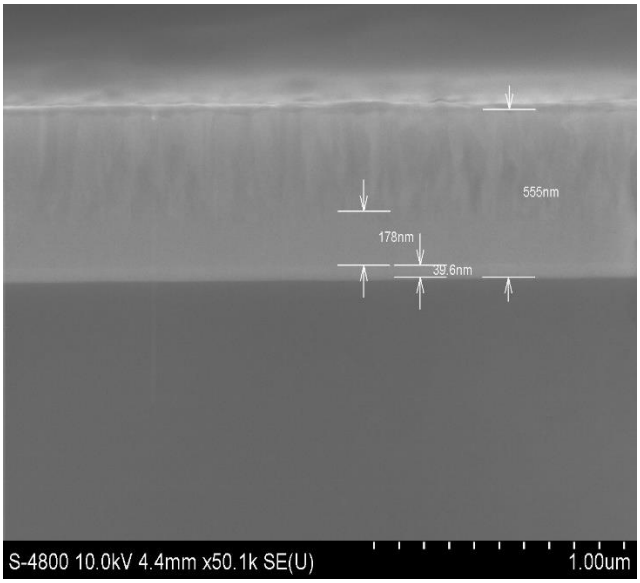

Figure 4-12 Cross section of the Ta–N film deposited with 3% N_2.

Nanoindentation experiments were conducted to study the effect of the varying N_2 content in the gas mixture on the mechanical properties of the films. Figure 4-13(a) shows variation in hardness, effective Young's modulus and residual stress as a function of the N_2 content of films deposited at E_B = –100 V. As the N_2 content is decreased from 25% to 3%, there is an increase in hardness from ~20 GPa to ~33 GPa. However, the 7% N_2 film shows a lower hardness of ~ 24 GPa. This decrease in hardness is possibly due to the texture developed in the film depicting a preferred fcc (111) orientation (Figure 1) as compared to the 10% and 15% N_2 film which have a

more uniform non-textured fcc crystal structure. Hardness value of ~20 GPa for fcc TaN has been previously reported in the literature [69]. As can be seen, the 25% N_2 film also showed preferred fcc (111) orientation and displayed hardness of ~20 GPa. The 7% N_2 film, shows comparable hardness but with larger scatter than the 25% N_2 film. This can be attributed to the nucleation of the higher hardness hex Ta_2N nanograins in the 7% N_2 film (Figure 1). Decreasing the N_2 content to 5% and 3% results in higher hardness around 33 GPa due to change in crystal structure from dominant fcc TaN (25% to 7% N_2) to a mixture of fcc $TaN_{1.13}$ and hex Ta_2N (for 5% N_2) and finally to hex Ta_2N (for 3% N_2). The variation in effective Young's modulus shows a similar trend like the variation in hardness and increases from ~185 GPa to ~230 GPa as we decrease N_2 content from 25% to 3%.

The low residual stress observed for the 5% N_2 film compared to the rest of the films is more likely due to the formation of a mixture of phases in this film. The 3% film exhibited a good combination of hardness (~33 GPa) accompanied with a relatively low residual stress (~ –1.5 GPa). Nano–needle like structures which were observed for this film play a critical role in enhancement of film hardness (Figure 4-11). Nano-needle like structures usually have a single crystal structure and exhibit strong preferred crystallographic orientation. The hardness enhancement due to the presence of nano-needle like structures is very similar to the enhanced enhancement due to nano-columnar morphology where dislocation formation is unlikely when the size of nanocolumns is ~5-10 nm. Even if dislocations did nucleate during indentation, dislocation motion would be impeded due to the transition from one crystallographic orientation to another.

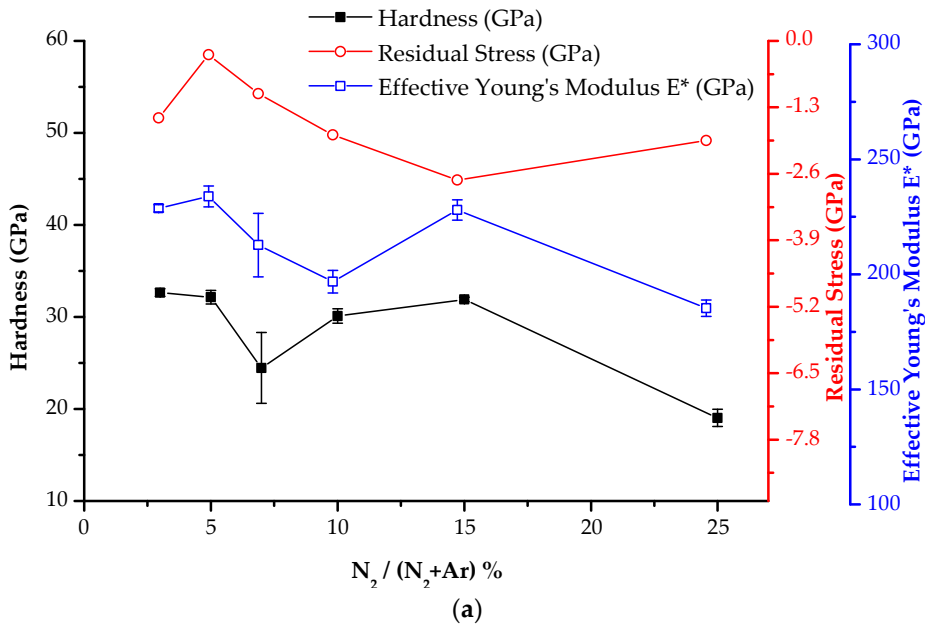

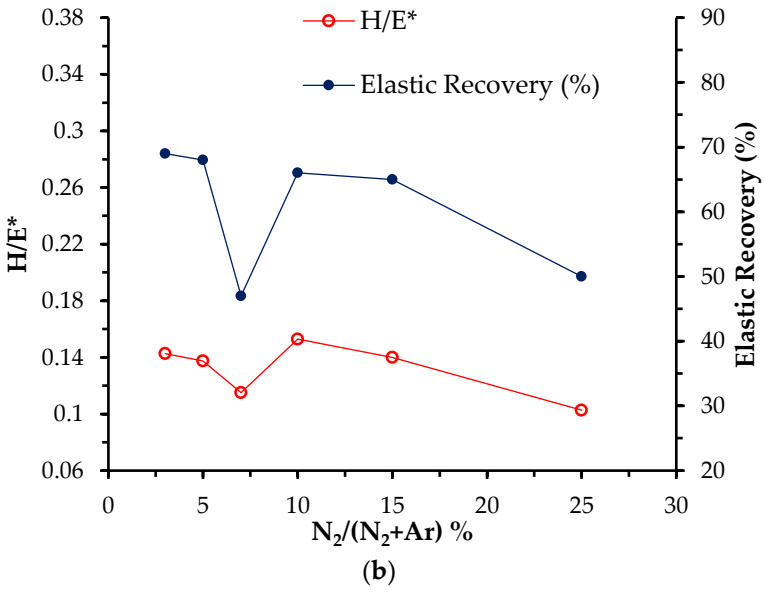

Figure 4-13 Variation in (a) hardness, Elastic Modulus and residual stress (b) H/E* ratio and elastic recovery W_e (%) of the films deposited at E_B: -100 V with N_2 varying from 25% – 3%.

Figure 4-13(b) shows the variation of H/E* ratio and elastic recovery W_e (%) of the films with N_2 varying from 25% – 3%. For films deposited with 25% - 10% N_2, H/E* ratio is around 0.10 and elastic recovery is between 40% - 50 %. The films deposited with 7%, 5% and 3% N_2 have a high H/E* ratio of ~ 0.13 and elastic recovery is ~ 68 %. Hard coatings with high values of H/E* ratio ≥ 0.1 and high W_e (> 70%) exhibit high resistance to plastic deformation and increase the resistance of the coating to cracking. The same H/E* ratio approximately correlates with the same elastic recovery W_e [97, 98].

Figure 4-14 shows the variation of hardness and residual stress of films deposited at E_B = –200 V and varying the N_2 content. Decreasing the N_2 content from 7% to 5% results in the increase in hardness from ~33 GPa to ~37 GPa. This can be attributed to the crystal structure change from fcc TaN to hex Ta_2N.

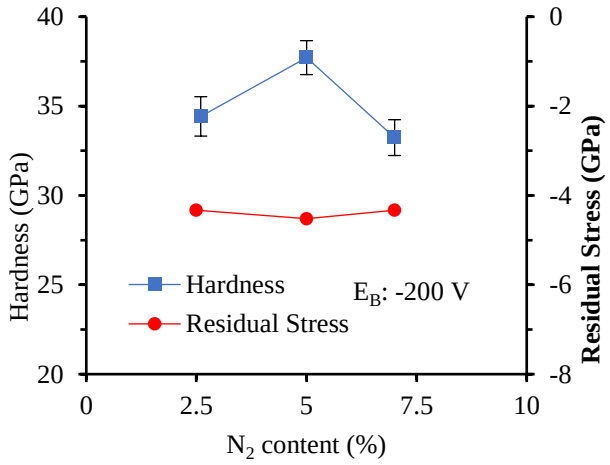

Figure 4-14 Variation of hardness and residual stress of films deposited at EB = –200 V and varying the N_2 content from 7% to 2.5%.

Decrease in N_2 content from 5% to 2.5% results in slight decrease of hardness from ~37 GPa to ~34 GPa. The crystal structure present in both the films is hex Ta_2N, however, the 2.5% film shows significant texture along the (101) plane. This could be one of the possible reasons for the slight

decrease in the hardness of this film. These films were accompanied by high compressive stress of ~ 4 GPa. This could possibly be explained by the higher energy delivered to the films by Ar atoms (due to higher kinetic energy at higher E_B) and possibly also by sputtered Ta atoms.

Pin on disc experiments were performed on Ta–N films which were deposited at a E_B of –100 V with 5% and 3% N_2 content. The coefficient of friction (μ) was continuously measured during the testing for the 3% and 5% N_2 films and was between 0.8 – 0.9 as shown in Figure 4-15(a), (b).

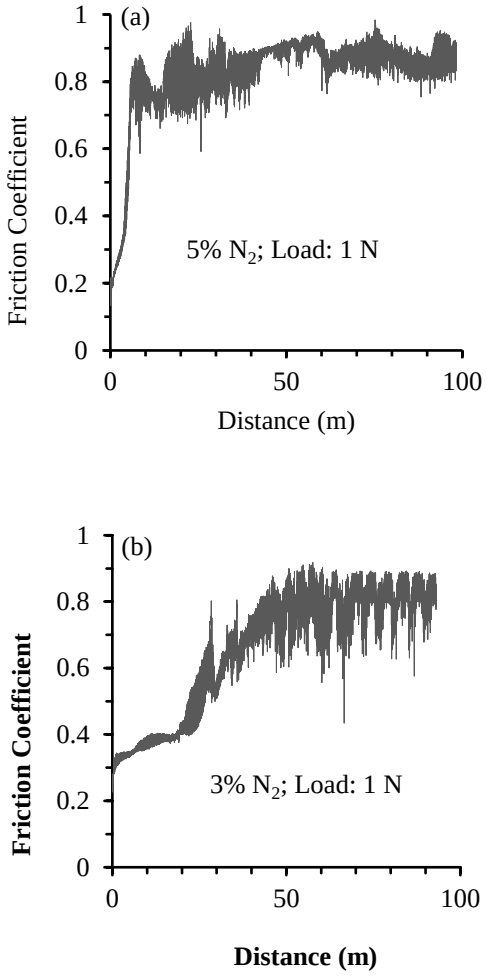

Figure 4-15 Coefficient of friction (μ) of TaN film deposited with (a) 5% and (b) 3% N_2.

Tribological studies reported for some nanocomposite films have drawn some conclusions like hardness is not a sufficient condition to reach low friction. Coefficient of friction(μ) decreases with decreasing value of E* and high value of W_e results in low μ. Similar conclusions were drawn for the wear. The E* and W_e for both the 3% and 5% N_2 films was ~230 GPa and ~68% respectively, and as observed μ was ~0.8 - 0.9 for both these films [98].

Figure 4-16 presents the two-dimensional wear track profiles for the 5% and 3% films. As can be seen, the wear track of the 5% N_2 film is much wider (~220 μm) compared to 3% N_2 film (~40 μm). Similarly, the 3% N_2 film showed a slightly lower wear track depth (~32 μm) compared to 5% N_2 film (~34 μm). Overall, the 3% N_2 film exhibited almost an order of magnitude lower wear rate (3.1×10^{-6} mm^3/Nm) compared to the 5% N_2 film (2.8×10^{-5} mm^3/Nm).

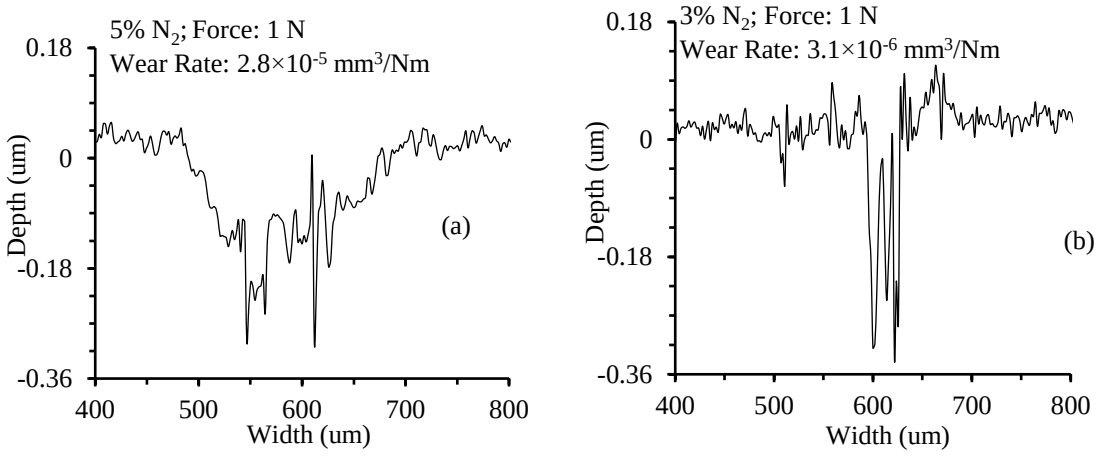

Figure 4-16 Two- dimensional wear track profile for films sputtered with (a) 5% N_2 and (b) 3% N_2 content.

Considering the microstructure of these two films, the higher wear rate of the 5% N_2 film is attributed to the presence of both fcc TaN and hex Ta_2N phases. As noted earlier, the fcc TaN phase has lower hardness (~25 GPa) than that of the hex Ta2N phase (~33 GPa) and thus, it is expected to wear out faster. This can produce a three body wear at the contact resulting in the faster

wear rate of the 5% N_2 film. On the contrary, the 3% N_2 film has a uniform microstructure composed of a hard hex Ta_2N phase present as fine nano needles and a grain size of 5-10 nm, Figure 4-11. This film exhibited a very low wear rate and can be a potential coating material for tribological applications.

4.3.5 Oxidation Resistance

Two films were chosen to test the oxidation resistance of the TaN films, the ones deposited with 3%, 5% and 7% N_2 / (N_2 + Ar) gas ratio. Thermogravimetric analysis (TGA) was carried out to observe their oxidation behavior. Amount of weight change of a material was measured as a function of increasing temperature in air.

The thermogravimetric curve displaying the oxidation resistance behavior of the 7% N_2 film is shown in Figure 4-17, depicting an increase of the film mass Δm with increasing annealing temperature, T. The film was dynamically heated up to 1300 ^oC in air, with a heating rate of 10 ^oC min^{-1} and subsequently cooled down to room temperature.

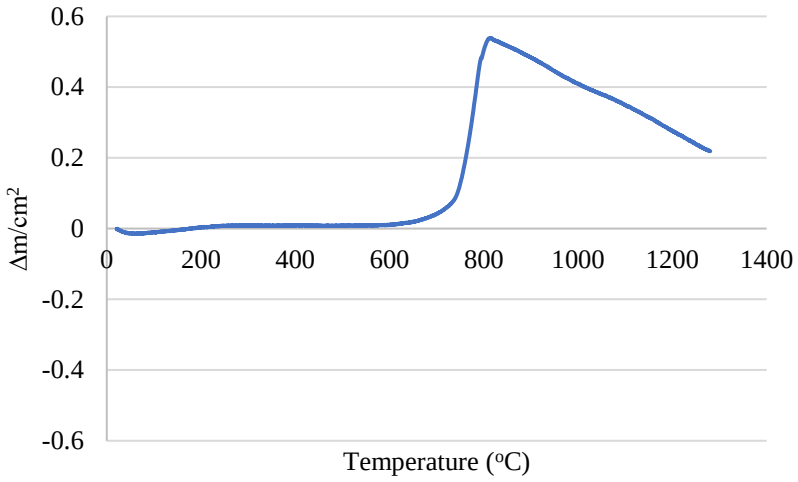

Figure 4-17 TGA curve for Ta-N film deposited with 7% N_2.

The results show a satisfactory oxidation behavior of the TaN film. The film remains completely stable upto 750 ^oC and the oxidation rate starts to increase at 780 ^oC, which depicts the

possible formation of Tantalum oxide. The mass gain Δm increases up to temperature 820 ^{o}C and then there is mass loss. The mass loss of the film is probably due to out diffusion of Nitrogen or disintegration of the film. During the decomposition of MeN (metal nitride) the metal gets oxidized and nitrogen is released from the coating. Similar behavior was shown by films deposited with 3% and 5% N_2/ (N_2 + Ar) gas ratio.

4.3.6 Summary of the Effect of Varying N_2/ (N_2 + Ar) Gas Ratio on Mechanical Properties in Magnetron Sputtered TaN Films

In this study, the effect of the varying N_2 content in the gas mixture on the crystal structure, composition, chemical states, microstructure and eventually mechanical properties of Ta–N thin films was studied. Varying N_2 percentage in the gas mixture was shown to have a significant effect on material structure and properties. Ta–N films deposited with 25% - 7% N_2 are dominated by fcc TaN phase with hardness varying from 22 - 26 GPa and compressive stress varying from 1.84 - 2.72 GPa. The 7% film exhibited a nano columnar morphology and was accompanied by high H/E* ratio of 0.13 and low compressive stress of 1.03 GPa. Further decrease of N_2 to 5% resulted in a mixture of fcc $TaN_{1.13}$ and hex Ta_2N phases and was composed of randomly oriented nanocrystals with a typical grain size of 2 – 5 nm. This led to increase in hardness of ~32 GPa and was accompanied by high H/E* ratio of 0.13 and low compressive stress of 0.27 GPa. The film with 3% N_2 was dominated by hex Ta_2N crystal structure. This film was composed of nano–needle like structure and grain size varied from ~ 5 – 10 nm. The hardness for this film was a maximum of ~33 GPa with low compressive stress of 1.51 GPa. XPS investigation indicated Ta–N and Ta-O chemical states for all films. However, for the film deposited with 3% N_2, the fraction of Ta_2O_5 chemical state was higher than the rest of films, indicating incorporation of residual O_2 with decrease in N_2 content. It is observed that decreasing the N_2 content in the gas mixture results in

refining the microstructure and significantly increasing the hardness of the reactively sputtered Ta-N thin films, while the oxidation resistance for all the three TaN films with 7%, 5% and 3% N_2/ (N_2 + Ar) ratio seems to be almost same and is around 750 ^oC.

4.4 Effect of Varying Substrate Bias (E_B) on Film Properties

By varying the bias voltage applied to the substrate during the deposition of TaN films, the relationship between bias voltage applied at the substrate and film properties were explored. During bias sputter deposition, where deposition and sputtering of the wafer are done simultaneously as energetic ions bombard the film surface and this results in refining the grain size and altering the film properties. A negative bias relative to the plasma is applied to the substrate, which is electrically isolated from the chamber walls. Positive Ar atoms from the plasma will now be accelerated to the wafers to the substrate and sputter off atoms. The energy of the ions can be controlled by controlling the substrate bias.

In sputter cleaning, no deposition can occur on the wafer surface by usually using a shutter to block sputtered material from the target. A controlled thickness of the material is sputtered off the wafer, removing any contaminants and oxides. In bias sputtering, conditions are chosen so that more deposition occurs than sputtering. A more planarized film is obtained because of bias sputtering. The drawback of this method is that the net deposition rate is slow. The relationship between bias voltage and deposition rate was not of key importance in this work, the interest instead resided in the relationship between processing conditions, mechanical properties, and film microstructure, the relationship between bias and deposition rate was explored to gain clearer understanding of the coating deposition process.

To determine the effect of changing substrate bias on TaN film properties, all the films were deposited at a temperature of 550 ^{o}C, with 50 W power to Ta target, at 5% N_2/ (N_2 + Ar) ratio and the substrate bias was increased from -50 V to -200 V.

4.4.1 XRD Analysis

Figure 4-18 shows the low–angle XRD of the Ta–N films deposited with 5% N_2 content and E_B varying from -50 V to -200 V. The XRD spectra of the film deposited at -50 V substrate bias shows a diffraction peak at 2θ angle of 36.02^{o} corresponding to lattice spacing of 2.49 Å. This can be identified as the (111) plane of fcc $TaN_{1.13}$. This film seems to show a noticeable texture. Increasing the E_B to -200 V results in diffraction peaks at 2θ angles of 33.8^{o}, 38.4^{o}, and 60.4^{o} with lattice spacing 2.63 Å, 2.32 Å and 1.53 Å, respectively. These can be identified as the (100), (101), (110) planes of hex Ta_2N (PDF#26-0985). It should be noted that the (002) reflection of the hex–Ta_2N is expected to be present in the shoulder around 2θ angle of 36.5^{o}. All the reflections are at lesser 2θ values as the films are under compressive stress.

The XRD of the film deposited with E_B = -100 V shows at least two peaks at 2θ angle of 33.9^{o} and 60.40^{o}, and a broad peak around 36.02^{o} which in turn is comprised of many peaks. The peaks at 33.9^{o}, 36.02^{o}, 60.40^{o} with lattice spacing 2.63 Å, 2.49 Å and 1.53 Å, respectively can be identified as the (100) plane of the hex Ta_2N, and (111) and (220) plane of fcc $TaN_{1.13}$, respectively. Thus, the XRD spectrum for the film deposited at E_B = -100 V shows a mixture of phases and is a transition from a single phase fcc $TaN_{1.13}$ (E_B = -50 V) to mainly hex Ta_2N (E_B = -100 V). We should note that since the film deposited at E_B = -100 V had a mixture of phases, the other expected planes such as (002), (101) of the hex Ta_2N and (200) of the fcc $TaN_{1.13}$ phase are present in the broad shoulder extending from a 2θ angle of 35.83^{o} to about 42^{o} as shown in Figure 2. The hex Ta_2N

phase which dominates in the film deposited with E_B = -200 V was still emerging in the film deposited with E_B = -100 V.

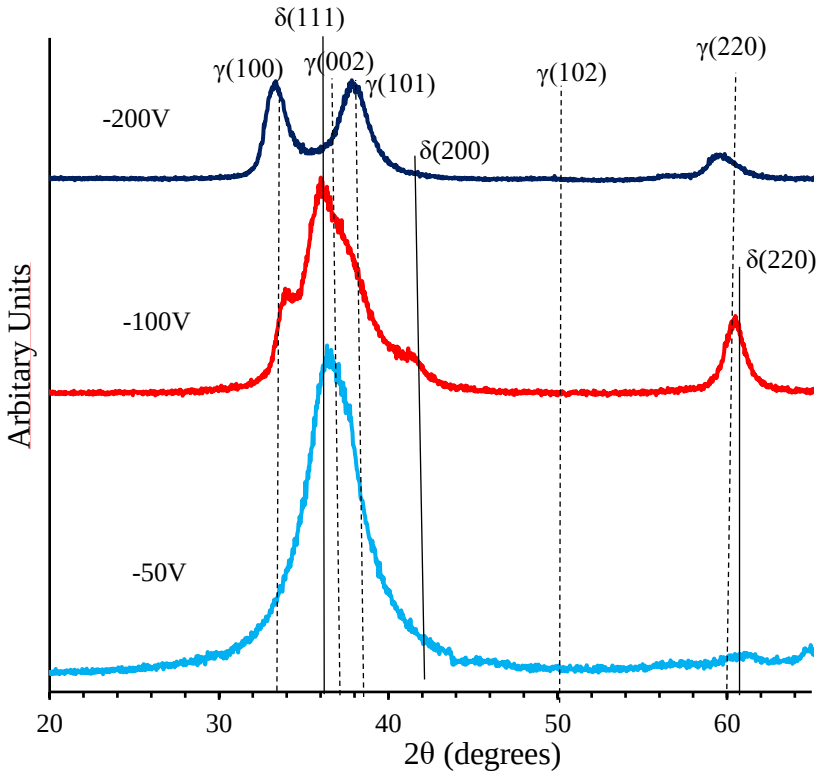

Figure 4-18 Low–angle XRD of films deposited with varying substrate bias.

Energetic ions bombard the film during bias sputtering. As a result, the films are re-sputtered throughout the deposition process, making the films more planarized, which results in significantly decreasing the deposition rate. In addition to that, bias sputtering refines the microstructure and decreases the surface roughness of the films deposited using PVD. Figure 4-19 shows the decrease in deposition rate with increase in substrate bias.

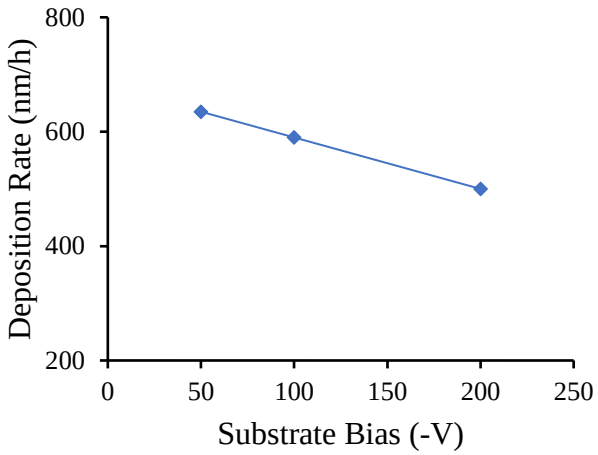

Figure 4-19 Variation in deposition rate of the films deposited with varying substrate bias.

4.4.2 XPS Studies

The chemical binding states of Ta in the Ta–N films were examined by XPS; the narrow scan Ta-4f and N 1s spectra are shown in Figure 4-20(a) and (b), respectively. All binding energy values have been corrected for the charging effect with reference to the adventitious carbon 1s peak at 284.6 eV. For XPS measurements, sputter cleaning was also performed to remove surface contamination. Sputter cleaning may cause phase changes resulting in the shift of XPS peak positions. However, there are well separated deconvoluted peaks and the peak positions are in good agreement with the reference data. Therefore, the shift of XPS peaks due to sputter cleaning is insignificant. As shown in figure 4-20(a), the Ta $4f_{7/2}$ peak for film deposited at -200V bias has shifted far from 21.8 eV for pure Ta. The N 1s peak is in well agreement with data, which reports the binding state of N 1s in metal Nitrides as 397 eV. Figures 4-21(a) and (b) show the deconvoluted peaks for films deposited at -50 V and -100 V bias. After deconvolution, the spectra for these films are composed of two sets of Ta 4f doublets. Considering, the split energy by spin orbit coupling of $4f_{7/2}$ and $4f_{5/2}$ in Ta 4f as 1.9 eV, the high energy side doublet for all films shows the binding energy of Ta $4f_{7/2}$ to be 26.2 eV and of Ta $4f_{5/2}$ close to 28.2 eV, close to the chemical

state of Ta in Ta_2O_5 (Ta $4f_{7/2}$ = 26.2 eV [99]. As far as the low energy side doublet for -100V bias, the binding energy of Ta $4f_{7/2}$ is around 23.5 eV and of Ta $4f_{5/2}$ close to 25.5 eV, which correspond to binding states of Ta in Ta-N system (Ta_2N hex or TaN fcc, which cannot be distinguished) ($4f_{7/2}$ = 23.3 eV and $4f_{5/2}$ = 25.2 eV.

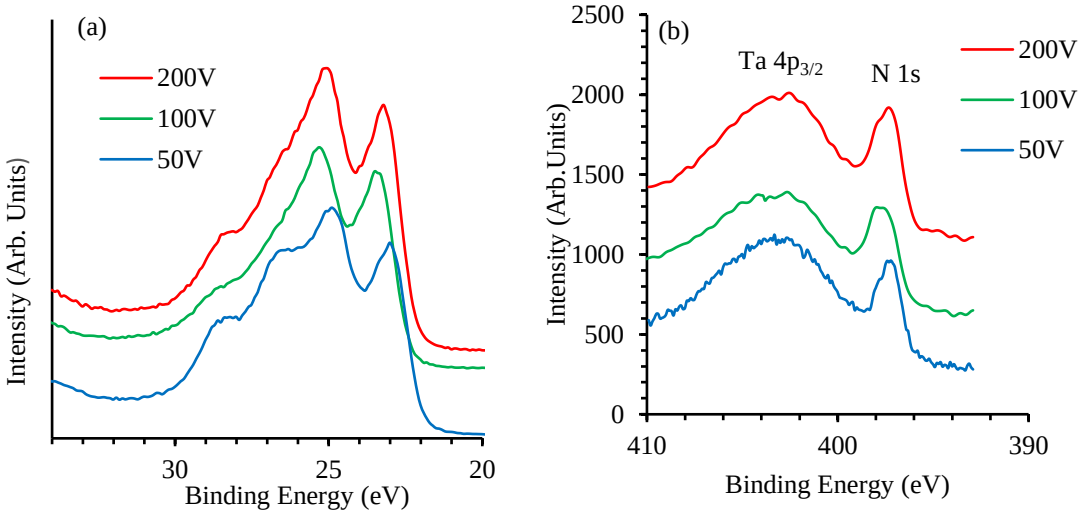

Figure 4-20 Narrow scan XPS spectra of (a) Ta $4f_{7/2}$ core levels (b) N1s core levels.

Higher binding energies also justify the increase in hardness of the Ta-N films. However, for -50 V bias, the binding energy of Ta $4f_{7/2}$ has shifted to 22.9 eV. We can say that this film has binding state between pure Ta and Ta-N binding state. Comparing the spectra for films deposited at -50V and -100V bias the fraction of Ta_2O_5 binding state is higher for film deposited at -50 V bias, as we can see from the intensity of the high-energy side shoulder in the Ta 4f spectra which increases with decreasing bias. It looks like the incorporation of residual oxygen in crystalline Ta-N is increased with decreasing bias.

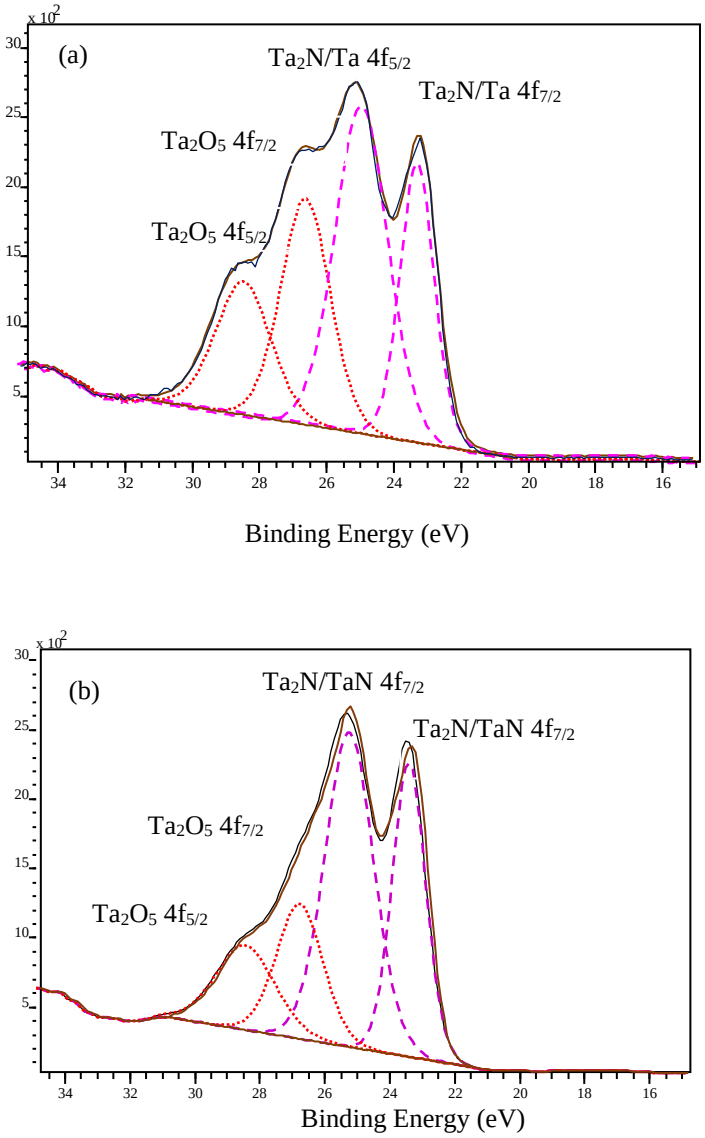

Figure 4-21 Typical deconvoluted XPS spectra of Ta 4f core levels for film deposited with (a) -50 V bias (b) -100 V bias.

4.4.3 Film Hardness and Residual Stress

Nanoindentation was performed on these coatings and the average hardness was obtained from 9 indentation points. Figure 4-22(a) shows the variation in hardness of the films with varying substrate bias. As previously mentioned, upon increasing the substrate bias, the

crystal structure changed from dominant fcc $TaN_{1.13}$ to a mixture of fcc $TaN_{1.13}$ and hex Ta_2N and entirely to hexagonal Ta_2N. The hardness of the film increased to 37.83 GPa in the film deposited at a substrate bias of -200 V from ~33 GPa for the film deposited at -100 V bias. This increase in hardness of the film deposited at -200 V from the film deposited at -100 V could be attributed to the change in crystal structure. Also, it is well known that higher substrate bias leads to refinement of microstructure, which could be another probable reason for increase in hardness.

Figure 4-22(a) shows the change in residual stress with varying substrate bias. The radius of curvature was calculated on uncoated Si wafers before film deposition and on the coatings after deposition. With the presence of residual stress within the TaN films, some curvature will be induced onto the Si wafer. The difference in the curvature of the wafer before and after TaN film deposition, was used to calculate the stresses present within each film using Stoney's Equation, previously described in Chapter 3. Compressive intrinsic stresses in nitride films can be controlled through energetic particle bombardment during growth which creates lattice defects of larger effective molar volume than that of the host lattice. For magnetron sputtering, the energetic particles generated from the sputtering gas are back-scattered inert gas neutrals or ions of Ar or the reactive gas (i.e., Ar and N_2) accelerated by a negative substrate bias potential towards the growing film. The residual stress is very similar for substrate bias -50 V and -100 V, and then increases with increase in substrate bias to ~ 4 GPa for the film deposited at -200 V bias. We can say that hardness for the -100 V and -200 V films was close, and the higher compressive stress induced in the -200 V bias film could have attributed to its increased hardness. Residual stress is affected by stoichiometry, phase, film thickness and deposition conditions. The increase in residual stress with bias can be explained by the fact that with increase in substrate bias, the film deposition rate decreased. The decrease in thickness with increase in substrate bias could be a reason for

increased residual stress. The additional energy due to high bias, favors a particular orientation of atoms that would not be normally possible. This translates into residual stress and curvature is induced in the films after deposition. Figure 4-22(b) shows elastic recovery and H/E* ratio for all films. Elastic recovery is higher in the -100 V bias sample (~ 60%) as compared to the -200 V and -50 V bias films were elastic recovery is ~50%. H/E* ratio for all films is > 0.1.

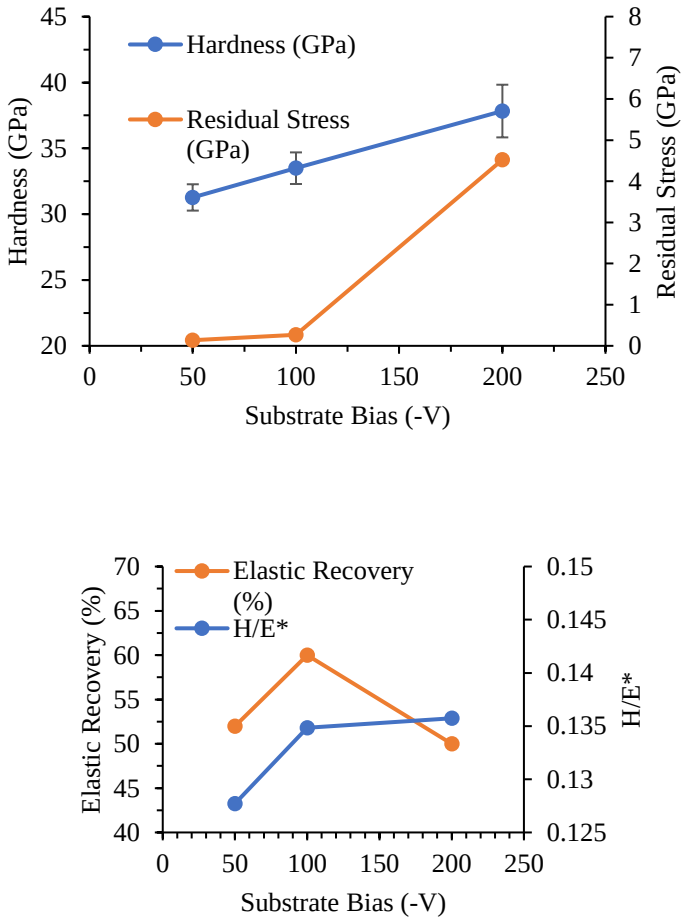

Figure 4-22 Variation in (a) hardness and residual stress (b) elastic recovery (%) and H/E* ratio for films deposited with varying substrate bias (-V).

Figure 4-23 shows a typical example of a nano-indentation loading and unloading curve for a depth-controlled indentation test. Coatings with high elastic recovery (>70%) and greater H/E* ratio (> 0.1) are of key importance for developing hard coatings with enhanced toughness.

Overall, it seems, film deposited with substrate bias of -100 V displays desirable mechanical properties, i.e., high resistance to deformation and resistance to cracking and low residual stresses.

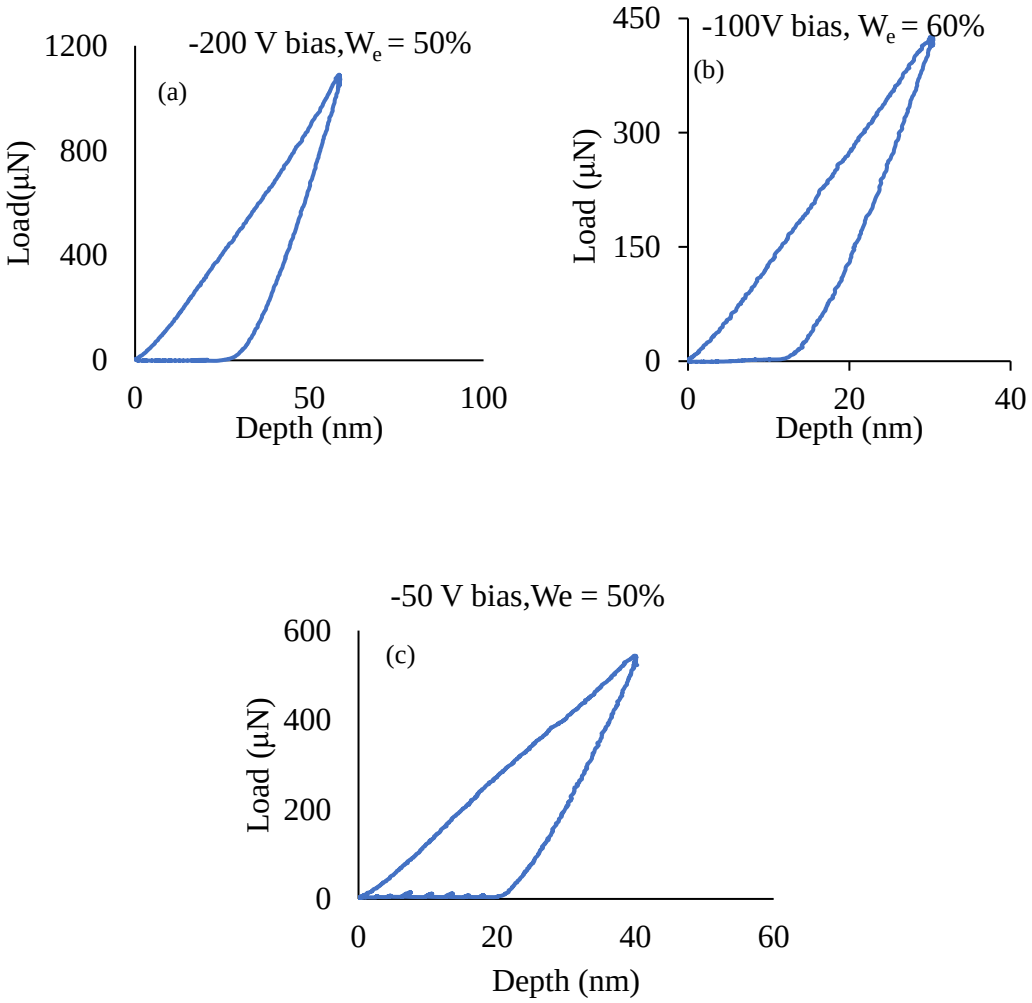

Figure 4-23 Nano-indentation loading and unloading curve for films deposited with E_B of (a) -200 V, (b) -100 V, (c) -50 V.

4.4.4 Summary of Effect of Varying Bias Voltage on Mechanical Properties in Magnetron Sputtered Ta-N Films

In this study, the effect of varying the substrate bias on the crystal structure, chemical states, and mechanical properties of Ta–N thin films was studied. A series of Ta-N films were deposited

with varying substrate bias from -50 V to -200 V. Varying substrate bias was shown to have a significant effect on material structure and properties. As the substrate bias was increased from – 50 V to -200 V the crystal structure changed from a mixture of fcc TaN and fcc $TaN_{1.13}$ (at -50 V) to a mixture of fcc $TaN_{1.13}$ and hex Ta_2N (-100 V) and then entirely to hex Ta_2N (at -200 V). The film deposited with -100 V substrate bias displayed high hardness of ~ 33 GPa and very low residual hardness of 0.5 GPa, while the film deposited at -200 V substrate bias displayed a high hardness of ~ 37 GPa but was accompanied by a high residual stress of – 4 GPa. Residual stress is likely more prominent in the higher bias coatings due to the high amount of energy present at the substrate encouraging specific atomic interactions. After the deposition is completed and the bias is no longer present, the atomic structures which were made possible by the excess energy presence at the substrate cause the presence of increased residual stress. As these coatings are indented, some of the residual stresses imposed by the high bias deposition conditions could be relieved. This would contribute a higher percentage of permanent, plastic deformation and less overall elastic recovery during the unloading of these coatings. As was seen, the higher bias film (-200 V) also showed less elastic recovery of ~50 %.

There seems to be a high degree of inter-relation between mechanical properties and the varying substrate bias voltages for the films. Higher bias film did display impressive hardness values and very less residual oxygen incorporation but was unaccompanied by other undesirable properties such as high residual stress and lower elastic recovery. The film deposited with -100 V bias had a mixture of phases, impressive hardness of ~33 GPa, low residual stress of ~0.2 GPa, good oxidation resistance, elastic recovery of ~60%, $H/E^*>0.1$. In general, it was found across these series lower bias voltage (-100 V) during coating deposition yielded films with better desirable properties.

4.5 Effect of Deposition Temperature on Film Properties

After determining the effect of varying substrate bias and varying N_2/ (N_2+ Ar) gas ratio on the films, TaN films deposited at a substrate bias of -100 V and -200 V, both with 5% N_2 and temperature 550 ^oC, were deposited at 350 ^oC to determine the effect of temperature on the mechanical properties of the films. The other deposition parameters like power to Ta target, percentage of N_2 same, working pressure, substrate rotation was kept the same.

4.5.1 XRD Analysis

Figure 4-24, shows low angle XRD of films deposited with 5% N_2 and a substrate bias of -100 V at varying temperature of 550 ^oC and 350 ^oC. The XRD of the film deposited with 5% N_2 and 550 ^oC shows at least two peaks at 2θ angle of 33.9^o and 60.40^o, and a broad peak around 36.02^o which in turn is comprised of many peaks. The peaks at 33.9^o, 36.02^o, 60.40^o with lattice spacing 2.63 Å, 2.49 Å and 1.53 Å, respectively can be identified as the (100) plane of the hex Ta_2N, and (111) and (220) plane of fcc $TaN_{1.13}$, respectively. Thus, the XRD spectrum for the film with 5% N_2 shows a mixture of phases and is a transition from a single phase fcc TaN (from 25% – 7% N_2) to mainly hex Ta_2N (3% N_2). This film was discussed in detail in the first section of this chapter.

The XRD (Figure 4-24) of the film deposited with 5% N_2 and 350 ^oC shows one broad peak at 2θ angle of 36.83^o d-spacing 2.4, which can be identified as (002) diffraction of hex Ta_2N. This broad peak includes diffractions from other expected planes of hex Ta_2N and fcc TaN and fcc $TaN_{1.13}$, but the energy of the system seems not enough to promote the complete transformation. It is very likely that there would be unreacted Ta in this film. When the temperature is increased to 550 ^oC, the other phases which were likely forming in the low temperature sample as indicated

by one broad peak, completely emerge, as is evident from the differentiated small peaks in the broad peak for the higher temperature sample.

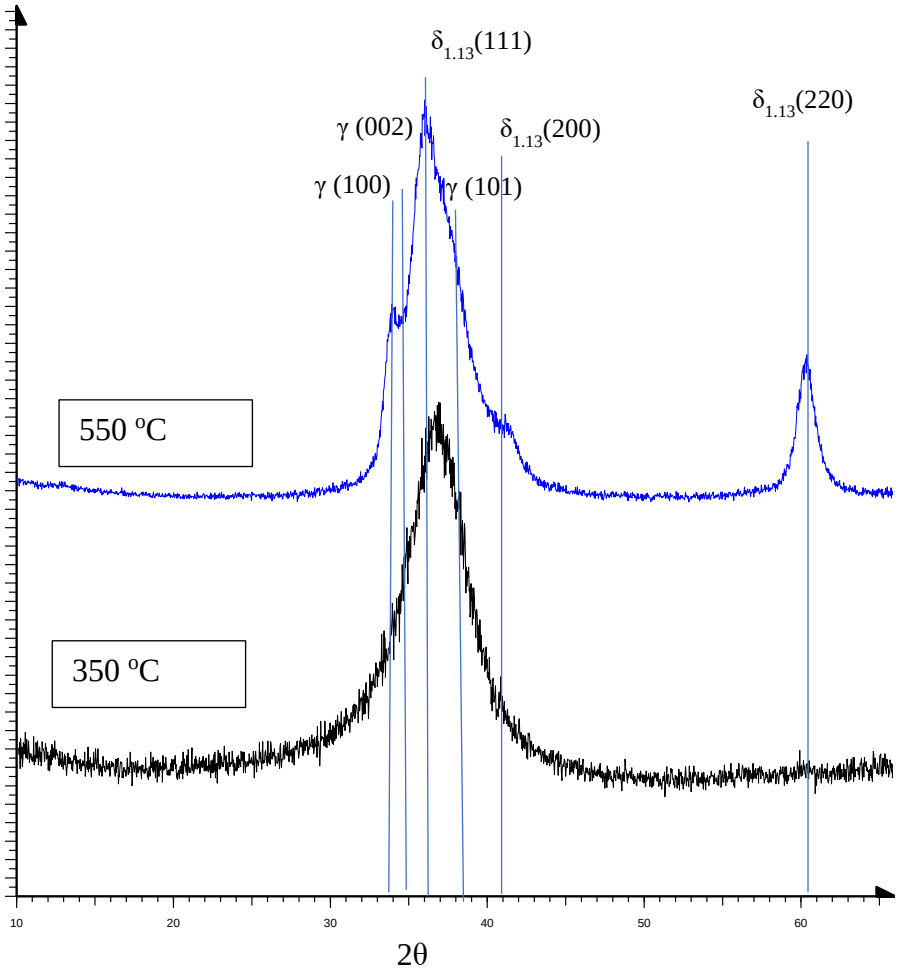

Figure 4-24 Low Angle XRD scans of TaN films deposited at a substrate bias of -100V and deposition temperatures 350 ºC and 550 ºC.

The same trend was observed at a substrate bias of -200 V. Figure 4-25 shows low angle XRD of films S200N5, which were deposited with 5% N_2 and a substrate bias of -200 V, with temperature 350 ºC and 550 ºC. The XRD of the film deposited at -200 V substrate bias and temperature 350 ºC shows a broad peak around 2-theta of 36º and d-spacing 2.49 Å. This peak can

be identified as (111) diffraction of fcc $TaN_{1.13}$. There is one small peak in this broad peak at 2θ angle of 33.9° which suggests presence of other phases as well.

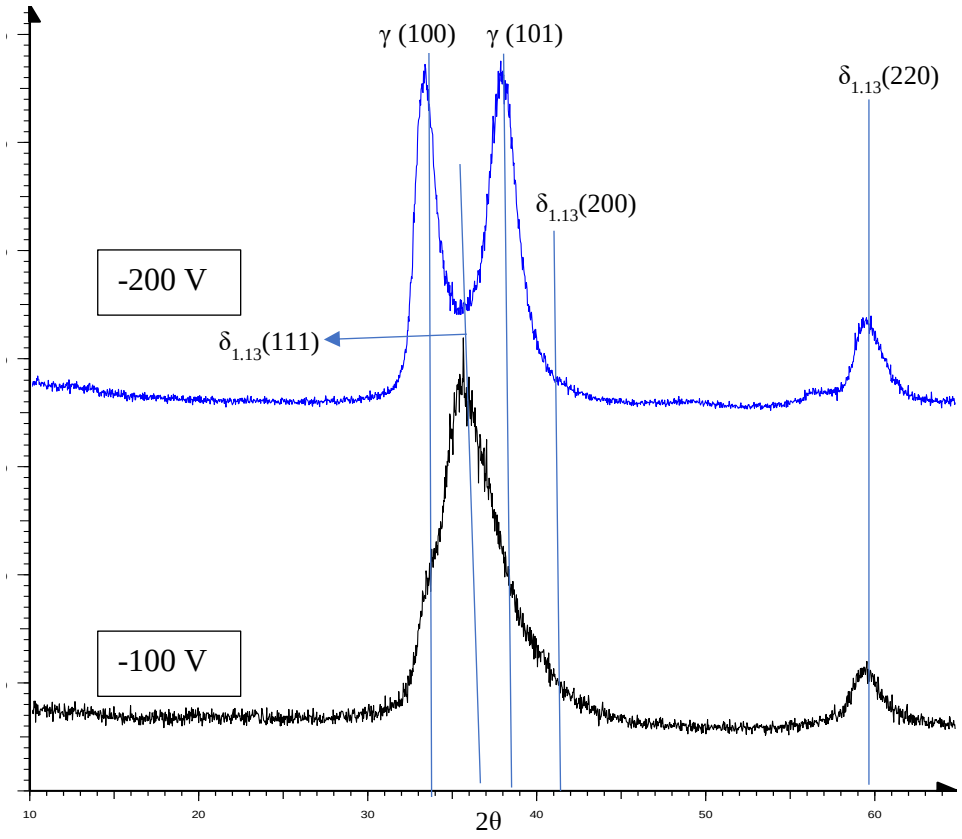

Figure 4-25 Low Angle XRD scans of TaN films deposited at a substrate bias of -200V and deposition temperatures 350 °C and 550 °C.

The peak at 33.9° with lattice spacing 2.63 Å can be identified as the (100) plane of the hex Ta_2N. The peak at 60.40° and d-spacing 1.53 Å can be identified as (220) plane of fcc $TaN_{1.13}$. The other expected diffractions of hex Ta_2N and fcc $TaN_{1.13}$ are present in the broad shoulder extending from 2-theta 36° to 41°. The crystal structure of this film is very similar to the film which was deposited at -100 V bias and 550 °C. It seems like, although this film was deposited at a lower temperature (-200 V and 350 °C), the energy for the transformation (small peaks in addition to the broad peak) was provided by the higher bias as compared to the film which was deposited at the same temperature but lower bias (-100 V and 350 °C, Figure 4-24). The peaks present in the film

deposited at 350 ºC around 2-theta equal to 33.35º and 37.99º have clearly emerged and are distinct in the film deposited at -200 V and 550 ºC. These diffraction peaks at 2θ angles of 33.35º and 37.99 with lattice spacing 2.6 Å and 2.3 Å respectively can be identified as the (100) and (101) planes of hex Ta_2N (PDF#26-0985). It should be noted that the (002) reflection of the hex–Ta_2N is expected to be present in the shoulder around 2θ angle of 36.5º. The diffractions here are at lesser 2-theta values and this is due to the compressive residual stresses in the film. The films were deposited at high substrate bias of -200 V and this led to high residual stresses in these films. Effects of higher substrate bias on the film properties (including residual stress) have been discussed in the previous section.

Figure 4-26 shows the effect of temperature on the deposition rate of the films. It is observed that with decrease in temperature, the deposition rate increases, which suggests that at low temperature bombardment of ions is less as the energy of the system is less. For the -100 V bias sample, the rate decreases from ~660 nm/h to ~590 nm/h as temperature is increased from 350 ºC to 550 ºC. Same trend is observed with the -200 V bias sample, where rate decreases from 550 nm/h to 500 nm/h as temperature is increased from 350 ºC to 550 ºC. Decreased temperature plays the same role as decreased substrate bias as far as film thickness is concerned. With increase in temperature, ions are more energetic and bombard the surface of the substrate, resulting in re-sputtering of films throughout the deposition process, making the films more planarized, which results in significantly decreasing the deposition rate. The films deposited at higher bias have lesser deposition rate as compared to lower bias samples. This has been discussed in detail in the previous section.

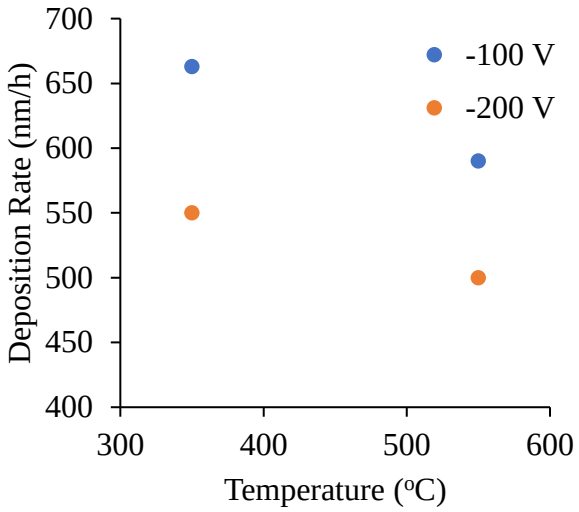

Figure 4-26 Variation in deposition rate (nm/hr) of TaN films with varying deposition temperature.

4.5.2 Film Hardness and Residual Stress

Figure 4-27 shows the variation in hardness of the films with varying temperature. It is observed that in both cases, -100 V and -200 V, the hardness of the films decreases. For the film deposited at -100 V bias, the hardness decreases from ~33 GPa to ~24 GPa, as temperature decreases from 550 °C to 350 °C. As mentioned in the previous section, low temperature (around 350 °C) possibly does not provide the energy for the optimal reaction between Ta and Nitrogen, and thus does not lead to the complete formation of various Ta-N phases. Thus, hardness of Ta-N films decreases with decrease in temperature. The film deposited at 550 °C had a mixture of fcc $TaN_{1.13}$ and hex Ta_2N phases, resulting in high hardness. Also, the TEM investigation for this film revealed randomly oriented elongated and rounded grains depicting more than one morphology. Nanograins with a typical size of 2–5 nm with no visible amorphous boundaries between grains can be observed (refer to section 4.2). This microstructure also explains high hardness for this film.

For the film deposited at -200 V bias, the hardness decreases from ~37 GPa to ~33 GPa, as temperature decreases from 550 °C to 350 °C. In this case, the higher hardness of film deposited

at lower temperature (350 ^{o}C), is higher than the film deposited at -100 V bias and same temperature. This is because better reaction between Ta and N is facilitated by the energy provided by high substrate bias, resulting in the formation of mixture of fcc $TaN_{1.13}$ and hex Ta_2N crystal phases and hence high hardness. The film deposited at -200 V bias and higher temperature shows high hardness of ~37 GPa. One of the possible reasons for this high hardness could be the complete formation of hex Ta_2N crystal structure which was still emerging in the lower temperature film. Also, higher bias is known to refine microstructure, which leads to increase in resistance to plastic deformation.

The residual stress was estimated from the radius of curvature of the substrate before and after coating deposition. The residual stress of the -100 V substrate bias film was almost same at ~0.2 GPa for both temperatures. For the -200 V bias film, the residual stress showed a slight decrease with decrease in temperature from ~ 4 GPa to ~ 3 GPa. This decrease was possibly due to the mixture of phases being formed in the lower temperature film.

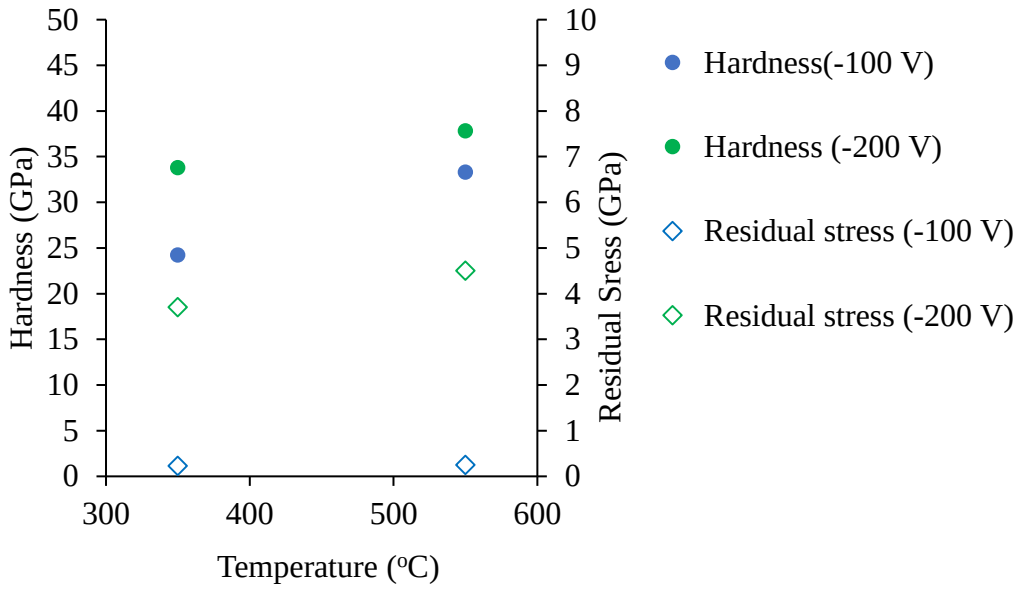

Figure 4-27 Variation in hardness of TaN films deposited at -100 V and -200 V substrate bias with varying deposition temperature.

4.5.3 Summary of Effect of Varying Substrate Temperature on the Mechanical Properties in Magnetron Sputtered TaN Films

In this study, the effect of the varying temperature on the crystal structure and mechanical properties of Ta–N thin films was studied. A series of TaN films were deposited with varying temperature from 550 ^{o}C to 350 ^{o}C and substrate bias -100 V. Similar set of films was deposited at -200 V. Varying temperature was shown to have a significant effect on material structure and properties. For the -100 V bias condition, the film deposited at 550 ^{o}C showed a mixture of fcc $TaN_{1.13}$ and hex Ta_2N phases. The film deposited at 350 ^{o}C also had mixture of phases as was evident from the low angle XRD broad peak. However, the diffractions could not be differentiated in this broad peak. The difference in the XRD patterns of the two films was that the peaks of the individual phases were better differentiated and slightly exaggerated in the higher temperature film. It can be said that lower temperature conditions did not provide the necessary energy for the optimal reaction between Ta and N and hence did not result in complete formation of Ta-N phases.

For the higher -200 V bias set, the lower temperature 350 ^{o}C film showed a mixture of fcc $TaN_{1.13}$ and hex Ta_2N phases, very similar to the -100 V, 550 ^{o}C film. As the temperature of the -200 V bias film was increased to 550 ^{o}C from 350 ^{o}C, the crystal structure changed entirely to hex Ta_2N phase which was still emerging in the 350 ^{o}C film. It is very clear that in case of -200 V bias 350 ^{o}C film, the energy for the transformation (slightly exaggerated peaks in addition to the broad peak) was provided by the higher bias as compared to the film which was deposited at the same temperature but lower bias (-100 V and 350 ^{o}C).

Since there was little variation in the deposition parameters, the changes to the mechanical properties of the coatings were modest than the effects presented in the previous section, but the

effects were still apparent. The hardness of the film deposited with -100 V substrate bias decreased as temperature was decreased from 350 ^{o}C to 550 ^{o}C from ~33 GPa to ~24 GPa while residual stresses were almost same at ~0.2 GPa. For the -200 V bias film, the hardness decreased from ~37 GPa to ~ 33 GPa as temperature decreased from 350 ^{o}C to 550 ^{o}C and residual stress also showed a slight decrease with decrease in temperature. The deposition rate for both sets decreased with increase in temperature due to re-sputtering effects.

The results clearly show deposition temperatures obviously influence the growth of TaN phases. This study though did not result in improvement in terms of coating hardness but resulted in a more enhanced understanding of the quite involved relationships between minimum temperatures (or energies) and crystal structure formation, deposition rate, residual stress and hardness of the Ta-N films. It was found across these series that a minimum optimal temperature is required for the formation of various Ta-N phases. Even if minimum temperature requirement is not met, higher substrate bias can have the same effect in terms of evolution of crystal structure and deposition rate as higher temperature. The drawback of depositing at higher bias is the incorporation of high residual stresses in the films. Higher temperature of 550 ^{o}C resulted in crystal structure changes in films and high hardness.

4.6 Conclusions of Magnetron Sputtered TaN Films

Three different series of Ta-N films produced using the in-house SaNEL PVD Magnetron Sputtering system show the effect of various processing parameters on the mechanical properties of the as-deposited coatings. The films with the most desirable mechanical properties were then examined in detail to determine the relationship between the deposition parameters, microstructure and the observed mechanical properties. Based on the analysis presented here, some interesting relationships between not only the processing conditions and the various mechanical properties,

but also the interaction of the crystal structure, the microstructure, the hardness, and the residual stress emerged.

The effects of varying $N_2/(N_2+Ar)$ ratio on the film microstructure and mechanical properties was explored. $N_2/(N_2+Ar)$ ratio was shown to have a significant effect on the film crystal structure. Higher $N_2/(N_2+Ar)$ ratio (25% - 7%) was shown to favor formation of fcc TaN phase while lower $N_2/(N_2+Ar)$ ratio (~3%) favors hex Ta_2N phase and a mixture of phases is formed around ~5% $N_2/(N_2+Ar)$ ratio. The hardness of the films increases from about ~22 GPa to ~ 33 GPa, as we decrease the $N_2/(N_2+Ar)$ ratio from 25% to 3%. The HRTEM analysis revealed presence of nano–columnar morphology for the 7% film, while the 5% film was composed of randomly oriented nanocrystals with a typical grain size of 2 – 5 nm. This led to increase in hardness of ~32 GPa and was accompanied by high H/E* ratio of 0.13 and low compressive stress of 0.27 GPa. The 3% film was composed of nano–needle like structure and grain size varying from ~ 5 – 10 nm. The hardness for this film was ~33 GPa with low compressive stress of 1.51 GPa. Lowering $N_2/(N_2+Ar)$ ratio refined the microstructure of the films, led to formation of harder hex Ta_2N crystal structure and thus led to significant and impressive improvement in mechanical properties.

Next, the effects of substrate bias voltage on mechanical properties were assessed, and it was found that increasing substrate bias did led to increase in hardness but were accompanied by high residual stresses within the coatings. The trend of the phase change involved during varying bias was much similar to the trend which was observed while varying $N_2/(N_2+Ar)$ ratio. As the substrate bias was increased from – 50 V to -200 V the crystal structure changed from a mixture of fcc TaN and fcc $TaN_{1.13}$ (at -50 V) to a mixture of fcc $TaN_{1.13}$ and hex Ta_2N (-100 V) and then entirely to hex Ta_2N (at -200 V). However, increased bias voltage results in the presence of increased energy at the site of the substrate during coating deposition. This can in turn cause re-sputtering effects of

atoms away from the coating after their initial deposition. Thus, coatings produced using high bias voltage may contain atomic arrangements which would not be energetically favorable under conditions with less bias applied. The results show that substrate bias should not exceed -100 V, as higher bias films though displayed higher hardness and less residual oxygen incorporation had decreased deposition rates, less elastic recovery and high residual stresses.

Deposition temperature plays a crucial role on the chemical structure and mechanical properties of Ta-N films. As was seen, deposition temperatures obviously influence the growth of various Ta-N phases and a minimal optimal temperature of ~500 ^{o}C or more is required for effective reaction between Ta and N. With the increase in temperature, chemical structures changes in the film induced mechanical properties changes. The results demonstrate that desirable mechanical characteristics such as high hardness in Ta-N films deposited by DC magnetron sputtering could be controlled by controlling temperature.

Although variation of mechanical properties of magnetron sputtered TaN films with processing conditions had been reported, however, there was lack of detailed microstructural analysis in relation to composition, crystal structure and properties. From this study, it was noticed in the case of each series, films with entirely hex Ta_2N crystal structure or a mixture of fcc TaN and hex Ta_2N had impressive mechanical properties in terms of increased hardness and decreased residual stress. Dense, smooth nanocrystalline Ta-N films were produced with sharp interface with the substrate and low surface roughness. Besides promoting formation of the hexagonal Ta_2N phase, decreasing the N_2 content in the gas mixture below 7% N_2 and a substrate bias of -100 V was found to result in refining of the microstructure with grain size from 5-15 nm. The films deposited with 5% and 3% N_2 content exhibited the highest hardness (33 GPa), H/E* ratio (0.13) and *We* (68%). The films with 7%, 5% and 3% N_2/ (N_2 +Ar) ratio displayed satisfactory oxidation

resistant and were stable upto 780 ^{o}C. In particular, the film deposited with 3% N_2 exhibited very low wear rate (3.1×10^{-6} mm^3/Nm) and seems to be a potential material for tribological applications.

Chapter 5 Microstructure and Property Investigation of Tantalum Silicon Nitride Films

5.1 Background

Researchers have focused on expanding the application of nitride coatings that feature multiple functions, such as outstanding mechanical properties and high oxidation resistance. Various Me-N systems have been explored to some detail by researchers, such as TiN, ZrN, CrN etc. TiN is the most explored hard coating; however, it exhibits inferior oxidation resistance at temperatures above 500^{o}C [100-101]. The relatively weak thermal stability and resistance against oxidation limit the use of various MeNs to temperatures lower than 600 ^{o}C. To further expand the applications of MeNs, nanocrystalline or quasi amorphous ternary Me-Si-N systems have been considered. Various Me-Si-Ns such as TiSiN, TaSiN, WSiN have been explored as diffusion barriers in microelectronics. Slightly better progressions in oxidation resistance for Ti–Si–N [102] (compared to TiN) and Cr–Si–N (compared to Cr-N) coatings were reported [103-107].

As mentioned previously, Ta-N was studied as a model system to explore another high potential MeSiN system: Ta-Si-N system. Our study on TaN system revealed interesting and important relationships between processing parameters, crystal structure, microstructure and mechanical properties. Such detailed microstructural analysis had not been reported previously in the literature. TaN films fabricated in the SaNEL lab displayed impressive hardness of ~33 GPa and oxidation resistance upto 780 ^{o}C. Ta-Si-N coatings reported so far in the literature tend to be mostly amorphous, with some having a small amount of crystalline content. These amorphous coatings have been explored mainly because of promising optical and electrical properties and for use as insulating layers. In addition, Ta–Si–N films with high Si content (> 30 at. %) are used as protective coatings because they feature high oxidation resistance and thermal stability upto 1300 ^{o}C. However, there are very few research groups which have focused on promising mechanical

properties, such as hardness >30 GPa, while displaying excellent oxidation resistance (> 800 ^{o}C) of ternary Ta–Si–N films.

By applying the relationships and trends established and studied with the PVD magnetron sputtered TaN samples at SaNEL, TaSiN coatings which could serve as effective high hardness, oxidative resistant coatings were developed using the same, home-built reactive magnetron sputtering system. The effect of varying deposition conditions on the crystal structure, microstructure and hence mechanical properties have been explored in detail, with the overall goal of synthesizing advanced hard (≥ 30 GPa), high temperature resistant (≥ 900^{o}C) coatings.

5.2 Experimental Details

The deposition conditions for the Ta-Si-N system were chosen based on the detailed analysis carried out on the Ta-N system. After initial experiments, parameters were adjusted as needed based on results, in order to further refine processing parameters. The thin films were deposited on Si (001) wafers using magnetron sputtering of a Ta and Si targets of 99.9% purity. DC power was supplied to the Ta target while the Si target was supplied with a pulsed power supply which delivered pulses with 13 W power. The processing temperature was set to 550 ^{o}C for all depositions. The target to substrate distance was 10 cm, and a negative bias was applied to the substrate to limit the incorporation of oxygen atoms to the coatings. The Ta target and the substrate were sputter cleaned with Ar plasma prior to film deposition. The total gas flow (Ar + N_2) was kept constant at 25 sccm and the low working pressure was maintained at 5 mTorr in a mixture of Ar (99.9% pure) and N_2 (99.9% pure).

Two sets of experiments: (i) Effect of varying power to Tantalum target, (ii) Effect of varying N_2/Ar gas ratio) were designed to investigate the effects of varying deposition parameters

on the crystal structure, chemical states, microstructure and hence mechanical properties of Ta-Si-N films.

1. To determine the effect of varying $N_2/(N_2+Ar)$ gas ratio in the films, experiments were carried out at –100 V substrate bias (E_B) with a total gas (N_2+Ar) flow rate of 25 sccm. The N_2 content was varied in the gas mixture from 7% to 20%. Once the chemical composition of the films and the effect on mechanical properties was established, the second step involved adjusting additional deposition parameters to obtain high hardness Ta-Si-N films.
2. To determine the effect of varying power to the Ta target on the films, experiments were carried out with varying power to Ta from 70 W to 120 W, while keeping the rest of the parameters constant such as substrate bias (E_B) at –100 V, $N_2/(N_2+Ar)$ gas ratio at 7% and pulse dc power to Si target at 13 W.

The deposition conditions for Ta-Si-N films are given in Table 5-1.

Table 5-1 Deposition conditions for Ta-Si-N films.				
Film	**Substrate**	**Si Target**	**Ta Target**	**% of N_2**
	Bias (-V)	Pulse Power (W)	DC Power (W)	
S70N7	100	13	70	7%
S100N7	100	13	100	7%
S120N7	100	13	120	7%
S150N7	100	13	150	7%
S150N10	100	13	150	10%
S150N13	100	13	150	13%
S150N15	100	13	150	15%
S150N20	100	13	150	20%
Processing Temperature: 550 ^oC				

The crystallographic structure of the films was studied by low angle XRD in a Bruker D8 Advance diffractometer using Cu Kα radiation at room temperature. The elemental composition and chemical states were investigated using AES and XPS conducted in a Perkin–Elmer Phi 560 ESCA/SAM system using a non–monochromated Al Kα excitation source. The Casa XPS software was used for XPS spectra analysis. The microstructure of the films was studied by HRTEM. SAED patterns and HRTEM images were recorded in a Hitachi H–9500 electron microscope (300 keV). Film hardness, effective Young's modulus $E^* = E/(1-\nu^2)$ (where E and ν are Young's modulus and

Poisson's ratio, respectively) and elastic recovery (W_e) were determined by a Hysitron Ubi 1 Nanomechanical Test Instrument using a cube corner diamond tip. Depth controlled indentations were performed at less than 10% of the coating thickness. The thickness, curvature (from which the residual stress was determined using the original Stoney's formula) and surface roughness of the film were measured by a Veeco NT–9100 Optical Surface Profilometer. Oxidation resistance was determined by Thermogravimetric Analysis. A pin–on–disk tribometer was used to obtain the coefficient of friction and the wear rate of the films. A 6 mm alumina ball was used as the pin and it was loaded with 1 N weight. The rotation speed was 10 cm/sec for a sliding distance of 100 m. The coefficient of friction was continuously measured during wear testing. The overall wear rate was determined by conducting wear depth profile analysis using optical profilometry.

5.3 Effect of Varying $N_2/ (N_2 + Ar)$ ratio on the Ta-Si-N Film Properties

This experiment was designed based on the results on the Ta-N system. The film with the most impressive properties from the entire Ta-N series was the one deposited with 5% N_2 (resulted in mixture of phases) and 3% N_2 (resulted in hex Ta_2N), at E_B= -100 V and 50 W power to Ta target. Due to phase diversity of the Ta-N system, the choice of a single phase would be beneficial in order to better understand the properties of two phase Ta-N/a-Si-N nanocomposite. For these reasons, the hex Ta_2N phase was selected and attention was paid to its composition. Since, we were dealing with a ternary system Ta-Si-N, $N_2/(N_2+Ar)$ gas ratio was increased from 3% to 7%, so that content of N is sufficient to react with both Ta and Si. Power to Ta was increased from 50 W to 150 W, and pulse power to Si was kept at 13 W (based on another trial experiment) so that we could limit the incorporation of Si to ~ 10-11 at. %. The first set of experiments was to determine the effect of varying $N_2/ (N_2 + Ar)$ ratio on the microstructure and eventually mechanical properties of Ta-Si-N coatings. Based on, XRD, AES and nanoindentation results, a series of films

were deposited at the same temperature of 550 ^{o}C, with 150 W power to Ta target, 13 W power to Si target and the N_2/ (N_2 + Ar) ratio was increased from 7% to 20%.

5.3.1 XRD Analysis

Figures 5-1(a) and 5-1(b) show the low–angle XRD and GIXRD (for 7% - 15% N_2 films) of the Ta-Si-N films deposited at E_B = -100 V with the N_2/ (N_2 + Ar) ratio varying in the gas mixture from 20% to 7%. The low angle XRD spectra of the film deposited with 20% N_2 show diffraction peaks at 2θ angles of 35.5^{o}, 41.3^{o} and 60.1^{o} corresponding to lattice spacing of 2.52 Å, 2.18 Å and 1.53 Å, respectively. These can be identified as the (111), (200), (220) peaks of fcc δ–TaN (PDF#49-1283). Decreasing the N_2 content to 13% and 10% N_2 results in diffraction peaks at 2θ angles of 33.7^{o}, 38.5^{o}, 50.3^{o} and 60.2^{o} with lattice spacing 2.65 Å, 2.33 Å, 1.81 Å and 1.53 Å, respectively. These can be identified as the (100), (101), (102) and (110) peaks of hex Ta_2N (PDF#26-0985). However, the intensity of the (102) peak is less in the 13% film. It should be noted that the (002) reflection of the hex–Ta_2N is expected to be present in the shoulder around 2θ angle of 36.5^{o}. The same crystal structure for the 10% and 13% N_2 films was observed in the GIXRD scans. Further decreasing the N_2 content to 7% results in one major peak at 2θ angle of 38.06^{o} with lattice spacing of 2.36 Å, and a small peak at 2θ angle of 50.3^{o} with lattice spacing of 1.81 Å. These can be also identified as the (101) and (102) diffraction peak of hex Ta_2N. The 7% N_2 film seems to have a noticeable (101) texture. The (100) and (002) reflection of the hex–Ta_2N around is expected to be present in the shoulder around 2θ angle of 33^{o} - 34^{o}.

The low angle XRD of the film deposited with 15% N_2 shows a broad peak from 34^{o} - 42^{o} which in turn is comprised of many peaks and one peak at 60.35^{o}. The peaks at 33.9^{o}, 35.8^{o}, 38.40^{o} with lattice spacing 2.63 Å, 2.48 Å and 2.33 Å, respectively can be identified as (100) diffraction of hex Ta_2N, (111) of fcc TaN and (101) of hex Ta_2N, respectively. Thus, the low angle XRD

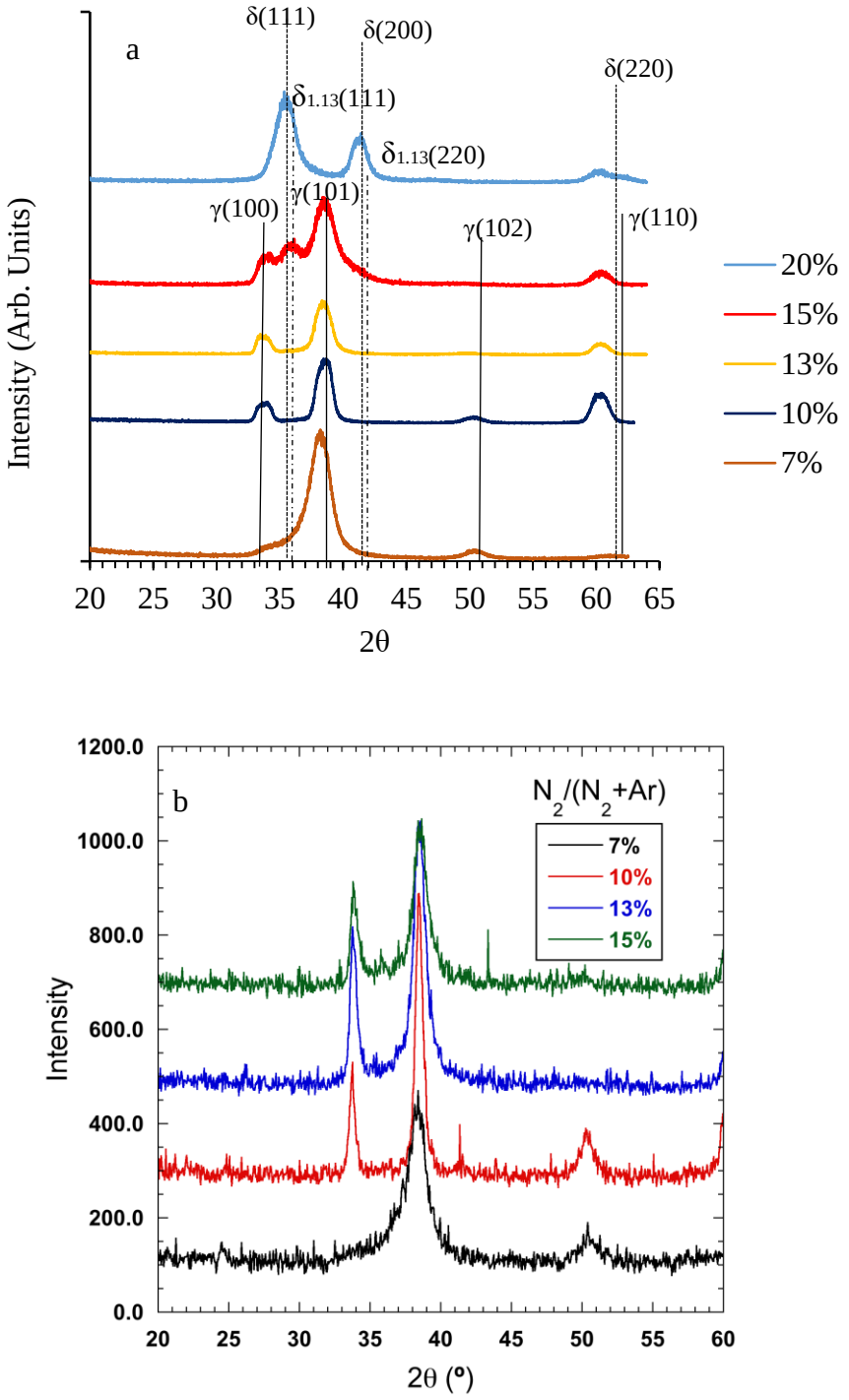

Figure 5-1(a) Low angle (5° incidence angle) XRD (b) GIXRD (1° incidence angle) of Ta-Si-N films deposited with varying N_2/ (N_2 +Ar) ratio. (The GIXRD experiments were conducted at IMDEA Materials Institute in Madrid Spain)

spectrum for the film with 15% N_2 shows a mixture of phases and is a transition from a single phase fcc TaN (at 20% N_2) to mainly hex Ta_2N (13% to 7% N_2). We should note that since the film with 15% N_2 had a mixture of phases, the other expected diffraction peaks such as (002) of hex Ta_2N and (200) of fcc $TaN_{1.13}$ phase are present in the broad shoulder extending from a 2θ angle of 34° to about 42°. The hex Ta_2N phase which dominates in the 13% - 7 % N_2 films was still emerging in the 15% film. This transition was also seen while exploring the Ta-N system. The GIXRD scan for the 15% N_2 film displays 2 peaks at 2θ angles of 33.7°, 38.5°, which correspond to the (100) and (101) diffractions of hex Ta_2N. Comparison of the low angle XRD and GIXRD for the 15% N_2 film depicts the possible nucleation of the fcc TaN phase first followed by the formation of the hex Ta_2N phase.

Figure 5-2 shows the variation in the deposition rate (nm/h) of the films. The deposition rate seems to be similar for the 7%, 10% and 13% films and lower for the 20% N_2 film, where it decreases to ~ 900 nm/h. The change in crystal structure (fcc TaN at higher N_2 content) and target poisoning at higher N_2 flow for the 20% film could be the reason for its lower deposition rate. The highest deposition rate for the 15% film can be attributed to the mixture of phases being formed.

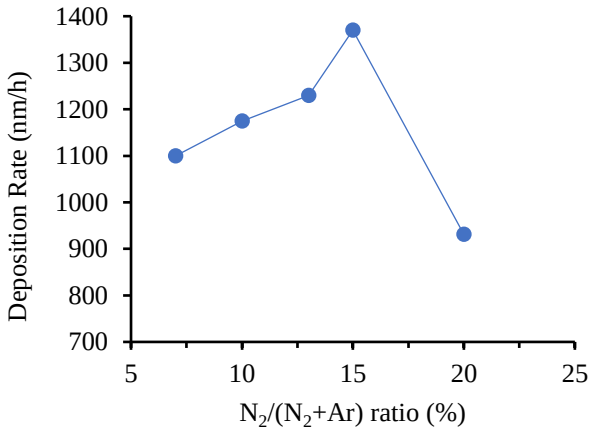

Figure 5-2 Variation of deposition rate of Ta-Si-N films deposited with varying N_2/ (N_2 +Ar) ratio.

5.3.2 XPS Studies

The composition of the films was examined by AES. Figure 5-3 shows the evolution of the elemental composition of the reactively sputtered Ta-Si-N films with N_2/ (N_2 +Ar) ratio varying from 20% to 7%. The elemental percentage composition was determined from peak to peak intensity from the differentiated spectrum. Increase in N concentration and decrease in Ta concentration can be observed as the N_2 content in the gas mixture is increased from 7% to 20%. It looks like high power (150 W) to Ta target, results in overwhelming the plasma in the system which leads to Nitrogen preferentially reacting with Tantalum. This leads to very little Nitrogen (at 7% N_2) left for Silicon to react with and hence very little incorporation of Si (~ 6%) in the film. As the content of Nitrogen in the gas mixture is increased from 7% to 10% and then to 13%, there is more Nitrogen available in the system for Si-N reaction and hence, Si content in the film is increased to ~13% due to possible formation of Si_3N_4. However, further increase in N_2/ (N_2 + Ar) ratio to 15%, results in decrease in Si content to ~9%.

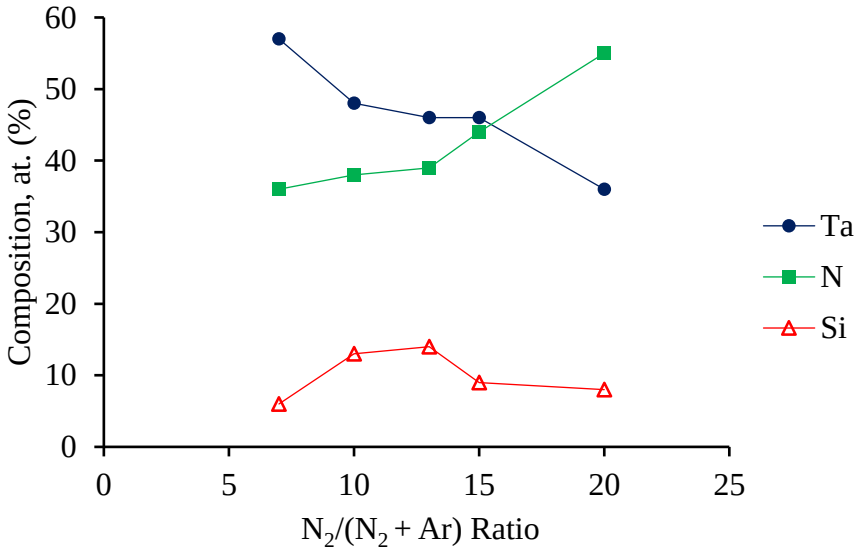

Figure 5-3 Evolution of the elemental composition of the reactively sputtered Ta-Si-N films deposited with N_2 content varying in the gas mixture from 20% to 3%.

One of the reasons for this decrease in Si content, could be the mixture of two Ta-N phases (Ta_2N and TaN) being formed for this gas ratio which resulted in using up major amount of N in the system and hence resulted in decrease in available N for Si to react with. Increase in N_2/ (N_2 + Ar) ratio to 20% results in decrease in Ta to about 36% and Si is about ~8%. The N content for this film was ~55%. This film cracked completely possibly due to high residual stresses and due to possible increased N content in interstitial solid solution of Ta-N. Low Ta content along with less deposition rate for this film depicts the possibility of target poisoning due to high N_2 in the gas mixture.

5.3.3 Microstructural Investigation

In order to understand the effect of varying N_2 content in the gas mixture on the microstructure of the Ta-Si-N films, three films were selected to be analyzed using HRTEM. These were the films deposited with 7%, 13% and 15% N_2/ (N_2 + Ar) ratio.

5.3.3.1 Ta-Si-N film deposited with 7% N_2

Figure 5-4(a) is a typical SAED pattern taken from an area in the film away from the film/Si interface. The three diffraction rings 1, 2 and 3 with lattice spacing 2.33 Å, 1.80 Å and 1.51 Å, respectively can be identified as the (101), (102) and (110) plane of hex Ta_2N. As is evident from the SAED pattern, the diffraction arcs are discontinuous indicating some texture in the films and it agrees well with the XRD (Figure 5-1). Figure 5-4(b) is a HRTEM cross section image of the film, which depicts ~ 5–15 nm size nanograins. The presence of amorphous boundaries around the grains was not innately clear, however, and most of the disordered regions (1-2 ML thick) were distinguishable via slight changes in compositional contrast as indicated by dashed lines in Figure 5-4(b).

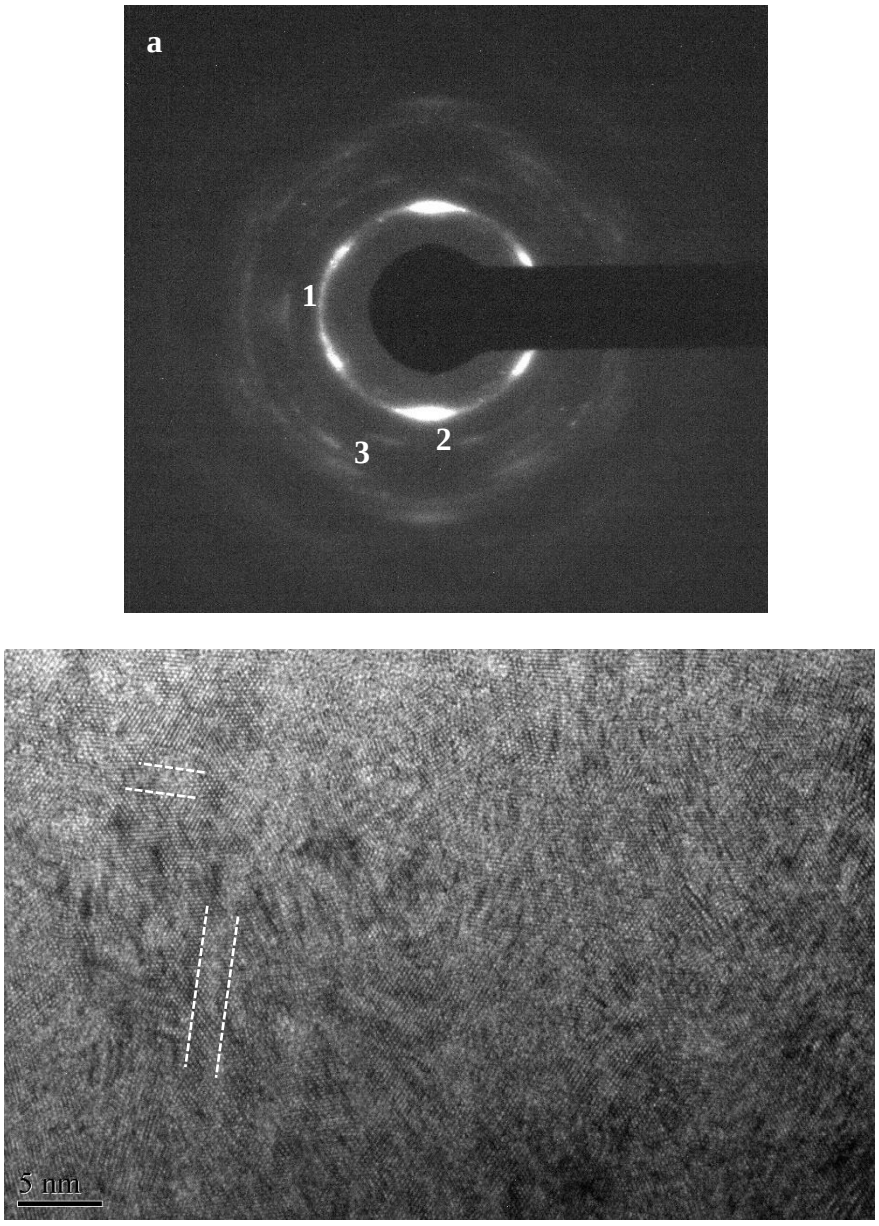

Figure 5-4(a) SAED pattern (b) cross section HRTEM image of the 7% N_2 film.

5.3.3.2 Ta-Si-N Film Deposited with 13% N_2

Figure 5-5(a) is a typical SAED pattern of the 13% N_2 film showing several diffractions. The five diffraction rings 1, 2, 3, 4 and 5 with lattice spacing 2.63 Å, 2.42 Å, 2.33 Å, 1.80 Å and 1.51 Å, respectively can be identified as the (100), (002), (101), (102) and (110) plane of hex Ta_2N. This agrees well with the phases identified from XRD of the film (Figure 5-1).

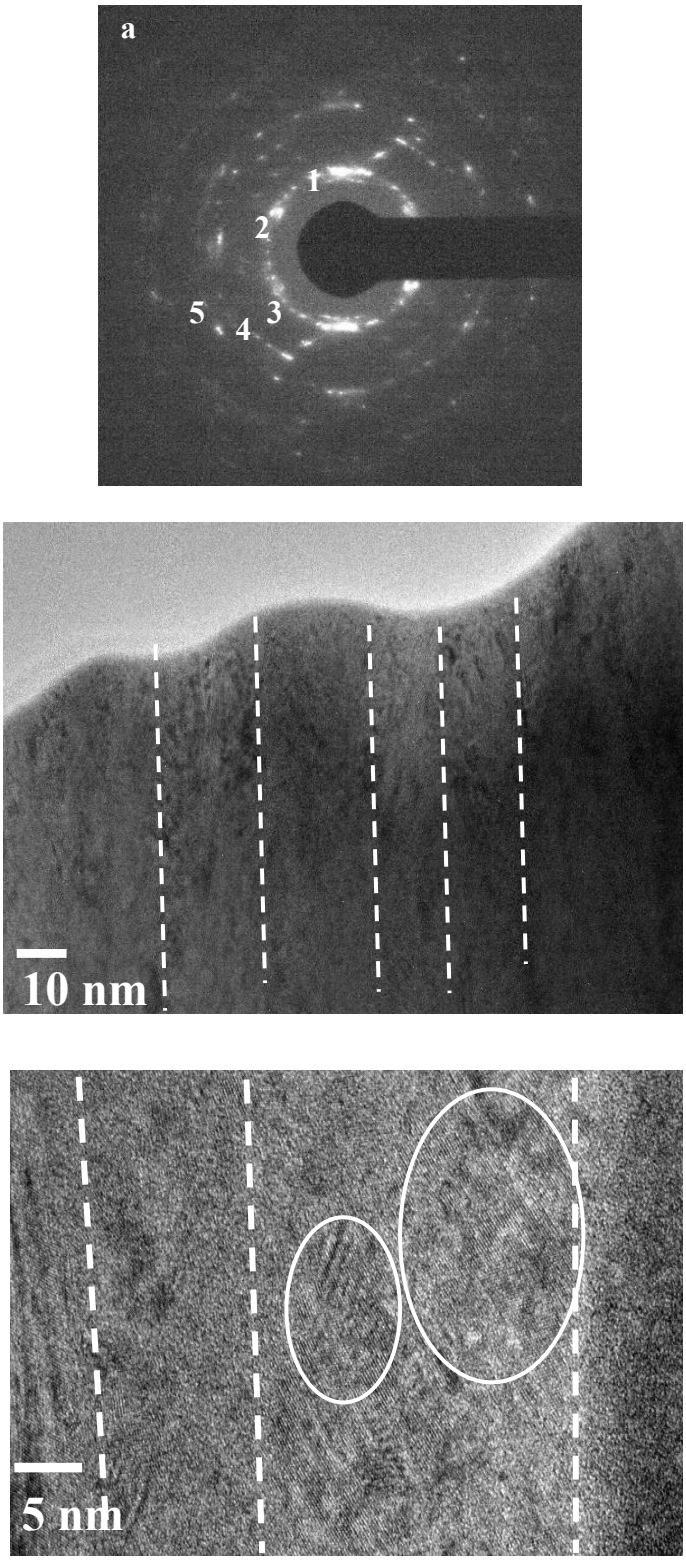

Figure 5-5(a) SAED pattern (b) Bright field TEM image of the bulk structure of the film (c) cross section HRTEM image of the 13% N_2 film.

However, the XRD did not show the (002) and (102) diffractions of hex Ta_2N. Also, as is evident from the SAED pattern, the diffraction arcs are discontinuous indicating the ordering of the columnar grains in the in-plane direction in the films. Figure 5-5(b) shows the bright field TEM image of the bulk structure of the film. We can see some sort of columnar morphology in the film, with 20-30 nm wide columns. Figure 5-5(c) shows the cross section HRTEM image. The columns are composed of several nanocrystalline grains of different orientations as indicated by the dashed circles. These columns are separated by an amorphous matrix of about 5-10 nm in width (indicated by dashed lines). As was seen in the AES results, this film had about ~14% - 15% Si content, which has led to the formation of the disordered Si_3N_4 tissue phase between the columns.

5.3.3.3 Ta-Si-N Film Deposited with 15% N_2

Figure 5-6(a) is a typical SAED pattern taken from an area away from the film/Si interface showing several diffractions. The diffraction rings 1 and 3 with lattice spacing of 2.65 Å and 2.29 Å respectively, can be identified as the (100) and (101) plane of hex Ta_2N. The diffraction spots 2 between the ring 1 and 3 have a lattice spacing of 2.5 Å and this corresponds to (111) diffraction of fcc TaN. The diffraction spots 4 and 5 have lattice spacing of 1.82 Å and 1.5 Å correspond to the (102) and (110) diffraction of hex Ta_2N, respectively. The other expected (200) and (002) diffractions of fcc TaN and hex Ta_2N with lattice spacing 2.24 Å and 2.42 Å respectively could not be differentiated in this diffused arc. This agrees with the broad transition peak observed in the XRD pattern for this film (Figure 5-1), where only three peaks where well differentiated. Those were (100), (101) diffractions of hex Ta_2N and (111) diffraction of fcc TaN. Figure 5-6(b) is a bright field TEM image of the bulk structure of the film, clearly showing signs of columnar morphology, columns being 20 – 30 nm wide.

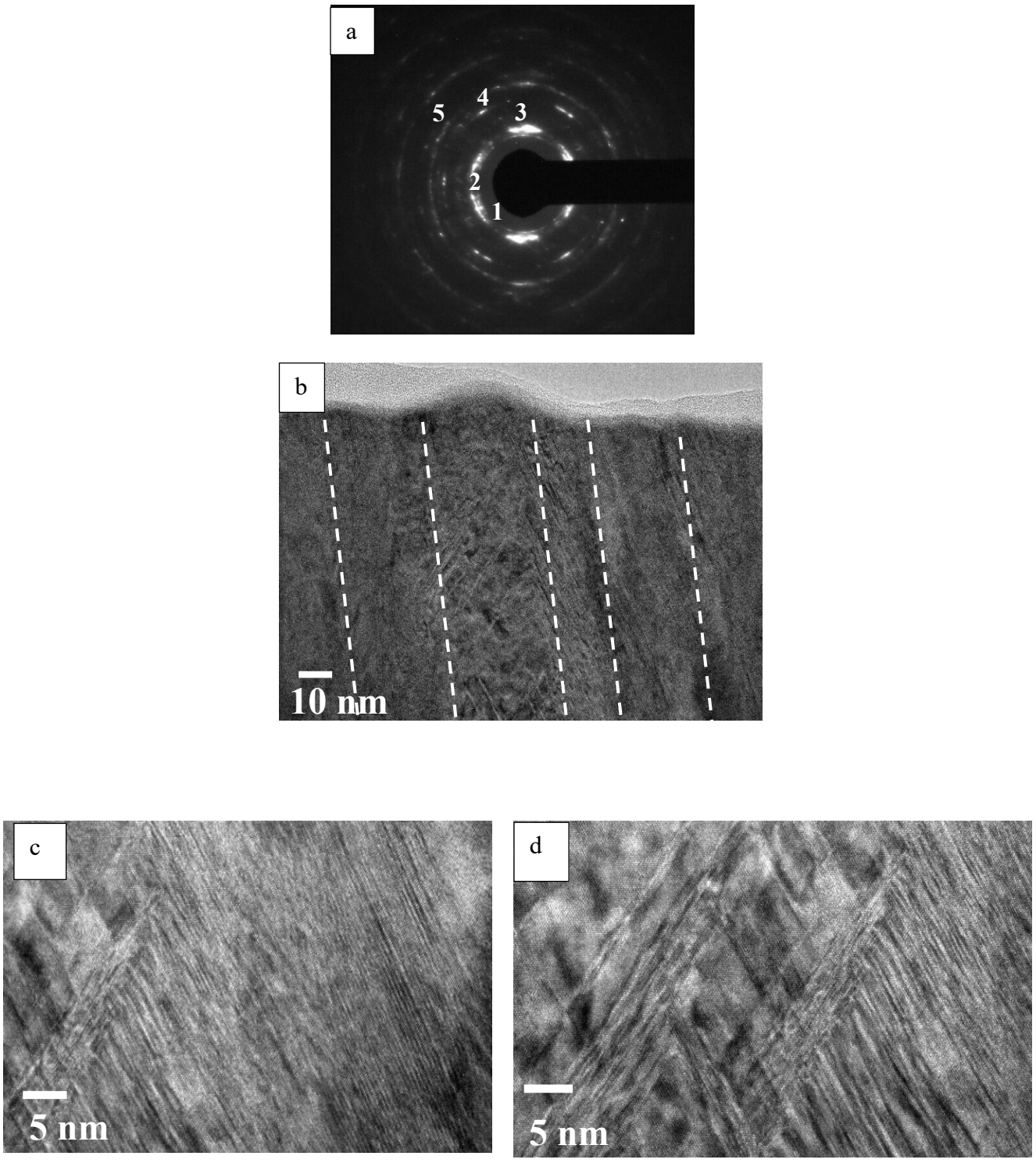

Figure 5-6(a) SAED pattern (b) Bright field TEM image of the bulk structure of the film (c), (d) cross section HRTEM image of the 15% N_2 film.

Figure 5-6(c) and (d) are HRTEM images showing columns of two crystallographic orientations, possibly from two different phases (hex Ta_2N and fcc TaN). The presence of amorphous boundaries in this film was not as clear as in the 13% film, however, disordered tissue phase in this film could be differentiated via compositional contrast (as shown in Figures 5 (c) and (d)). AES results depicted decrease in Si at. % for this film possibly due to formation of more than one phase, which led to decrease in available N for Si to react with to form the expected Si_3N_4 tissue phase.

5.3.4 Mechanical and Tribological Properties

Nanoindentation experiments were conducted to study the effect of the varying N_2 content in the gas mixture on the mechanical properties of the Ta-Si-N films. Figure 5-7(a) shows variation in hardness and Young's modulus and Figure 5-7(b) shows variation in hardness and residual stress of the films as a function of varying $N_2/(N_2+Ar)$ ratio. The hardness increases from ~ 30 GPa to ~ 42 GPa as we increase N_2 content from 7% to 15%. This increase in hardness can be attributed to several reasons. One of the possible reason is the change in crystal structure from a textured hex Ta_2N (for the 7% N_2 film) to a more uniform hex Ta_2N (for the 10% and 13% N_2 film) structure. The 15% film also depicted hex Ta_2N crystal structure in the surface layers as observed via GIXRD. During the nanoindentation the top 40-60 nm are indented to get the hardness response measurement, hence the response for the 15% N_2 film was from the surface layers comprising the hard hex Ta_2N phase. Another reason which explains the highest hardness (~42 GPa) of the 15% N_2 film is its dense nanocolumnar structure (~ 10-15 nm wide columns) with nanocrystals of ~5-10 nm in size with different crystallographic orientations within these columns. This nanostructure is reported to result in hardness enhancement due to resistance in dislocation motion because of the transition from one crystallographic direction to other [98].

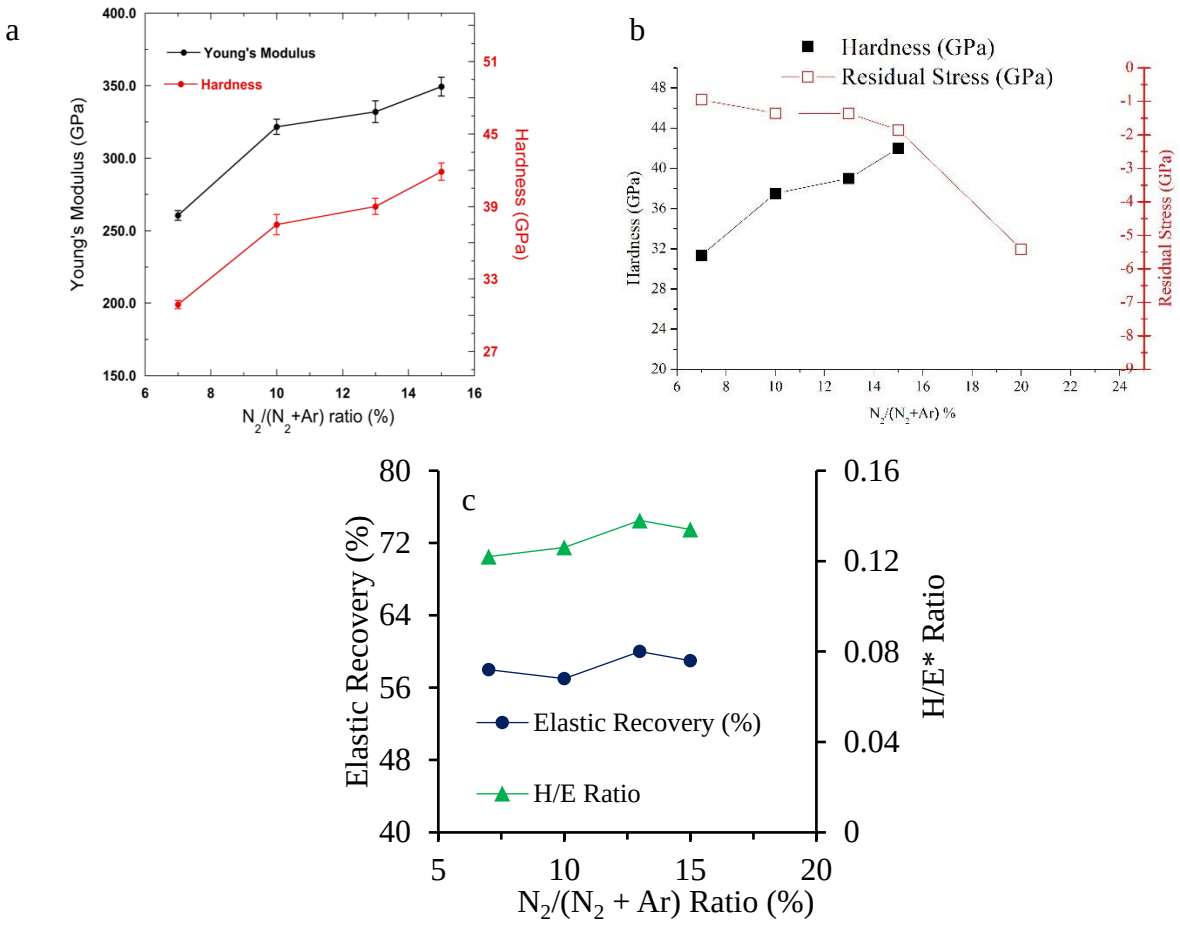

Figure 5-7 Variation in (a) hardness, Young's modulus (b) hardness and residual stress (c) H/E* ratio and elastic recovery W_e (%) of the films deposited with N_2 varying from 7% – 15%.

The 13% N_2 film although had the hex Ta_2N crystal structure and also possessed dense nanocolumnar structure but these nanocolumns were separated by thin soft (possibly Si_3N_4) amorphous boundaries, which could be the likely reason for the decreased hardness (~ 39 GPa) of the 13% N_2 film compared to the 15% N_2 film. Also, is observed the scatter in hardness is large for the 10%, 13% and 15% N_2 film films compared to the textured 7% N_2 film. This is possibly due to the textured crystal structure in the 7% N_2 film which gives less scatter. The nanoindentation of the film with 20% $N_2/(N_2+Ar)$ ratio was not carried out as the film surface was cracked possibly due to high residual stress (~ -5 GPa). Elastic recovery ~ 60% in hard films is expected to make

them more resistant to cracking [98]. The residual stress for the films increased from ~ -1 GPa to ~ -2 GPa as we increase N_2 from 7% to 15%. This increase could be due to incorporation of N atoms at interstitial sites at higher N_2 content. For the 20% N_2 film residual stress was high ~ -5 GPa.

Figure 5-7(b) shows the variation of H/E* ratio and elastic recovery W_e (%) of the films with N_2 content varying from 7% – 15%. The H/E* ratio for all films is ≥ 0.11, reaching a maximum value of ~ 0.13 for the 13% N_2 film depicting films are developing high resistance to plastic deformation with increase in N_2 content. Elastic recovery for all films is ~ 58% ± 2. Elastic Overall, it seems that the films deposited with N_2 content around 10% - 15% exhibited a good combination of hardness (~ 40±2 GPa) and were accompanied with low residual stress (~ −1.5 GPa). Especially the 15% N_2 film, in addition to highest hardness and low residual stress, exhibited high H/E* of ~0.13 and high elastic recovery of ~ 60%.

Pin on disc experiments were performed on Ta–Si-N films which were deposited with 7%, 13% and 15% N_2 content. The coefficient of friction (μ) was continuously measured during the testing and was ~0.6 - 0.7 for all films as shown in Figures 5-8 (a), (b) and (c). Figures 5-9 (a), (b), (c) show the 2- dimensional wear track profile for films sputtered with 7%, 13% and 15% N_2. As seen, the wear track was much wider in case of 7% and 13% N_2 films (~100 μm) compared to the 15% N_2 film (~ 40 μm). However, the depth of the wear track was lower for the 7% and 13% N_2 films (~ 0.12 – 0.14 μm) than the 15% N_2 film (~0.36 μm). The calculated wear rate for 7%, 13% and 15% N_2 films was 3.05094×10^{-5} mm^3/Nm, 7.09538×10^{-6} mm^3/Nm, 1.28112×10^{-5} mm^3/Nm, respectively.

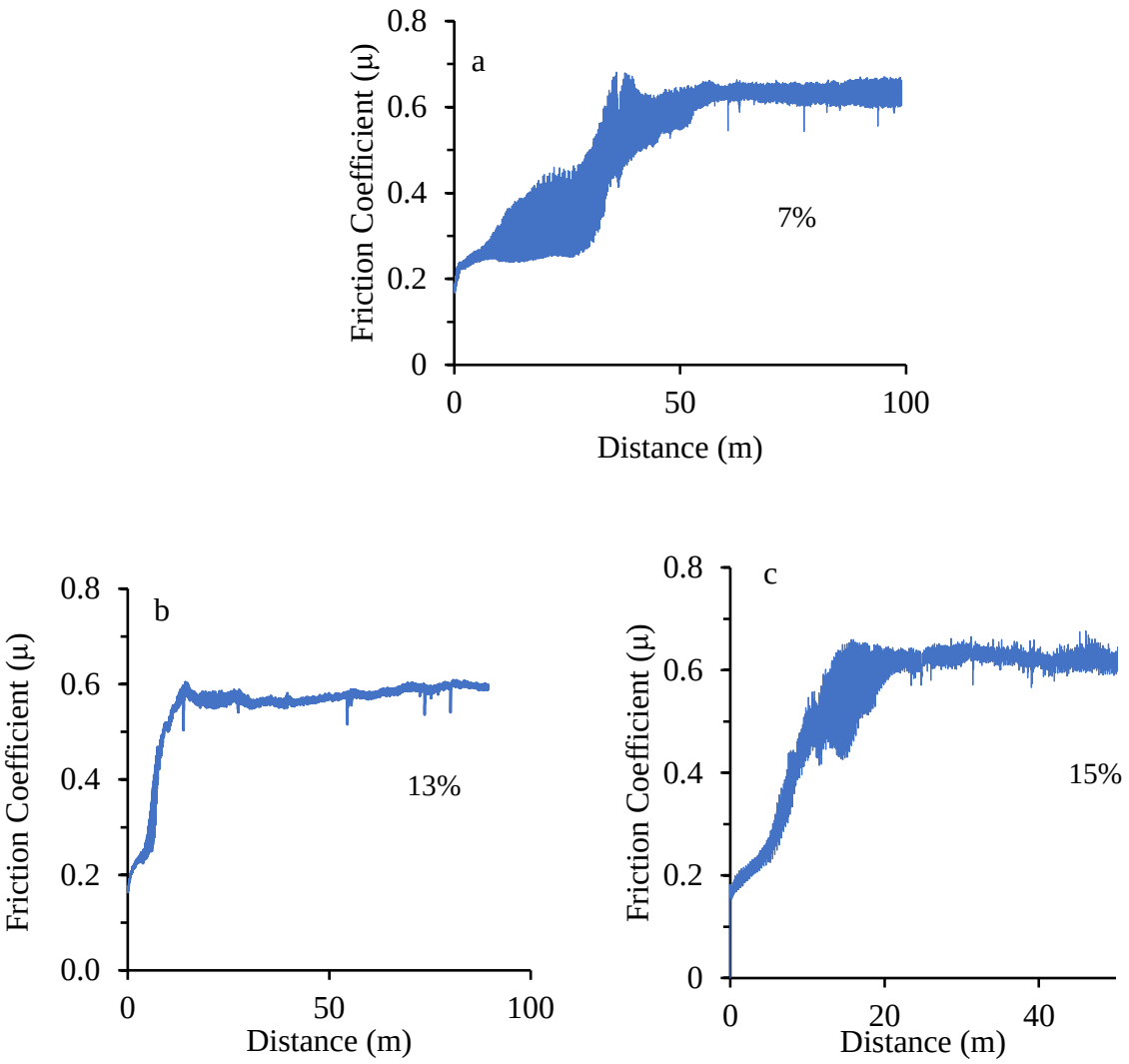

Figure 5-8 Coefficient of friction (μ) of Ta-Si-N films deposited with (a) 7% (b) 13% (c) 15% N_2.

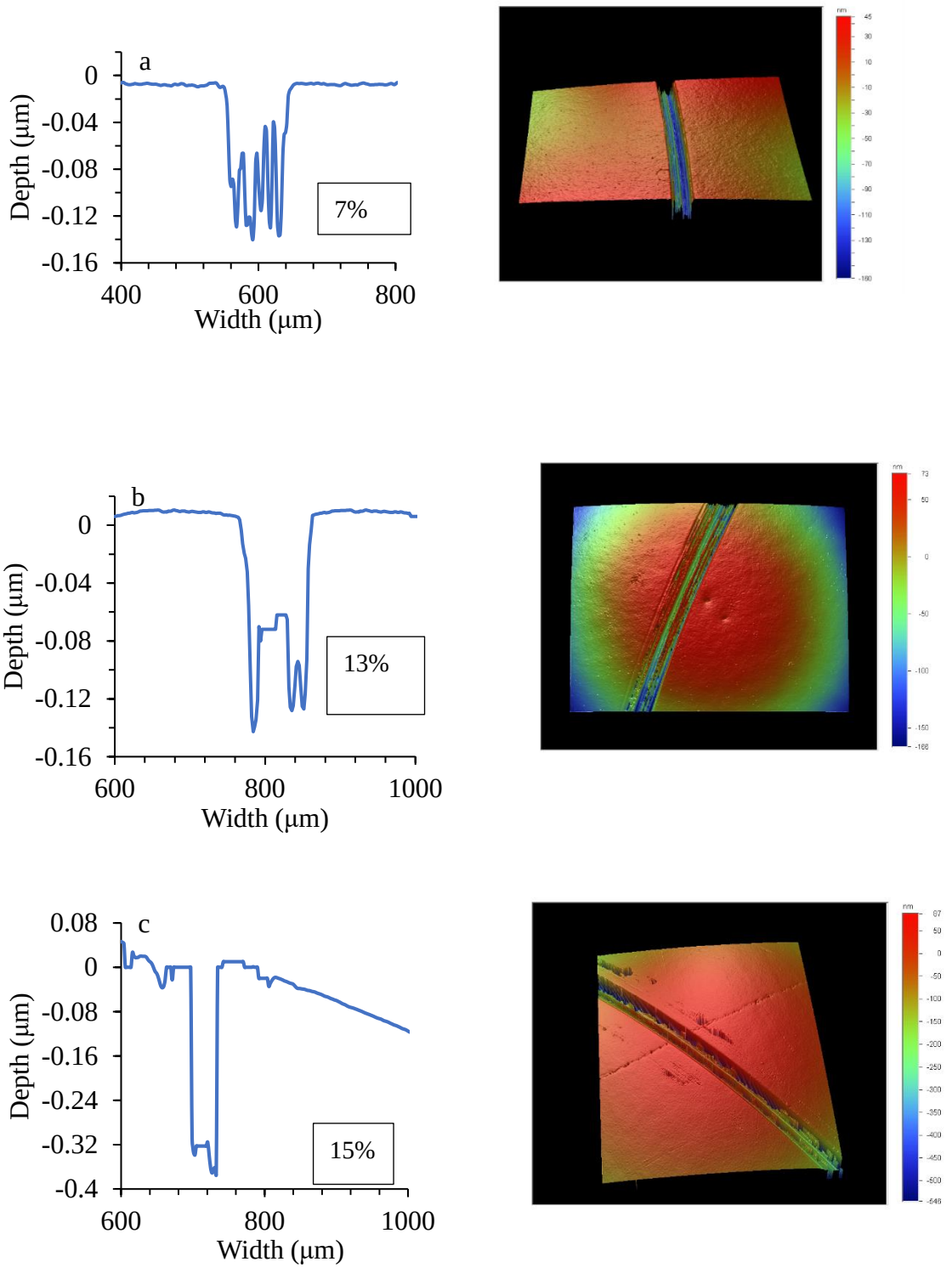

Figure 5-9 Two-dimensional wear track profile for films sputtered with

(a) 7% (b) 13% (c) 15% N_2 content.

As we can see, the wear rate of the 13% film is almost a magnitude less than the other films. The lower wear rate of the 13% film can be attributed to its high hardness. This film had a uniform microstructure with hex Ta_2N grains growing in columnar fashion with amorphous boundaries in between, which possibly led to high resistance to wear. On the other hand, the 7% film had lower hardness than the 13% film, contributing to its higher wear rate. The 15% film, though had highest hardness, but due to the mixture of phases present, led to faster wear, possibly due to three body wear at the point of contact.

5.3.5 Oxidation Resistance

The 13% film was chosen to test the oxidation resistance of the Ta-Si-N films. TGA was carried out to observe their oxidation behavior. Amount of weight change of a material was measured as a function of increasing temperature in an atmosphere of air.

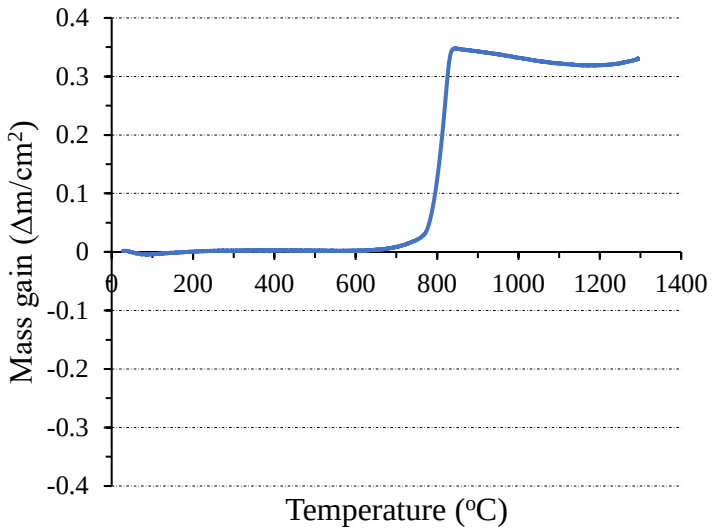

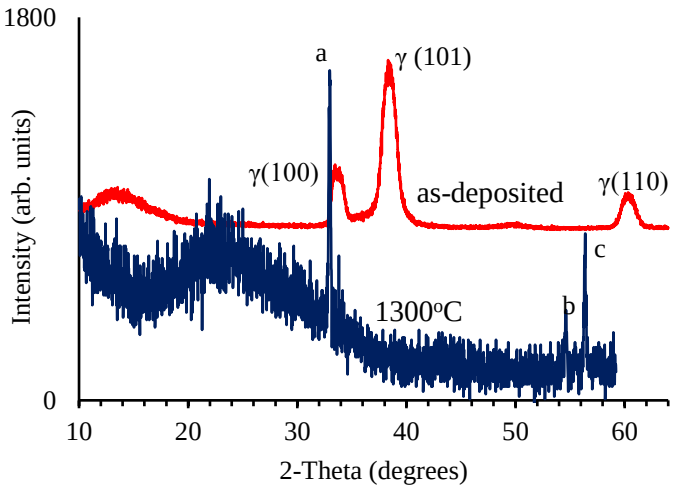

Figure 5-10(a) TGA curves for Ta-Si-N film deposited with 13% N_2 (b) XRD of the 13% N_2 film before and after annealing.

Figure 5-10(a) presents the TGA curves for Ta-Si-N film deposited with 13% N_2 content. The film was heated from room temperature to 1300°C with a heating rate of 10 $^oC\ min^{-1}$ in flowing air. The TGA curve reveals no mass gain till ~ 780 °C and the beginning of increase in the total mass after 780 °C which depicts the formation of Tantalum oxide. The mass gain continues up to 830°C and then remains more or less constant upto 1300°C (the maximum temperature used in our test). The saturation of the mass growth can be either due to the formation of a stable passive oxide layer on the surface of the film or due to the oxidation of the whole bulk of the film. Figure 5-10(b) shows the XRD of the 13% N_2 film before (red) and after annealing (blue) at 1300ºC. The XRD of the as-deposited film, which has been discussed earlier, revealed three diffraction peaks at 2θ angles of 33.7º, 38.5º and 60.2º. These can be identified as the (100), (101) and (110) peaks of hex Ta_2N (PDF#26-0985), respectively. The XRD of the film after annealing revealed a broad peak around 23º and three diffraction peaks at 2-theta angles of 32.9º, 54.8º and 56.1º. The broad peak around 23º can be assigned to SiO_2. The two peaks at 32.9º and 54.8º can be attributed to the (211), (400) plane of the cubic Ta_2O structure (PDF 18-1302) and

the last peak can be attributed to the (132) plane of orthorhombic Ta_2O_5 structure (PDF 25-0922). It is evident from the comparison of the two scans that the entire film had been oxidized in this case.

5.4 Effect of Varying Power to Ta Target on Ta-Si-N Film Properties

The second set of experiments involved varying the power to Ta target to vary the composition of the films further to modify the microstructure and explore effects on hardness. Films were prepared with 70W, 100 W and 120 W power to Ta target, while keeping other deposition parameters constant like 7% N_2 content and 13 W power to Si target. The effects of varying power to the Ta target on the crystal structure, elemental composition, chemical states, microstructure evolution and eventually mechanical properties of the films were determined.

5.4.1 XRD Analysis

Figure 5-11 shows the low–angle XRD of the Ta-Si-N films deposited with Ta power varying from 70 W to 120 W. The XRD spectra of the film with 70 W power to Ta target, shows a single diffraction peak at 37.7º, with lattice spacing 2.3 Å. This corresponds to non-stoichiometric (110) fcc $TaN_{0.01}$. However, this peak is not sharp and is relatively broad, which depicts a defective structure or nucleation of other phases. As the power is increased to 100 W, the XRD reveals diffraction peaks at 2θ angles of 33.8º, 38.5º, 50.6º and 60.5º with lattice spacing 2.63 Å, 2.33 Å, 1.79 Å and 1.53 Å, respectively. These can be identified as the (100), (101), (102), (110) planes of hex Ta_2N (PDF#26-0985). It should be noted that the (002) reflection of the hex–Ta_2N is visible in the shoulder around 2θ angle of 36.5º. A transition from fcc $TaN_{0.01}$ to hex Ta_2N is evident as power to Ta target is increased. Increasing the power to 120 W results in one main peak at 2θ angle of 38.3º, lattice spacing 2.35 Å, and other small peaks at 50.6º and 60.5º with lattice spacing of 1.79 Å and 1.53 Å, respectively. These can also be identified as (101), (102) and

(110) planes of hex Ta_2N. The other expected (100) and (002) reflection of the hex–Ta_2N is visible in the broad shoulder extending from 2θ angle of 33° - 36°. It is observed that films are developing texture with hex Ta_2N (101) orientation, as the power to the Ta target is increased from 100 W to 120 W. However, for the 120 W film, the hex Ta_2N (101) peak shows a slight shift to 38.3° from normally expected 38.6° position, which indicates compressive residual stress or lattice strains within the film (Figure 5-11).

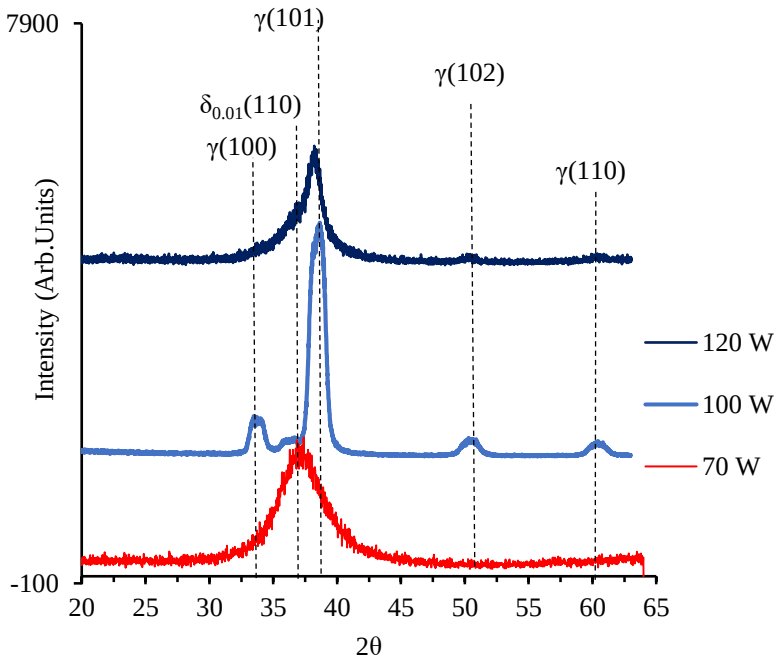

Figure 5-11 Low–angle XRD of the Ta-Si-N films deposited with Ta power varying from 70 W to 120 W.

Figure 5-12 shows the variation in the deposition rate (nm/h) of the films with varying power to Ta target. The deposition rate increases with increase in power to the Ta target from 100 W to 120 W. The deposition rate for the film deposited with 100 W power to a target shows the least deposition rate of ~800 nm/h, compared to the other two films deposited at 70 W and 120 W, where the deposition rate is ~870 nm/h and ~900 nm/h respectively. The low deposition rate of the

100 W film in comparison to the other films could be attributed to the uniform non-textured crystal structure, whereas the 120 W film is seen developing texture. Same behavior is observed for the film deposited with 70 W power to Ta which shows higher deposition rate compared to the 100 W film, which again could be attributed to the texture developed in this film.

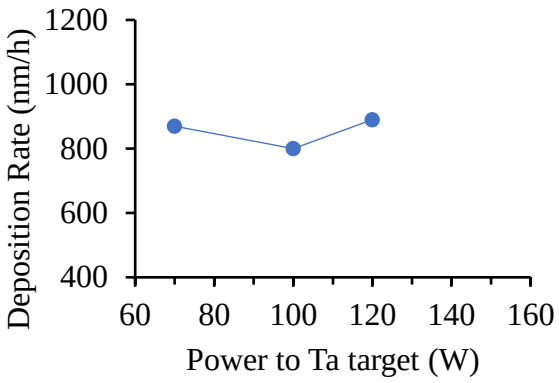

Figure 5-12 Variation in the deposition rate (nm/h) of the Ta-Si-N films deposited with Ta power varying from 70 W to 120 W.

5.4.2 XPS Studies

The composition of Ta-Si-N films was examined by AES. Figure 5-13 shows the evolution of the elemental composition of the reactively sputtered Ta-Si-N films deposited with varying power to Ta target from 100 W to 120 W, at E_B = –100 V with 7% N_2 content. The elemental percentage composition was determined from peak to peak intensity from the differentiated AES spectra. Increase in Ta concentration and decrease in Si concentration can be observed as the power to the Ta target is increased from 100 W to 120 W. The N concentration slightly decreases as we go from 100 W to 120 W. It seems that at 120 W power to Ta target, the sputtering rate of Ta was enough to overwhelm the Si content in the structure. Most of the Nitrogen seems to have preferentially reacted with Ta resulting in hex Ta_2N phase as was evident from the XRD.

High Resolution XPS was carried out for the film deposited with 120 W power to Ta target. As seen in Figures 5-14(a) and (b), Silicon is in the Si_3N_4 binding state and Ta is clearly in Ta-N binding state. The Si 2p peak has shifted from 99 eVs (pure Si) to ~101 eVs (Si_3N_4). The Ta 4f peaks are at higher binding energies compared to that of metallic Tantalum (Ta $4f_{7/2}$ ~ 21.7 eV). This peak shift indicates the transition from a metallic (Ta $4f_{7/2}$ ~ 21.7 eV) to a nitride (Ta $4f_{7/2}$ ~ 24.7 eV) chemical state.

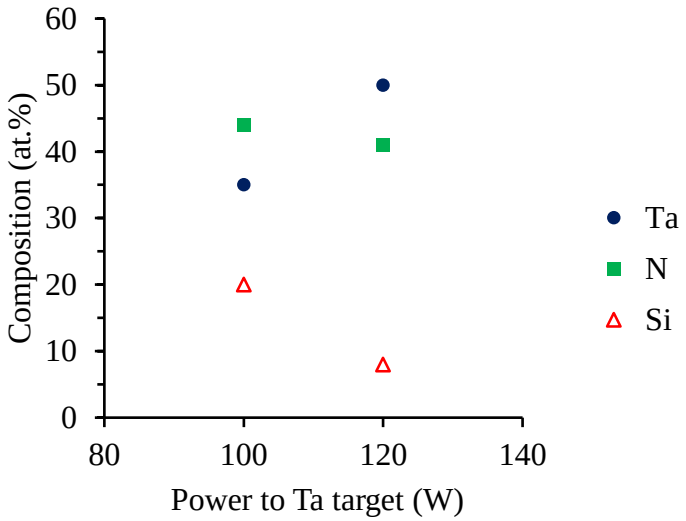

Figure 5-13 Evolution of the elemental composition of the reactively sputtered Ta-Si-N films deposited with varying power to Ta target.

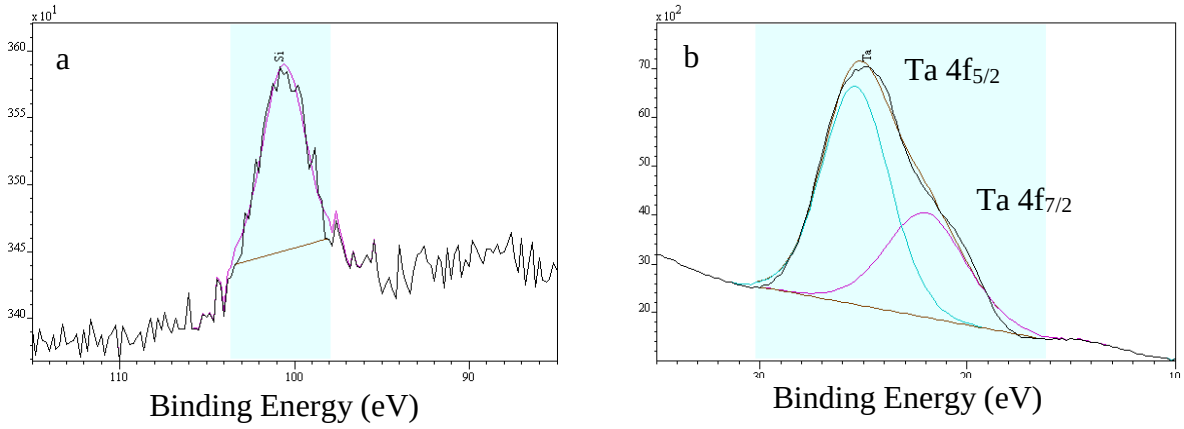

Figure 5-14 High resolution deconvolution of (a) Si 2p and (b) Ta 4f core levels.

5.4.3 Mechanical Properties

Nanoindentation experiments were conducted to study the effect of the varying power to the Ta target on the mechanical properties of the films. Figure 5-15(a) shows variation in hardness, reduced elastic modulus and residual stress of the films as a function of the varying power to the Ta target. The hardness increases from ~22 GPa to ~ 30 GPa as power is increased from 70 W to 100 W and decreases from ~30 GPa to ~25 GPa as the power is increased from 100 W to 120 W. The increase in hardness from 70 W to 100 W is probably due to the change in lattice structure from fcc $TaN_{0.01}$ to hard hex Ta_2N phase as was shown in Figure 5-1. H/E* ratio and elastic recovery W_e (%) of the films deposited with varying power to Ta target. Also, higher amorphous content (due to higher at. % of Si) in the 70 W film could have led to the decrease in hardness of this film, due to increase in volume fraction of the soft boundary area in the film. The decrease in hardness for the 120 W film could be due to the texture developed in these films. Also, as was seen, the at. % of Si in this film was ~6-8%. Increase in at. % of Si in the 100 W film may have led to the refinement and formation of more uniform microstructure. One of the nanostructures which leads to increased hardness, is where the nano-crystallites are surrounded by amorphous ~1 nm monolayers. In 120 W film, the Ta seems to overwhelm the plasma in the system, leaving very little N to react with Si. This seems to have resulted in no optimal formation of amorphous layers of Si_3N_4 around the nanocrystallites of Ta-N and hence reduced hardness. The residual stress seems to increase with increase in power to Ta target. The increase in compressive residual stress in the 120 W film could be due to the texture or inhomogeneous strains developed in the film at higher power. Another reason could be decrease in the Si at. % (Figure 5-13) in the 120 W film, which eventually led to a decrease in the formation of the amorphous boundary region. Formation of amorphous boundary regions is said to result in stress relaxation.

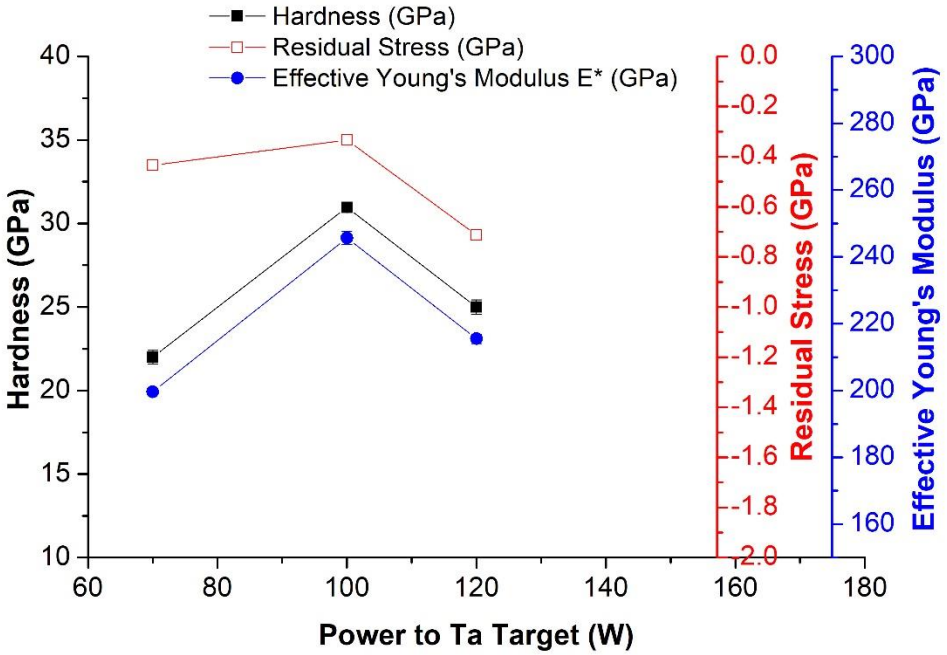

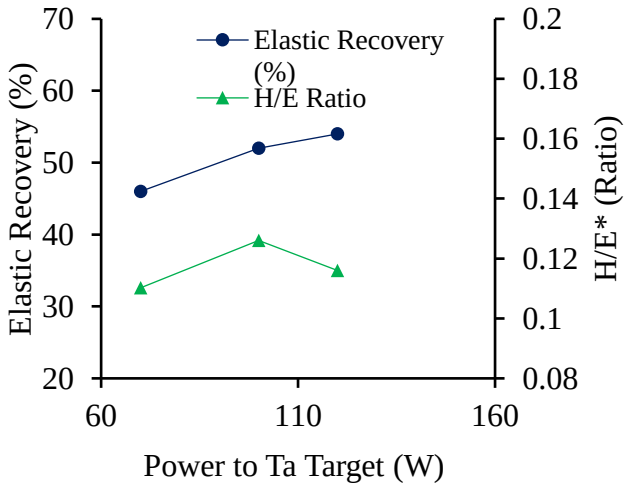

Figure 5-15 Variation in (a) hardness, reduced elastic modulus and residual stress and (b) H/E* ratio and elastic recovery W_e (%) of the films deposited with varying power to Ta target.

Figure 5-15(b) shows the variation of H/E* ratio and elastic recovery W_e (%) of the films. H/E* ratio for all films is ≥ 0.11. Elastic recovery is observed to increase gradually from ~ 45%

(at 70 W) to ~ 58% (at 120 W). Hard coatings with high values of H/E* ratio ≥ 0.1 and high W_e (> 60%) exhibit high resistance to plastic deformation and increase the resistance of the coating to cracking.

5.5 Conclusions of Magnetron Sputtered Ta-Si-N Films

Two different series of Ta-Si-N coatings were produced using the in-house SaNEL PVD Magnetron Sputtering system. Based on the analysis presented here, interesting relationships between the processing conditions and the microstructure, emerged, which led to a better understanding of the effect of microstructure on the mechanical properties of these films.

The effect of varying N_2/ (N_2 + Ar) gas ratio on the mechanical properties was investigated. Based on the extensive study on the Ta-N system, the N_2/ (N_2 + Ar) gas ratio was varied from 7% to 20% (while keeping the power to Ta and Si targets constant at 150 W and 13 W respectively). It was found that increasing the N_2/ (N_2 + Ar) gas ratio from 7% to 15%, led to increase in hardness from ~30 GPa to ~42 GPa. This was due to the significant change in crystal structure and microstructure of the films with changing N_2/ (N_2 + Ar) gas ratio. Film crystal structure changed from textured hex Ta_2N (at 7%) to uniform non-textured hex Ta_2N (at 10% and 13%) to mixture of hex Ta_2N and fcc TaN (at 15%) to fcc TaN (at 20%).

The first experiment involved film deposition with 150 W of power to Ta, 13 W to Si and 7% N_2. XRD revealed a hex Ta_2N structure for this film with a hardness of ~30 GPa. High resolution TEM showed some signs of the nc-TaN a-Si_3N_4 microstructure, as proposed by Veprek [18]. However, the presence of amorphous content at the grain boundaries was not innately clear and most of the grains were only distinguishable by low angle grain boundaries, visible via slight changes in the angles of the lattice fringes. The composition for this film showed little incorporation of Si (~5 at. %). This led to the conclusion that Ta at this power was overwhelming

the plasma in the system, preferentially reacting with N and using up the major content of N_2 to form Tantalum rich Ta_2N. Consequently, the content of N_2 was increased from 7% to 10%, 13%, 15% and 20%. The texture greatly decreased and led to the formation of more uniform hex Ta_2N phase with increase in N_2 to 10% and 13% N_2. This was possibly due to increase of Si incorporation (formation of amorphous phase which breaks textured structure) in the film (as Si_3N_4, possibly due to more N_2 available for Si to react) and was confirmed by AES which depicted Si content to be ~13% for these films. The TEM for the 13% film revealed columnar morphology (20-30 nm wide columns) with hex Ta_2N nanograins/nanoneedles (5-15 nm size) oriented in different crystallographic orientations in individual columns, separated by amorphous boundaries which were not clearly visible. The 13% film had a high hardness of ~39 GPa, high elastic recovery of ~60% and least wear rate amongst all tested films (7×10^{-6} mm^3/Nm), with coefficient of friction ~0.6. This film was oxidation resistant to ~800 ^oC. The nanoneedles found in this film act as a resistance to dislocation movement and hence increase the hardness of the material.

Increase in N_2 to 15%, resulted in a film with mixture of phases, the Ta rich hex Ta_2N phase and fcc TaN. This film displayed impressive highest hardness of ~42 GPa. The microstructure of this film was again columnar without presence of any amorphous boundaries between them. The Si content for these films was around ~8%. Although the N_2 content was higher than in the 13% N_2 film, the formation of two crystal structures led to decrease in incorporation of Si in its Nitride state (Si_3N_4). Presence of amorphous boundaries around the nanograins was visible via compositional contrast in the columns. The absence of amorphous columns in this film with sharp interface between the nanocrystalline columns led to the highest hardness of this film. Both the 13% and 15% N_2 films displayed high resistance to plastic deformation as their H/E* ratio was >0.11 and elastic recovery ~60%. Further increase in N_2 to 20%, led to cracking of the film possibly

due to higher residual stress. The crystal structure for this film was fcc TaN which was still emerging in the 15% film. This investigation indicates that high hardness was displayed by the films deposited with ~10% - 15% N_2. However, the 15% N_2 film, due to formation of hard hex Ta_2N phase in the top surface layers along with optimal formation of Si_3N_4 amorphous boundaries around nanocrystalline Ta-N grains displayed overall impressive mechanical properties. Overall, 10%-15% N_2 content in the gas ratio at 150 W power to Ta and 13 W power to Si, led to films with desirable microstructure and impressive mechanical properties.

The second set of experiments was a trial series based on the previously worked Ta-N system to determine deposition conditions which could result in expected chemical compositions and increased hardness and provided understanding of the quite involved relationships between composition, chemical states, microstructure and mechanical properties. The effects of varying power to the Ta target, (70 W to 120 W) (to vary composition) on the mechanical properties was studied, while power to Si (13 W) and N_2/ (N_2 + Ar) gas ratio (7%) was kept constant. Increased power to the Ta target was carried out in order to increase the incorporation of Ta in Ta-N binding state and limiting the incorporation of Si in the Si_3N_4 state ~ 10%.

The transition of the crystal structure went from non- stoichiometric fcc $TaN_{0.01}$ (at 70 W) to uniform hex Ta_2N crystal structure (100 W) to textured hex Ta_2N structure (at 120 W). XRD showed a decrease in texturing for the films deposited with lower power (~100 W) to Ta target as compared to the film deposited with 120 W power. This could be due to the increased incorporation of Si in the films, at comparatively lower power to Ta (100 W), which refines the microstructure and decreases texturing. Increasing power to the Ta target (from 70 W to 100 W) led to increase in hardness from ~25 GPa to ~30 GPa and further increase in power to Ta (from 100 W to 120 W) led to decreased hardness from ~ 30 GPa to ~27 GPa of the coatings. The high hardness of the 100

W film can be attributed to its uniform crystal structure and optimal formation of the amorphous boundary regions around the nano crystallites of Ta-N. Decrease in hardness (for the 120 W film) with increase in texture within the hex Ta_2N crystal structure was a recurring theme observed in all series of Ta-Si-N coatings explored in this chapter, regardless of the deposition parameter being investigated in each series. The residual stress increases with increase in power to Ta target. Analysis of the Low Angle XRD, XPS and nano-indentation data suggest that in addition to the presence of the uniform hex Ta_2N structure, incorporation of Si in the microstructure should not be very high (leading to higher volume fraction of soft grain boundary area which leads to decrease in hardness) and should not be completely absent (no amorphous grain boundary region which leads to high residual stress, decreased oxidation resistance and in some cases decreased hardness). It should be optimal enough to result in the expected 1-2 monolayer thick Si_3N_4 boundary area around the distributed Ta-N nanocrystals for high hardness of films with less residual stress. It is observed that the incorporation of right amount of Ta, Si and N, and their role in evolvement of the microstructure, along with the desired crystal structure (uniform hex Ta_2N in this case), all play a crucial role in the enhancing mechanical properties of the films.

Chapter 6 Conclusions

In this body of work, two transition metal nitride systems were explored, Ta-N and Ta-Si-N with the goal of developing an overall understanding for designing new protective coating systems with desirable properties, by investigating the effects of elemental composition, crystal structure and microstructure on the mechanical properties of the Ta-N/Ta-Si-N coatings.

Extensive study of the relationships of deposition conditions with the microstructure and mechanical properties of Ta-N system was carried out. Ta-N films with hardness as high as 33 GPa were produced. These films were able to resist oxidation up to 780 ^{o}C. Ta-N was used as a model system to explore another high potential candidate for high hardness and high oxidation resistance, Ta-Si-N system. The Ta-Si-N films fabricated in SaNEL were super-hard with hardness of ~42 GPa and excellent thermal stability upto 800 ^{o}C.

The theoretical study for Veprek's proposed model of a pure nc-TiN/a-Si_3N_4 system shows that hardness in excess of 70 GPa can be achieved. However, in practice, it is limited by a variety of flaws of which oxygen impurities are the most dangerous ones. Important is the finding that although the stoichiometric and pure transition metal nitride and Si_3N_4 are immiscible, not all decompose by nucleation, which does not yield uniformly distributed regular nanocrystals of 3-5 nm in size with sharp TmN/Si_3N_4 interfaces. Although, the resulting magnetron sputtered Ta-Si-N coatings still have extraordinary mechanical properties, their properties cannot be completely explained by Veprek's model.

6.1 Ta-N System

Throughout the series of experiments carried out, it was found that the deposition conditions strongly influenced the microstructure and hence mechanical properties of the Ta-N

films. It was observed in the case of each series, films with non-textured hex Ta_2N crystal structure or a mixture of fcc TaN and hex Ta_2N had impressive mechanical properties in terms of increased hardness and decreased residual stress. Substrate bias of -100 V (compared to -50V, -200 V and -300 V) and low N_2/ (N_2 +Ar) ratio (~3% - 5%) resulted in films with high hardness of ~33 GPa, elastic recovery of ~60% and low residual stress of ~ 1 GPa. High substrate bias exceeding -100 V negatively affected residual stress and elastic recovery, though resulted in enhancing hardness to a small extent (~4 GPa) and reducing incorporation of residual oxygen in the films. The microstructure of the film varied greatly with varying N_2/ (N_2 +Ar) ratio. The microstructure changed from columnar morphology (at 7% N_2) to non-columnar uniformly distributed nanograins (~ 2-5 nm size) separated by amorphous boundaries (at 5% N_2) to nano-needle like structure (~ 5-10 nm size) (at 3% N_2). This microstructure along with the change in crystal phases led to increase in hardness to ~32 GPa (at 5% N_2) from ~27 GPa (at 7% N_2). The film with 3% N_2 was dominated by uniform non-textured hex Ta_2N crystal structure. This film was composed of nano–needle like structure and grain size varied from ~ 5 – 10 nm, which played a critical role in enhancing the hardness of this film to ~33 GPa with low compressive stress of 1.51 GPa. The oxidation resistance for all the three Ta-N samples with 7%, 5% and 3% N_2/ (N_2 + Ar) ratio seems to be almost same and is around 750 ^oC.

Overall, it is observed that decreasing the N_2 content in the gas mixture, besides promoting the formation of hard hex Ta_2N phase, resulted in refining the microstructure. This refinement in microstructure resulted in significantly increasing the hardness of the Ta-N films.

6.2 Ta-Si-N System

The Ta-N system was studied as a model to explore and design another potential high hardness and oxidation resistant, Ta-Si-N system. Two series of experiments were carried out to

study the Ta-Si-N system. It was observed throughout the series that the transition in the crystal structure of Ta-Si-N films with varying N_2/ (N_2 +Ar) ratio was the same as observed with Ta-N films. Transition went from fcc TaN (at 20% N_2) to mixture of fcc TaN and hex Ta_2N (at 15 % N_2) to uniform nontextured hex Ta_2N (at 13% and 10% N_2) to textured hex Ta_2N (at 7% N_2). The microstructure observed in the Ta-Si-N coatings via HRTEM, changed from uniformly distributed nanograins (~5-15 nm size) with/without amorphous boundaries between them (at 7% N_2) to columnar morphology (at 13% N_2) with amorphous boundaries between the columns to columnar structure without any amorphous boundaries between them (at 15% N_2).

For the 7% film, nano grains (~5-15 nm size) could be observed. In rarer cases, grain boundaries could be distinguished as lighter areas lacking lattice fringing located immediately adjacent to crystalline regions. These grain boundaries did not typically connect to form distinct grains, however. Instead, the grain boundaries served to distinguish loosely defined sub-domains at the nano-scale. The microstructure especially in the 13% N_2 film played a significant role not only in enhancing the hardness of the film, but also enhancing other mechanical properties such as H/E* ratio, elastic recovery and tribological behavior. This film depicted dense columnar morphology, with loosely defined sub-domains present within individual columns. Nanocrystalline columns boundaries were more clearly defined and had thin amorphous columns in between them; however, the opposite was true of the sub-domains present within the columns. This hardness of this film was ~39 GPa, H/E* was 0.13, high elastic recovery of ~60%, very low wear rate with low friction coefficient of 0.6. The oxidation behavior of this film was impressive as it remained stable upto ~800 ^{o}C.

The 15% N_2 film, was super hard, with excellent hardness of ~ 42 GPa. The HRTEM revealed dense columnar morphology without presence of any amorphous boundaries between

them. In a typical column, lattice fringing was continuous across most of the column, with possible sub-domains distinguishable by way of lighter and darker areas, presumably due to compositional contrast. Amorphous grain boundaries could be distinguished within a column around crystalline region, as lighter areas lacking lattice fringing. The absence of soft amorphous columns (possibly Si_3N_4) in this film led to highest hardness of this film as compared to the 13% N_2 film, which had same crystal hex Ta_2N structure.

6.3 Conclusion

Through the exploration of two different transition metal nitride thin film nanocomposite systems synthesized via magnetron sputtering, a deeper understanding of the relationship between the microstructure and the mechanical properties of the films was obtained. The deposition parameters had a significant effect on crystal structure and the microstructure of the films. Based on the knowledge gained, coatings with hardness as high as 42 GPa were produced in-house.

It was observed that one of the possible reasons that Vepreks's proposed structure could not be fully mimicked by the Ta-Si-N system was the lack of the high content of the Si_3N_4 phase required for the Ta-Si-N system as compared to TiSiN system (~10%). The reason for this lies in the shape of the nanograins formed. TiSiN nanograins formed are FCC and round whereas the nanograins for the hard hex Ta_2N phase from Ta-Si-N system are needle like. Needle like shaped structures are expected to have more surface area as compared to rounded structures. Hence, the content of Si required to form that uniform monolayer around needle like structures would be greater than that required for rounded structures (~10 % Si). The Si at. % for the Ta-Si-N films was restricted from ~9% - 13%, which did form amorphous boundaries around nano-needles but was not enough to cover the entire grain.

One of the other proposed nanostructures by Musil [57] which is supposed to result in hardness enhancement was experimentally verified for the Ta-Si-N system in this investigation. Comparison of the two-coating systems Ta-N and Ta-Si-N, led to the understanding of the role of thin (~5 nm) amorphous boundaries of a strong stable covalent nitride present around nanograins or in between nanocolumns of transition metal nitride. In general, hardness enhancement occurred when the hard-uniform hex Ta_2N crystal structure was formed, having dense columnar morphology, along with grains being separated by amorphous boundaries. The presence of smaller, nano-scale sub-grains or sub-domains was consistently noted through the course of this study. Decrease in volume fraction of amorphous columnar boundaries resulted in further increase in hardness and elastic recovery. Limiting Si content to ~ 9% resulted in the film with highest hardness while oxidation resistance of the coating was also acceptable.

The Ta-Si-N nanocomposite system displayed enhanced properties as compared to the Ta-N system, in terms of hardness, residual stress, elastic recovery, H/E* ratio, tribological behavior and oxidation resistance. It is observed that optimal incorporation of the stable covalent nitride (Si_3N_4) as a thin amorphous layer in between Ta-N nanograins did result in the development of super hard Ta-Si-N films (hardness ~ 42 GPa) and increasing its thermal stability (stable upto 800 ^oC).

References

1. H. Fischer. Polymer nanocomposites: from fundamental research to specific applications. Materials Science and Engineering C, 2003, 23, 763-772.

2. R. Hauert and J. Patscheider. From alloying to Nanocomposites—Improved performance of hard coatings. Advanced Engineering Materials, 2000, 2(5), 247–259.

3. Cision PRweb. Global coatings market to reach 8.7 billion gallons and US$107 billion by the year 2017, According to New Report by Global Industry Analysts, Inc. 2012. (http://www.prweb.com/releases/architectural_coatings/oem_special_purpose/prweb9264512.htm).

4. New study analyzes world market for nanocoatings. Coatings World, 2012, (https://www.thefreelibrary.com/New study anylyzes world market for nanocoatings-a0285887545).

5. R. H. Fernando. Nanocomposite and Nanostructured Coatings: Recent Advancements. Nanotechnology Applications in Coatings, 2009, ACS Symposium Series, 1008, Chapter 1, 2–21.

6. J. Musil. Hard and superhard nanocomposite coatings. Surface and Coatings Technology, 2000, 125, 322-330.

7. G. Erkens. New approaches to plasma enhanced sputtering of advanced hard coatings. Surface and Coatings Technology, 2007, 201, 4806-4812.

8. H. Gleiter. Nanocrystalline materials. Progress in Materials Science, 1989, 33, 223-315.

9. R. Birringer. Nanocrystalline materials. Materials Science and Engineering A, 1989, 117, 33-43.

10. R.W. Siegel. Cluster-Assembled Nanophase Materials. Annual Review of Materials Science, 1991, 21, 559-578.

11. R.W.Siegel. What do we really know about the atomic-scale structures of nanophase materials? Journal of Physics and Chemistry of Solids, 1994, 55, 1097-1106.

12. A. Niederhofer, P. Nesládek, H. D. Männling, K. Moto, S. Veprek and M. Jílek. Structural properties, internal stress and thermal stability of nc-TiN/a-Si_3N_4, nc-TiN/TiSix and nc-$(Ti_{1-y}Al_ySi_x)N$ superhard nanocomposite coatings reaching the hardness of diamond. Surface and Coatings Technology, 1999, 120–121 173-178.

13. K. Lu. Nanocrystalline metals crystallized from amorphous solids: nanocrystallization, structure, and properties. Materials Science and Engineering: R: Reports, 1996, 16, 161-221.

14. B.X. Liu, O. Jin. Formation and Theoretical Modeling of Non-Equilibrium Alloy Phases by Ion Mixing. Physica Status Solidi A, 1997, 161, 3-33.

15. S. Yip. Nanocrystals: The strongest size. Nature, 1998, 391, 532–533.

16. A.A. Voevodin, J.S. Zabinski. Superhard, functionally gradient, nanolayered and nanocomposite diamond-like carbon coatings for wear protection. Diamond and Related Materials, 1998, 7, 463-467.

17. Czichos, H. Tribology: Scope and Future Directions of Friction and Wear Research. The Journal of The Minerals, Metals & Materials Society, 1983, 35, 18-20.

18. S.Vepřek, M.Haussmann, S.Reiprich, Li Shizhi, J.Dian. Novel thermodynamically stable and oxidation resistant superhard coating materials. Surface and Coatings Technology, 1996, 86–87, 394-401.

19. J. Musil. Flexible hard nanocomposite coatings. RSC Advances, 2015, 5, 60482-60495.

20. E.O. Hall. The Deformation and Ageing of Mild Steel: II Characteristics of the Lüders Deformation. Proceedings of the Physical Society. Section B, 1951, 64, 742-747.

21. N.J. Petch. The ductile-brittle transition in the fracture of α-iron: I. The Philosophical Magazine: A Journal of Theoretical Experimental and Applied Physics, 1953, 3, 1089-1097.

22. H.Gleiter. Nanostructured Materials. Advanced Materials, 1992, 4, 471-484.

23. P. Baroch, P. Zeman, in: R. Wei (Ed.), Plasma Surface Engineering Research and its Practical Applications. Research Signpost, Kerala, 2008.

24. Musil, J. Hard nanocomposite coatings prepared by magnetron sputtering. Advanced Materials Forum I, 2002, 230, 613-622.

25. S. Veprek and S.Reiprich. A concept for the design of novel superhard coatings. Thin solid Films, 1995, 268, 64-71.

26. M. Zhang, J. Jiang, J. Houška, J. Kohout, J. Vlček, E. I. Meletis. A study of the microstructure evolution of hard Zr-B-C-N films by high resolution transmission electron microscopy. Acta Materialia, 2014, 77, 212-222.

27. A. Zaman, E. I. Meletis. Microstructure and Mechanical Properties of TaN Thin Films Prepared by Reactive Magnetron Sputtering. Coatings, 2017, 9, 209.

28. Bhushan, B.; Gupta, B.K. Handbook of Tribology: Materials, Coatings, and Surface Treatments; McGraw-Hill Book Company: New York, NY, USA, 1991; p. 1168.

29. X. Sun, E. Kolawa, J. Chen, J. Reid, M.A. Nicolet. Properties of reactively sputter deposited Ta–N thin films. Thin Solid Films,1993, 236, 347–351.

30. E.Bemporad, C. Pecchio, S. De Rossi, F. Carassiti. Characterization and hardness modelling of alternate TiN/TiCN multilayer cathodic arc PVD coating on tool steel. Surface and Coatings Technology, 2001, 146–147, 363–370.

31. C. Gautier, H. Moussaoui, F. Elstner, J. Machet. Comparative study of mechanical and structural properties of CrN films deposited by d.c. magnetron sputtering and vacuum arc evaporation. Surface and Coatings Technology, 1996, 86, 254–262.

32. J. Musil, J. Vlcek, P. Zeman. Hard amorphous nanocomposite coatings with oxidation resistance above 1000°C. Advances in Applied Ceramics, 2008, 107, 148-154.

33. R. F. Zhang, A. S. Argon, S. Veprek. Friedel Oscillations are Limiting the Strength of Superhard Nanocomposites and Heterostructures. Physical Review Letters 2009, 102, 015503.

34. S. Veprek. The origin of superhardness in TiN/Si_3N_4 nanocomposites: the role of the interfacial monolayer. High Pressure Research, 2006, 26, 119.

35. S. Veprek. Recent search for new superhard materials: Go nano!. Journal of Vacuum Science & Technology A: Vacuum, Surfaces, and Films, 2013, 31, 050822.

36. J. A. Thornton. High Rate Thick Film Growth. Annual Review of Materials Science, 1977, 7, 239-260.

37. A. R. Oganov, A. O. Lyakhov. Towards the theory of hardness of materials. Journal of Superhard Materials, 2010, 32, 143-147.

38. Teter, D. Computational Alchemy: The Search for New Superhard Materials. MRS Bulletin, 1998, 23(1), 22-27.

39. A. H. Cottrell, A. Seeger, J. L. Amorós. Dislocations in Crystals. Deformation and Flow of Solids, 1956, 33-52.

40. M. Holleck. Material selection for hard coatings. Journal of Vacuum Science & Technology A, 1986, 4, 2661–2669.

41. H. Holleck and V. Schier. Multilayer PVD coatings for wear protection. Surface and Coatings Technology, 1995, 76–77, 328–336.

42. Frank H.W. Löffler. Systematic approach to improve the performance of PVD coatings for tool applications. Surface and Coatings Technology, 1994, 68–69, 729–740.

43. A.C. Fischer-Cripps, S.J. Bull, and N. Schwarzer. Critical review of claims for ultra-hardness in nanocomposite coatings. Philos. Mag., 2012, 92(13), 1601–1630.

44. H. W. RosenbergW. D. Nix. Solid solution strengthening in Ti-Al alloys. Metallurgical Transactions, 1973, 4, 1333-1338.

45. William D. Callister and William D. Callister, Jr. Fundamentals of Materials Science and Engineering: An Interactive Text, 5th Edition. Wiley, December 2000. ISBN.

46. W. Wolf , R. Podloucky , T. Antretter & F. D. Fischer. First-principles study of elastic and thermal properties of refractory carbides and nitrides. Philosophical Magazine B, 1999, 79, 839-858.

47. Z.Y.Liu, X. Guo, J. He, D. Yu, and Y. Tian. Comment on“ Hardness of covalent and ionic crystals: First-Principle calculations”. Physical Review Letters, 2007, 98(10):109601.

48. A. Zerr, G. Miehe, G. Serghiou, M. Schwarz, E. Kroke, R. Riedel, H. Fueß, P. Kroll and R. Boehler. Synthesis of cubic silicon nitride. Nature, 1999, 400, 340–342.

49. E. Kroke and M. Schwarz, Coordination Chemistry Reviews, 2004, 248, 493–532.

50. David R., Christina W. S., Mykhailo M., Christian S., Tatiana B., Marcus R., Schwarz and Edwin Kroke. Interface phenomena in (super)hard nitride nanocomposites: from coatings to bulk materials. Chemical Society Reviews, 2012, 41, 5081–5101.

51. Holl, M.M.B., R.L. Laduca, and P.T. Wolczanski, Early Transition-Metal Nitride Complexes and Their Relation to Solid-State Nitrides. Abstracts of Papers of the American Chemical Society, 1990, 200, 327.

52. Dawson, P.T. and S.A.J. Stazyk. The Preparation and Characterization of Transition-Metal Nitride Films. Journal of Vacuum Science & Technology, 1982, 20(4), 966-967.

53. David M.H. Chemical vapour deposition of nitride thin films. Polyhedron 1994, 13, 1169-1179.

54. M. Nose and W. A. Chiou. Microstructure and mechanical properties of Zr–Si–N films prepared by rf-reactive sputtering. Journal of Vacuum Science & Technology A: Vacuum, Surfaces, and Films, 2002, 20, 823-828.

55. Sarakinos. K, Kassavetis. S, Patsalas. P, Logothetidis. S. Structural factors determining the nanomechanical performance of transition metal nitride films. Surface Engineering, Fundamentals and Applications, 2004, 843, 311-316.

56. J. Musil, P. Baroch, P. Zeman: Hard nanocomposite coatings. Present status and trends, Chapter 1 in “Plasma Surface Engineering Research and its Practical Applications”, (Ed. R.Wei), Research Signpost Publisher, USA, 2008, 1-34.

57. J.Musil, P. Baroch and P. Zeman. Hard nanocomposite coatings. Present stat us and trends. Plasma Surface Engineering Research and its Practical Applications, 2008, 1-33.

58. L. Shizhi, S. Yulong and P. Hongrui. Ti-Si-N films prepared by plasma-enhanced chemical vapor deposition. Plasma Chemistry and Plasma Processing, 1992, 12, 287–297.

59. K. Wasa and S. Hayakawa. Structures and resistive properties of sputtered TiZrAlN thin films. Thin Solid Films, 1972, 10, 367–375.

60. O. Knotek, M. Bohmer and T. Leyendecker. On structure and properties of sputtered Ti and Al based hard compound films. Journal of Vacuum Science & Technology A: Vacuum, Surfaces, and Films, 1986, 4, 2695–2701.

61. H. A. Jehn, S. Hofmann, W. D. Munz. Surface and Interface Characterization of Heat-Treated (Ti,Al)N on High Speed Steel Substrates. Thin Solid Films, 1987, 153, 45–53.

62. W. D. Munz. Titanium aluminium nitride films—A new alternative to TiN coatings. Journal of Vacuum Science and Technology, 1986, A-4, 2717–2725.

63. S. Christiansen, M. Albrecht and H. P. Strunk. Microstructure of novel superhard nanocrystalline-amorphous composites as analyzed by high resolution transmission electron microscopy. Journal of Vacuum Science & Technology B: Nanotechnology and Nanometer Structures Processing, Measurement and Phenomena, 1998, 16, 19.

64. Zeman T, J. Musil, R. Daniel. High-temperature oxidation resistance of Ta–Si–N films with a high Si content. Surface & Coatings Technology, 2006, 200, 4091–4096.

65. C. Cabral Jr., K.L. Saenger, D.E. Kotecki, J.M.E. Harper. Optimization of Ta–Si–N thin films for use as oxidation-resistant diffusion barriers. Journal of Materials Research, 2000, 15, 194-198.

66. F. Letendu, M.C. Hugon, J.M. Desvignes, B. Agius, I. Vickridge, D.J. Kim, A.I. Kingon. Oxidation resistance of TaSiN diffusion barriers. Integrated Ferroelectrics, 2000, 31, 315-322.

67. D.E. Kotecki, J.D. Baniecki, H. Shen, R.B. Laibowitz, K.L. Saenger, J.J. Lian, T.M. Shaw, S.D. Athavale, C. Cabral Jr., P.R. Ducombe, M Gutsche, G. Kunkel, Y.-J. Park, Y.-Y. Wang, R. Wise. (Ba,Sr)TiO_3 dielectrics for future stacked- capacitor DRAM. IBM Journal of Research and Development, 1999, 43, 367 - 382.

68. Valleti, K.; Subrahmanyam, A.; Joshi, S.V.; Phani, A.R.; Passacantando, M.; Santucci, S. Studies on phase dependent mechanical properties of dc magnetron sputtered TaN thin films: Evaluation of super hardness in orthorhombic Ta_4N phase. Journal of Physics D: Applied Physics, 2008, 41, 045409

69. D. Bernoulli, U. Müller, M. Schwarzenberger, R. Hauert, R. Spolenak. Magnetron sputter deposited tantalum and tantalum nitride thin films: An analysis of phase, hardness and composition. Thin Solid Films, 2013, 548, 57–161.

70. Riekkinen, T.; Molarius, J.; Laurila, T.; Nurmela, A.; Suni, I.; Kivilahti, J.K. Reactive sputter deposition and properties of Ta_xN thin films. Microelectronic Engineering, 2002, 64, 289–297

71. Liu, X.; Ma, G.; Sun, G.; Duan, Y.; Liu, S. Effect of deposition and annealing temperature on mechanical properties of TaN film. Applied Surface Science, 2011, 258, 1033–1037.

72. A.A. Adjaottor, E. Ma, E.I. Meletis. On the mechanism of intensified plasma-assisted processing. Surface and Coatings Technology, 1997, 89(3), 197-203.

73. Kim, S.H., J.K. Kim, and K.H. Kim. Influence of deposition conditions on the microstructure and mechanical properties of Ti-Si-N films by DC reactive magnetron sputtering. Thin Solid Films, 2002, 420, 360-365.

74. Hultman, L., Thermal stability of nitride thin films. Vacuum, 2000. 57(1): p. 1-30.

75. Sundgren, J.E.; Johansson, B.O.; Rockett, A.; Barnett, S.A.; Greene, J.E. TiN: A Review of the Present Understanding of the Atomic Electronic Structure and Recent Results on the Growth and Physical Properties of Epitaxial TiN x ($0.6 < x < 1.2$) Layers. In Physics and Chemistry of Protective Coatings: Universal City, CA, 1985; Greene, J.E., Sproul, W.D., Thornton, J.A., Eds.; AIP Conference Proceedings Series 149; American Institute of Physics: New York, NY, USA, 1986; p. 95

76. Lin, J.C.; Lee, C. Growth of Tantalum Nitride Films on Si by Radio Frequency Reactive Sputtering of Ta in N_2/Ar Gas Mixtures: Effect of Bias. Journal of Electrochemical Society, 2000, 147, 713–718

77. K. Hieber. Structural and electrical properties of Ta and Ta nitrides deposited by chemical vapour deposition. Thin Solid Films, 1974, 24, 157–164.

78. S.K. Kim, B.C. Cha. Deposition of tantalum nitride thin films by D.C. magnetron sputtering. Thin Solid Films, 2005, 475(1–2), 202–207.

79. A. Schauer, M. Roschy. R.F. sputtered b-tantalum and b.c.c. tantalum films. Thin Solid Films, 1972, 12, 313–317.

80. T. Oku, E. Kawakami, M. Uekubo, M. Murakami, K. Takahiro, S. Yamaguchi. Diffusion barrier property of TaN between Si and Cu. Applied Surface Science, 1996, 99 (4), 265–272.

81. M. Stavrev, D. Fischer, C. Wenzel, K. Dreschen, N. Mattern. Crystallographic and morphological characterization of reactively sputtered Ta, Ta–N and Ta–N–O thin films. Thin Solid Films, 1997, 307(1–2), 79–88.

82. S. Nakao, M. Numata, T. Ohmi. Thin and low-resistivity tantalum nitride diffusion barrier and giant-grain copper interconnects for advanced ULSI metallization. Journal of Applied Physics, 1999, 38, 2401–2405.

83. Nie, H., Xu, S., You, L., Yang, Z., Wang, S., Ong, C. Structural and electrical properties of tantalum nitride thin films fabricated by using reactive radio-frequency magnetron sputtering. Applied Physics A, 2001, 73, 229–236.

84. W.H. Lee, J. C. Lin, C. Lee, Characterization of tantalum nitride films deposited by reactive sputtering of Ta in N_2/Ar gas mixtures. Materials Chemistry and Physics, 2001, 68 (1–3), 266–271.

85. D. Gerstenberg, C.J Calbick. Effects of nitrogen, methane, and oxygen on structure and electrical properties of thin tantalum films. Journal of Applied physics, 1964, 35, 402.

86. N. Terao. Structure of tantalum nitrides. Japanese Journal of Applied Physics, 1971, 10, 248.

87. Y.X. Leng, H. Sun, P. Yang, J.Y. Chen, J. Wang, G.J. Wan, N. Huang, X.B. Tian, L.P. Wang, P.K. Chu. Biomedical properties of tantalum nitride films synthesized by reactive magnetron sputtering. Thin Solid Films, 2001, 398–399, 471–475.

88. H. Mori, J. Imahori, T. Oku and M. Murakami. Diffusion barriers between Si and Cu. AIP-Conference-Proceedings, 1998, 418, 475.

89. R.Westergard, M. Bromark, M. Larsson, P. Hedenqvist, S. Hogmark. Mechanical and tribological characterization of DC magnetron sputtered tantalum nitride thin films. Surface and Coatings Technology, 1997, 97, 779–784.

90. Lee G R, Kim H, Choi H S and Lee J J. Superhard tantalum-nitride films formed by inductively coupled plasma-assisted sputtering. Surface Coatings and Technology, 2007, 201, 5207–5210.

91. Shin, C.S.; Kim, Y.W.; Gall, D.; Greene, J.E.; Petrov, I. Phase composition and microstructure of polycrystalline and epitaxial TaN_x layers grown on oxidized Si (001) and MgO (001) by reactive magnetron sputter deposition. Thin Solid Films 2002, 402, 172–182.

92. Toth, L. Transition Metal Carbides and Nitrides; Academic Press: New York, NY, USA, 1971; pp. 150–160.

93. C. Stampfl, A.J. Freeman. Stable and metastable structures of the multiphase tantalum nitride system. Physical Review B, 2005, 71, 024111.

94. N. Arshi, J. Lu, C. G. Lee, B. H. Koo, F. Ahmed. Effects of nitrogen content on the phase and resistivity of TaN thin films deposited by electron beam evaporation. The Journal of The Minerals, Metals & Materials Society, 2014, 66 No. 9, 1893–1899.

95. K. Sasaki, A. Noya and T. Umezawa. Stoichiometry of Ta–N film and its application for diffusion barrier in the Al_3Ta/Ta–N/Si contact system. Japanese Journal of Applied Physics, 1990, 29, 1043-1047.

96. Chang, C.C.; Jeng, J.S.; Chen, J.S. Microstructural and electrical characteristics of reactively sputtered Ta–N thin films. Thin Solid Films, 2002, 413, 46–5197.

97. Leyland, A.; Matthews, A. On the significance of the H/E ratio in wear control: A nanocomposite coating approach to optimised tribological behaviour. Wear 2000, 246, 1–11.

98. J.Musil. Hard nanocomposite coatings: Thermal stability, oxidation resistance and toughness. Surface Coatings Technology, 2012, 207, 50-65.

99. Y. Kuo. Reactive ion etching of sputter deposited tantalum oxide and its etch selectivity to tantalum. Journal of the Electrochemical Society, 1992, 139, 579-583.

100. M. Wittmer, J. Noser, H. Melchior, J. Oxidation kinetics of TiN thin films. Journal of Applied Physics, 1981, 52, 6659.

101. W.D. Münz. Titanium aluminum nitride films: A new alternative to TiN coatings. Journal of Vacuum Science & Technology A: Vacuum, Surfaces, and Films, 1986, 4, 2717.

102. J.B. Choi, K. Cho, M.H. Lee, K.H. Kim. Effects of Si content and free Si on oxidation behavior of Ti–Si–N coating layers. Thin Solid Films, 2004, 447- 448, 365-370.

103. L. Castaldi, D. Kurapov, A. Reiter, V. Shklover, P. Schwaller, J. Patscheider. High temperature phase changes and oxidation behaviour of Cr–Si–N coatings. Surf.Coat. Technol., 2007, 202, 781-785.

104. Y.I. Chen, K. Y. Lin, H. H. Wang, Y. R. Cheng. Characterization of Ta–Si–N coatings prepared using direct current magnetron co-sputtering. Applied Surface Science, 2014, 305, 805–816.

105. N. Frety, F. Bernard, J. Nazon, J. Sarradin, J.C. Tedenac. Copper diffusion into silicon substrates through TaN and Ta/TaN multilayer barriers. Journal of Phase Equilibria and Diffusion, 2006, 27, 590–597.

106. J. Jang, E. An, I.W. Park, D.G. Nam, I. Jo, J. Lin, J.J. Moore, K.H. Kim, I. Park. Microstructure and mechanical properties of Ti–B–C–N–Si nanocomposite films deposited by unbalanced magnetron sputtering. Journal of Vacuum Science & Technology A: Vacuum, Surfaces and Films, 2013 31, 061401.

107. Chaudhri, Yong Yee Lim & M. Munawar. The influence of grain size on the indentation hardness of high-purity copper and aluminium. Philosophical Magazine A, 2002, 82, 2071-2080.